Formation and properties of polyvinyl butyral-transition metal alkoxides hybrid hollow fibers using air gap spinning

福井大学審査

学位論文 [博士(工学)]

(A Dissertation submitted to the University of Fukui for the Doctoral Degree of Engineering)

Formation and properties of polyvinyl butyral-transition metal alkoxides hybrid hollow fibers using air gap spinning

（エアギャップ紡糸を用いたポリビニルブチラール-遷移金属アルコキシドハイブリッド中空糸の形成と特性）

March 2023

Anamul Hoque Bhuiyan

TABLE OF CONTENTS

LIST OF SCHEMES

ACRONYMS

OIHFs	Organic/inorganic Hybrid Fibers
1D	One Dimensional
TEOS	Tetraethyl Orthosilicate
Cr (VI)	Chromium (VI)
kDa	Kilodalton
UV-Vis spectra	Ultraviolet-Visible Spectra
M_w	Molecular Weight
gm	Gram
hrs	Hours
°C	Degree Celsius
mm	Millimeter
cm	Centimeter
nm	Nanometer
μm	Micrometer
L	Litre
%	Percentage
Å	Angstrom
cc	cm^3
atm	Atmospheric Pressure
Pa	Pascal
kV	Kilovolt
Au	Aurum
Pd	Palladium
Ar	Argon
σ	Standard Deviation
D	Average Diameter
cps	Counts Per Second
keV	Kiloelectron Volt
BE	Binding Energy
a.u.	Arbitrary Unit
IβG	Immobilized β-galactosidase
IL	Immobilized Lipase

FWHM	Full Width at Half Maximum
λ	Wavelength
STP	Standard Temperature and Pressure
BJH	Barrett–Joyner–Halenda
°	Degree

CHAPTER ONE

1. INTRODUCTION

1.1 BACKGROUND OF THE STUDY

Organic/inorganic hybrid fibers (OIHFs) are a class of flexible pseudo-1D materials, featured with a reasonably high aspect ratio and distinct organic/inorganic species domains that have gained attention for a variety of applications [1]. OIHFs produce beneficial new properties as a result of the synergistic interactions between organic and inorganic components, rather than just combining the inherent benefits of individual entities [2–5]. The interaction of organic and inorganic components via covalent bonds, ionic bonds, hydrogen bonds, van der Waals forces, and electrostatic interactions greatly influences the characteristics of hybrid fibers. An organic fiber matrix, which generally has unique anisotropic features, high flexibility, low density, and a large specific surface area, is thought to be the ideal platform for integrating different inorganic components [6–9]. To provide extraordinary properties within the organic fiber matrix, inorganic species such as metal (or nonmetal) nanoparticles, and their compounds can be mixed with the fiber matrix in various ways. To date, various synthetic methods have been developed to create functioning OIHFs. Inorganic species are incorporated into the organic fiber matrix during the fiber fabrication procedures (sol-gel, liquid phase, wet spinning, electrospinning, etc.), resulting in homogeneous OIHFs with controlled overall structures [10,11]. Notably, the molecular assembly of organic and inorganic components opens up new possibilities for creating OIHFs and provides a strong foundation for precisely controlling the ratio and spatial distribution of organic/inorganic species.

OIHFs are commonly developed from a polymer including cellulose acetate (CA), polyvinyl alcohol (PVA), polyacrylonitrile (PAN), polysulfone (PSF), polyurethane (PU), and conducting polymer fibers, such as polypyrrole (PPy), polyaniline (PANI), and poly (3,4-ethylenedioxythiophene) (PEDOT). These 1D organic components are bonded to a wide variety of inorganic materials including precious metals (e.g., gold (Au), silver (Ag), platinum (Pt), and palladium (Pd)); nonprecious metals (e.g., iron (Fe), cobalt (Co), nickel (Ni), copper (Cu), zinc (Zn), titanium (Ti), zirconium (Zr), molybdenum (Mo), tungsten (W), tin (Sn), and antimony (Sb)), alongside their compounds (e.g., oxides, carbides, nitrides, sulfides, phosphides, and carbonitrides); nonmetallic element (e.g., aluminum (Al), silicon (Si)) as well as their oxides; and heteroatoms (e.g., nitrogen (N), boron (B), phosphorus (P), and sulfur (S)) [1].

Sol-gel chemistry not only offers access to ceramics and glasses with improved or new properties but also led to allow the incorporation of organic moieties into inorganic materials in a mild reaction condition. According to several reviews, the sol-gel approach describes the basic chemistry behind the preparation, various chemistry pathways, and the factors influencing the processing techniques in the area of organic/inorganic hybrid materials/fibers [12]. Wet spinning is another convenient technique where OIHFs could be developed with controlled diameter by changing the nozzle sizes, spinning solution viscosity, and coagulation liquid concentrations [13]. In contrast to wet spinning, dry-jet-wet spinning involves the extrusion of the dope through an air gap, followed by conventional coagulation. This can resolve some of the drawbacks of wet-spinning technology. The extruded dope can cool somewhat in the air gap before entering the coagulation bath, and the high stresses that have built up inside the spinneret assembly are also

relaxed as a result. In comparison to wet spinning, Baojan et al. observed that dry-jet-wet spinning had a softer coagulation and showed that spinning speeds could be increased [14]. In the study of hollow fiber membrane formation by dry-jet wet spinning, many researchers have examined the effect of the air gap length on the performance of the final membranes. According to their interpretation, the developing fiber was stretched and lengthened by its weight and the polymer aggregates came closer together and realigned themselves into a condition of increased solidity [15]. Accordingly, using air gap (dry-jet wet) spinning, Nakane et al. developed CA-Ti alkoxide and CA-Zr alkoxide hybrid gel fiber (**Scheme 1.1**) for the entrapment of different biocatalysts [16].

Moreover, OIHFs with different textural characteristics can be easily prepared by controlling organic/inorganic precursors in electrospinning conditions. The synthesis of OIHFs through electrospinning can be roughly divided into two types. One is based on the electrospinning of an inorganic precursor and polymer solution, occasionally followed by postprocessing like calcination. The other is to directly embed the prepared inorganic particles in the fiber network [1]. Shao et al. first reported that a PVA/silica hybrid with different silica content can be prepared via the electrospinning process by using the PVA and TEOS mixture as precursor [17]. Liquid phase synthesis is an effective method for producing hybrid nanofiber due to the high reactivity of reactants, easy control of solution reactions, and low energy consumption [18]. Furthermore, molecular-level assembly of organic and inorganic components is another approach that offers a powerful platform for accurately controlling the proportion and spatial distribution of organic/inorganic species by using pairs of complementary polymers as building blocks, which have been extensively studied [19].

Enzyme immobilization technology can offer an opportunity for increasing enzyme stability and reusability. Enzyme immobilization is irreversible when the enzyme and support material are bound together by covalent bonds [20], entrapment, encapsulation, cross-linking, or network formation [21]. Recently, OIHFs as a support matrix has been at the center of researchers' focus because they carry the characteristics of both organic and inorganic materials. They usually solidify the interactions between the enzyme and the support material, with an increase in mechanical resistance and stability of the biocatalyst under the reaction conditions [22,23]. Organic-metal oxide hybrid materials such as chitosan-ZnO_2, and alginate-TiO_2 have shown their potential as a support matrix for enzyme immobilization because these compounds present particularly high stability, and mechanical resistance, and still preserve a high affinity for biological molecules [24,25]. Ikeda et al. and Nakane et al. developed CA-metal (Zr, Ti) alkoxide gel fiber by a facile air gap spinning method where successfully entrap-immobilized different biocatalysts (β-galactosidase, invertase, urease, lipase) showed stability in phosphate buffer solution, electrolyte solution, and organic solvents, as shown in **Fig. 1.1** [26,27].

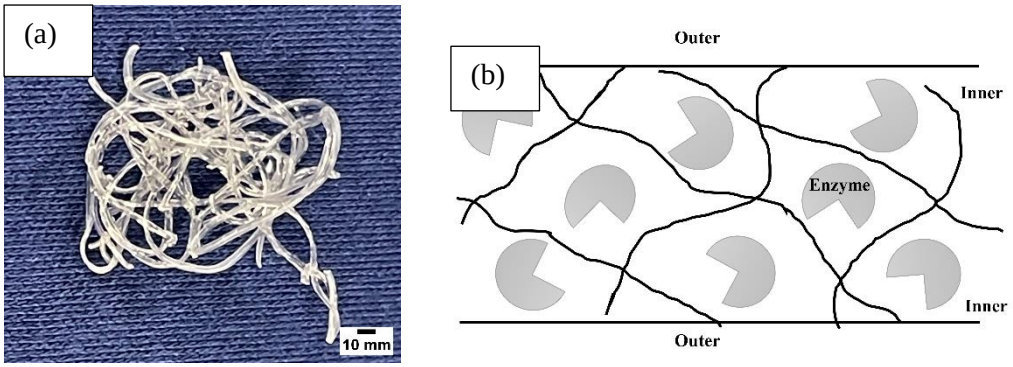

Fig. 1.1 (a) Photograph of CA-Ti hybrid gel fiber, and (b) illustration of enzyme immobilized CA-metal alkoxides hybrid gel fiber.

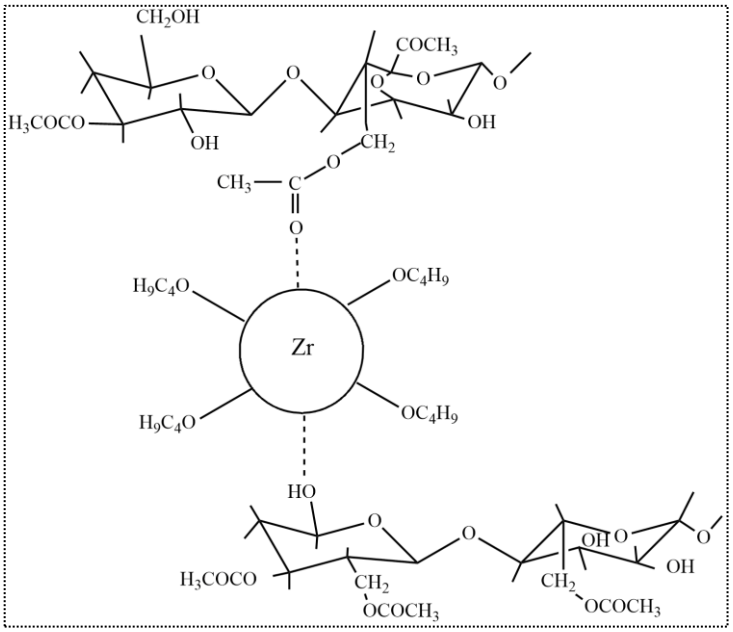

Scheme 1.1 Schematic illustration of CA-Zr hybrid gel fiber formation by wet spinning [27].

Moreover, organic-inorganic hybrid adsorbents (beads, fibers, aerogels), one of the most promising materials to replace conventional single-component adsorbents, have gained attention because of their greater adsorption properties and enhanced structural stability against organic and other pollutants [28]. For example, Zhang et al. prepared a magnetic cellulose bead entrapping activated carbon to remove dyes including methylene blue (MB) and methyl orange (MO) [29]. Li et al. successfully developed an adsorbent based on the maleic anhydride-modified cellulose beads and alkali-treated diatomite [30]. Asai et al. reported about CA-TiO_2 hybrid fiber to remove MB and Cr(VI) from wastewater [31]. Mandal et al. had a sol-gel process for the synthesis of polyacrylamide-Zr hybrid material to remove arsenic (III) from water [32]. Additionally, amorphous OIHFs could be handy to develop inorganic nanofiber and later useful for photocatalysis of organic, inorganic pollutants removal from wastewater. Nakane et al. have developed mesoporous

TiO_2 nanotubes prepared from electrospun polyvinyl alcohol-titanium isopropoxide hybrid fiber template and further, they showed the successful MB photocatalysis [33].

Poly (vinyl butyral) (PVB) is a product of the reaction between poly (vinyl alcohol) (PVA) and the butyraldehyde in the presence of an acid catalyst. PVB is a non-toxic, odorless, and environment-friendly polymer, and it is widely used as functional material in various fields. PVB can endure low temperatures, light, changes in humidity, bacteria, other microorganisms, alkali, and diluent acids. Also, because of its good compatibility with inorganic materials, PVB is an excellent organic component for the fabrication of organic/inorganic hybrid composites.[34]. Due to good hydrophilicity, it has been reported that PVB is used to prepare affinity membranes by thermally induced phase separation (TIPS) and non-solvent induced phase separation (NIPS) processes [35]. Wang et al. developed a PVB-carbon nanotube (PVB-CNT) for the ultrafiltration of bovine serum albumin and humic acid solutions [36]. However, Nakane et al. and Chen et al. developed PVB-TiO_2 and PVB-SiO_2 hybrid nanostructures (composites, fiber) by sol-gel process and electrospinning respectively [37,38]. Accordingly, later on, Nakane and coworkers had another report on the formation of PVB-zirconium dioxide (PVB-ZrO_2) hybrid film by sol-gel process [39].

Zirconia and titania have superior alkali resistance than the other ceramic metal oxides, are nearly insoluble over a wide pH range, and exhibit exceptional tolerance to high temperatures [40]. Zirconia has widely been used as a catalyst for various reactions [41] and absorbent for organic pollutants. In the form of a catalyst-supporting material and absorbent material, the mesoporous ZrO_2 structure could be effective with increased surface area, enhanced catalytic activity, surface active sites, and absorption sites [42]. On the other hand, titania has attracted significant attention for wastewater treatment via the photocatalysis process, especially for crystalline TiO_2 due to its high stability, low cost, harmless, high catalytic activity, and availability [43]. However, amorphous titania could also be effective in the case of pollutant removal since it is more easily prepared at room temperature, higher surface area, and possibility to dope with other substances. Wang et al. prepared amorphous titania by hydrolysis which could successfully remove Cr(VI) and rhodamine B under visible light irradiation [44].

Like CA, PVB is a random hydrophilic copolymer having acetyl and hydroxyl groups which can make the same coordinate bond with transition metal (Zr, Ti) alkoxides. Therefore, an air gap (dry-jet wet) spinning method could be applied for the formation of PVB-transition metal oxides hybrid hollow fiber. And later on, PVB-ZrO_2 and PVB-TiO_2 hybrid fiber could be used as an alternative approach in enzyme immobilization carrier and dye adsorption process that may overcome the limitations of CA-ZrO_2 and CA-TiO_2 hybrid fiber in this respective field reported by Nakane et al. and Asai et al. respectively.

1.2 AIM AND OBJECTIVES OF THE RESEARCH

This research aims to develop OIHFs to accomplish several performances in the catalysis field and to reduce environmental damage at an acceptable level.

To achieve the aim of the research, the overall activities of this study have been designed by following specific objectives:

(I) Development of PVB-metal alkoxides (PVB- Zr alkoxide, PVB- Ti alkoxide) hybrid hollow fiber by air gap spinning.

(II) Utilization of PVB-Zr alkoxide hybrid fiber as an enzyme immobilization support matrix for several bio-catalysts (β-galactosidase, lipase) aimed at catalysis reactions.

(III) Employment of PVB-Ti alkoxide hybrid fiber for the removal of organic dye from wastewater.

1.3 RESEARCH QUESTIONS

To achieve these objectives, experimental analyses were conducted to answer the following research questions:

(a) What could be the principle of the preparation of PVB-metal alkoxides hybrid fiber by air gap spinning?

(b) How can the enzyme-immobilized PVB-Zr alkoxide hybrid fiber be useful for the catalysis process?

(c) How can the PVB-Ti alkoxide hybrid fiber be suitable for successful application in the field of organic pollutants removal?

1.4 OUTLINE OF THE THESIS

Most of the part of this research study has been published in the journal and is included in the thesis. That's why the design of the "thesis with the publication" is presented to extant the dissertation. The whole thesis covers seven individual chapters to interpret and comprehend all the research findings and final results. The content of each chapter is as follows:

Chapter One presents the current research work and delivers a synopsis of OIHFs (Organic-inorganic hybrid fibers) preparation and application. Later the aim and objectives, and research questions are mentioned, and finally, the chapter concludes with the outline of the thesis.

Chapter Two deals with the literature review. This chapter discussed the basic idea of OIHFs including a review of organic-metal oxides hybrid fiber and their properties, and the preparation process. In addition, the overview of enzyme immobilization techniques and the organic-inorganic substances removal process by OIHFs have also been discussed.

Chapter Three depicts the experimental investigation, including the materials and reagents used, and the methods used to carry out this study. The thorough experimental techniques used to measure and characterize the materials developed in this study are also described.

Chapter Four covers the details of the development and structural analysis of PVB-ZrO_2 hybrid fiber by an air gap (dry-jet wet) spinning.

Chapter Five explores the application of the spun PVB-ZrO_2 hybrid fiber in multiple fields. This chapter emphasizes enzyme-immobilized PVB-ZrO_2 hybrid fiber's potentiality in lactose hydrolysis and ester synthesis reaction [45].

Chapter Six deals with the fabrication of PVB-amTiO_2 hybrid fiber by an air gap (dry-jet wet) spinning for the removal of methylene blue (MB) dye from an aqueous solution.

Chapter Seven concludes the thesis, summarizing the results and limitations. Possible future outlooks and recommendations based on this research are suggested for further investigations in this field.

REFERENCES

1 F. Zhang, P. C. Sherrell, W. Luo, J. Chen, W. Li, J. Yang and M. Zhu, *Advanced Science*, 2021, **8**, 2102859.
2 B. Ding, *Advanced Fiber Materials*, 2020, 2, 45–45.
3 M. Zhi, C. Xiang, J. Li, M. Li and N. Wu, *Nanoscale*, 2013, **5**, 72–88.
4 X.-Y. Du, Q. Li, G. Wu and S. Chen, *Advanced Materials*, 2019, **31**, 1903733.
5 P. S. Kumar, J. Sundaramurthy, S. Sundarrajan, V. J. Babu, G. Singh, S. I. Allakhverdiev and S. Ramakrishna, *Energy & Environmental Science*, 2014, **7**, 3192–3222.
6 W. Huang, Y. Xiao, and X. Shi, *Advanced Fiber Materials*, 2019, **1**, 32–45.
7 Y. Zhang, X. Xia, X. Cao, B. Zhang, N. H. Tiep, H. He, S. Chen, Y. Huang and H. J. Fan, *Advanced Energy Materials*, 2017, **7**, 1700220.
8 J. Liang, G. Zhu, C. Wang, Y. Wang, H. Zhu, Y. Hu, H. Lv, R. Chen, L. Ma and T. Chen, *Advanced Energy Materials*, 2017, **7**, 1601208.
9 S. Jiang, J. Li, J. Fang and X. Wang, *Small*, 2021, **17**, 1903760.
10 Y. Zhu, X. Fan, L. Suo, C. Luo, T. Gao and C. Wang, *ACS Nano*, 2016, **10**, 1529–1538.
11 Y. Xu, Y. Zhu, F. Han, C. Luo, and C. Wang, *Advanced Energy Materials*, 2015, **5**, 1400753.
12 S. Pandey and S. B. Mishra, *Journal of Sol-Gel Science and Technology*, 2011, **59**, 73–94.
13 H.-P. Cong, X.-C. Ren, P. Wang and S.-H. Yu, *Scientific Reports*, 2012, **2**, 613.
14 P. Bajaj, T. V. Sreekumar and K. Sen, *Journal of Applied Polymer Science*, 2002, **86**, 773–787.
15 J.-J. Qin, J. Gu and T.-S. Chung, *Journal of Membrane Science*, 2001, **182**, 57–75.
16 Y. Kurokawa, *Polymer Gels and Networks*, 1996, **4**, 153–163.
17 C. Shao, H.-Y. Kim, J. Gong, B. Ding, D.-R. Lee and S.-J. Park, *Materials Letters*, 2003, **57**, 1579–1584.
18 A. Kumar, M. M. Mohammadi and M. T. Swihart, *Nanoscale*, 2019, **11**, 19058–19085.
19 H. Cui, Z. Chen, S. Zhong, K. L. Wooley and D. J. Pochan, *Science*, 2007, **317**, 647–650.
20 Y.-T. Zhu, X.-Y. Ren, Y.-M. Liu, Y. Wei, L.-S. Qing and X. Liao, *Materials Science and Engineering: C*, 2014, **38**, 278–285.
21 S. Zahirinejad, R. Hemmati, A. Homaei, A. Dinari, S. Hosseinkhani, S. Mohammadi and F. Vianello, *Colloids, and Surfaces B: Biointerfaces*, 2021, **204**, 111774.
22 H. Xue, Z. Shen and C. Li, *Biosensors and Bioelectronics*, 2005, **20**, 2330–2334.
23 K. Rajdeo, T. Harini, K. Lavanya and N. W. Fadnavis, *Food and Bioproducts Processing*, 2016, **99**, 12–19.
24 J. Li, H. Wu, Y. Liang, Z. Jiang, Y. Jiang and L. Zhang, *Journal of Biomaterials Science, Polymer Edition*, 2013, **24**, 119–134.
25 J. Zdarta, A. S. Meyer, T. Jesionowski and M. Pinelo, *Catalysts*, 2018, **8**, 92.
26 Y. Ikeda, Y. Kurokawa, K. Nakane and N. Ogata, *Cellulose*, 2002, **9**, 369–379.

27 K. Nakane, T. Ogihara, N. Ogata and Y. Kurokawa, *Journal of Materials Research*, 2003, **18**, 672–676.
28 X. Jiang, S. Wang, L. Ge, F. Lin, Q. Lu, T. Wang, B. Huang and B. Lu, *RSC Advances*, 2017, **7**, 38965–38972.
29 X. Luo and L. Zhang, *Journal of Hazardous Materials*, 2009, **171**, 340–347.
30 Y. Li, H. Xiao, M. Chen, Z. Song and Y. Zhao, *Journal of Materials Science*, 2014, **49**, 6696–6704.
31 H. Asai, S. Kato, and K. Nakane, *Solid State Sciences*, 2019, **88**, 67–73.
32 S. Mandal, M. K. Sahu and R. K. Patel, *Water Resources and Industry*, 2013, **4**, 51–67.
33 Y. Lv, Z. L. Xu, H. Asai, N. Shimada and K. Nakane, *RSC Advances*, 2016, **6**, 21043–21047.
34 L.-J. Chen, J.-D. Liao, S.-J. Lin, Y.-J. Chuang and Y.-S. Fu, *Polymer*, 2009, **50**, 3516–3521.
35 X. Fu, H. Matsuyama and H. Nagai, *Journal of Applied Polymer Science*, 2008, **108**, 713–723.
36 J. Wang, W.-Z. Lang, H.-P. Xu, X. Zhang and Y.-J. Guo, *Chemical Engineering Journal*, 2015, **260**, 90–98.
37 K. Nakane, T. Kurita, T. Ogihara and N. Ogata, *Composites Part B: Engineering*, 2004, **35**, 219–222.
38 L.-J. Chen, J.-D. Liao, S.-J. Lin, Y.-J. Chuang and Y.-S. Fu, *Polymer*, 2009, **50**, 3516–3521.
39 K. Nakane, K. Mizutani, R. Zhang, K. Sugimoto and N. Ogata, *World Journal of Engineering*, 2012, **9**(3), 233-238.
40 J. Li, H.-Y. Qi and Y.-P. Shi, *Analytica Chimica Acta*, 2009, **651**, 182–187.
41 T. Yamaguchi, *Catalysis Today*, 1994, **20**, 199–217.
42K. Yuan, X. Jin, Z. Yu, X. Gan, X. Wang, G. Zhang, L. Zhu and D. Xu, *Ceramics International*, 2018, **44**, 282–289.
43 S. Buddee and S. Wongnawa, *Journal of Sol-Gel Science and Technology*, 2015, **75**, 152–163.
44 Q. Wang, X. Chen, K. Yu, Y. Zhang and Y. Cong, *Journal of Hazardous Materials*, 2013, **246**, 135–144.
45 A. H. Bhuiyan, T. Nagakawa and K. Nakane, *Journal of Applied Polymer Science*, 2021, **138**, 50164.

CHAPTER TWO

2. LITERATURE REVIEW

2.1 ORGANIC-INORGANIC HYBRID FIBERS

Organic/inorganic hybrid fibers (OIHFs) are attractive materials because they inherently have a large specific surface area and are flexible, and they also have special anisotropic properties, a variety of chemical compositions, and customizable hybrid structures. The diversity of keywords in OIHFs over the past 10 years has shown the broad family of materials with various attractions of components, the ability to form hierarchical structures and tunable and heterogeneous electronic properties are inherently powerful for a wide range of applications [1]. By incorporating organic and inorganic components in this new class of materials, a multifunctional hybrid with superior performance to single-component materials can be formed [2]. The combination of the outstanding properties of organic polymers (toughness, flexibility, and processability) and inorganic molecules (rigidity, heat resistance, and good mechanical strength) is capable to endure the requirements for a wide range of applications, such as catalyst carriers [3], electronics [4], adsorbents [5], and energy storage [6].

2.2 CLASSIFICATION OF ORGANIC-INORGANIC HYBRID STRUCTURE

Organic-inorganic hybrid polymers are classes of materials whose structure includes both organic and inorganic parts that interact with each other at the molecular level. These materials are divided into two classes based on the interaction between organic and inorganic components. In class, I, organic and inorganic are networked by weak interactions, such as hydrogen bonding, van der Waals, and weak electrostatic bonds between them, and in class II, these two components are bonded together through strong covalent or coordinative bonds [7].

2.3 SYNTHESIS OF ORGANIC-INORGANIC HYBRID STRUCTURE

2.3.1 Sol-Gel Process

Sol-gel process, the first successful commercial organic-inorganic hybrid structure provider, is a cheap and low-temperature method for producing transparent and homogenous solid structures with purity from small molecules and suitable to control the chemical composition of products [5]. This process could be done in both water and organic solvents and metal halides [8] and metal alkoxides [9,10] were generally used as precursors. These materials undergo several condensation and hydrolysis reactions, which result in the formation of sols via nucleophilic substitution mechanisms. A colloidal solution known as ‘sol’ comprises weak interactions between individual molecules, which eventually cross-link to form an integrated network (wet gel). Further drying processes convert this structure into a gel [5].

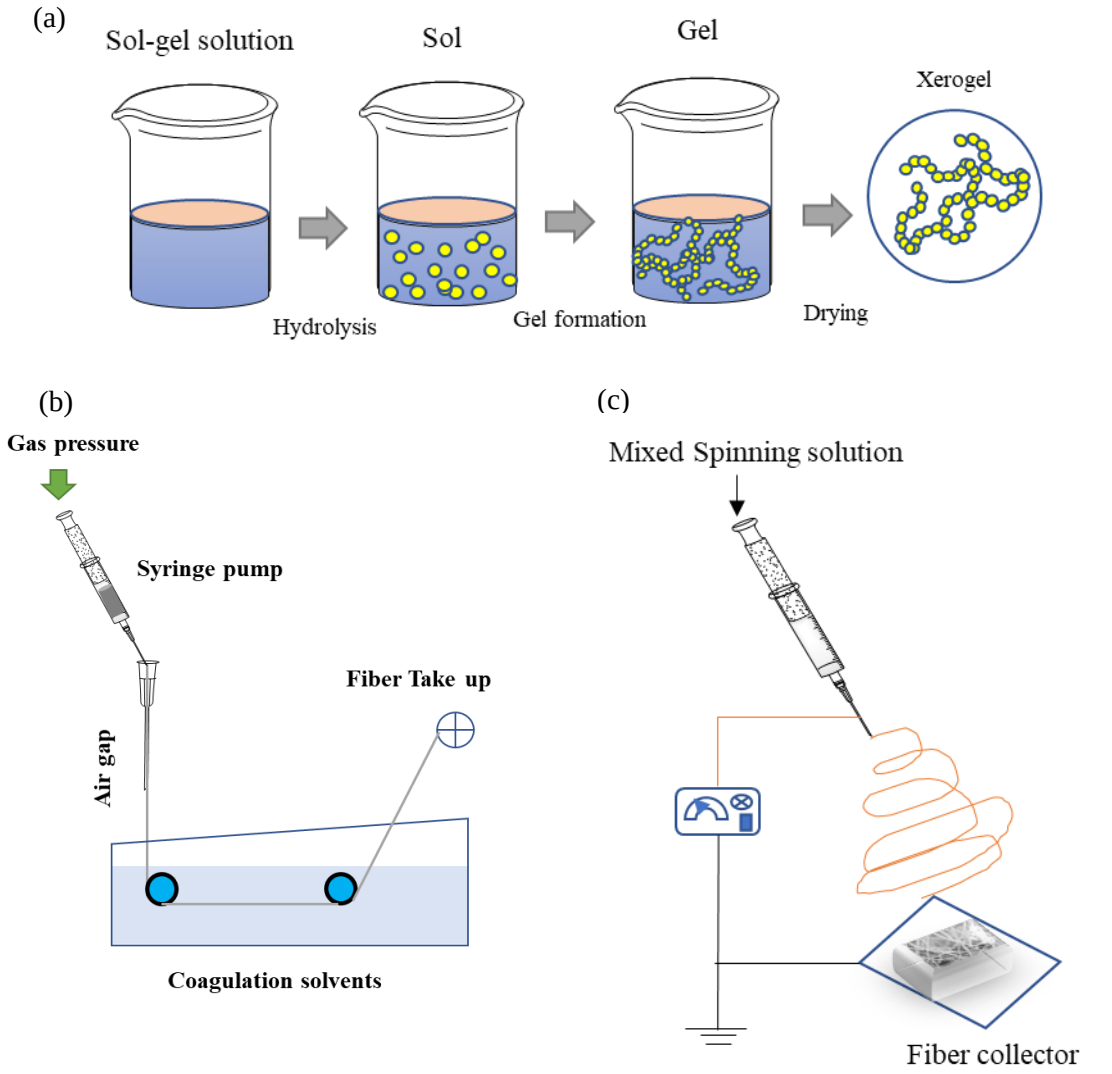

Fig. 2.1 Common systems of preparing organic-inorganic hybrid structures; (a) sol-gel process, (b) dry-jet wet spinning, and (c) electrospinning.

2.3.2 Wet Spinning

Wet spinning fabrication techniques may use numerous draws or baths to enhance molecular alignments and orientation. A new form of wet spinning, referred to as dry-jet wet spinning has been established [11]. Studies report that dry-jet wet spinning can result in better molecular alignment compared to conventional wet spinning. Fiber characteristics, including diameter, orientation, and morphology, can be changed by adjusting variables like the spinneret's diameter, the concentration of the polymer solution, and the flow velocity.

2.3.3 Self-Assembly Process

This approach offers a good system for accurately controlling the quantity and spatial distribution of organic/inorganic species. Numerous studies have been conducted on the noncovalently connected micelle (NCCM) method, which uses complementary pairings of polymers as building blocks to direct the production of fibrous nanostructures [12].

2.3.4 Electrospinning

Electrospinning is a polymer process technique that uses electrostatic forces to uniaxially stretch a viscoelastic jet derived from a polymer solution or melt, to produce continuous nanometric and micrometric fibers, typically assembled into nonwoven mats [13]. It is well known that electrospun polymeric fibers improve the structural performance of composite polymeric materials [14]. Electrospun materials can now be employed in a wider range of applications because of the development of nanofibers consisting of substances other than polymers, including composite organic-inorganic systems, carbon, ceramics, metal oxides, and metal oxide nanoparticles. The key benefit of creating hybrid nanomaterials using the electrospinning method is because: (1) long and continuous fibers with the combination of different functionalities and (2) the capability of controlling the structure (from nano to micrometer scales), the concentration, and the spatial distribution of the components [15].

2.4 COMMON ORGANIC-INORGANIC HYBRID STRUCTURE FOR ENZYME IMMOBILIZATION

The contacts between an enzyme and support may typically be stabilized using hybrids and composites, and these materials also increase the mechanical stability and stability of biocatalysts under reaction circumstances. It should be noted that hybrid supports in general offer biomolecules a suitable environment that encourages the immobilized enzyme to retain its high catalytic characteristics, allows the biocatalytic system to be reused, and secures it from conformational changes during storage [16]. To generate hybrid or composite supports for the immobilization of enzymes, a wide range of materials of both organic and inorganic origin can be combined. The most often utilized inorganic precursors are silica, and inorganic oxides including zinc and titanium oxides, minerals, carbon compounds, and magnetic nanoparticles [17–20]. They are compatible with synthetic polymers, for example, CA, polyacrylonitrile (PAN), polyethyleneimine, and polyvinyl alcohol (PVA) [21–23] as well as with biopolymers such as chitosan, lignin, and alginate [24,25]. Enzymes like hydrolases, oxidoreductases, and transferases are immobilized in these materials by adsorption or covalent bonding but the encapsulation [26] and entrapment [27] of other enzymes in these carriers have also been reported. For instance, Zhao et al. established immobilization of glucose isomerase on silica-chitosan hybrid via simple in situ encapsulation for the conversion of glucose to fructose by combining the stability and mechanical resilience of silica with the biocompatibility and gelation capabilities of chitosan [28]. Chang et al. combined natural clay composed of montmorillonite and layer silicates with a chitosan hybrid, further cross-linked with glutaraldehyde for the immobilization of β-glucosidase [29]. Nakane et al. reported about the entrapment of invertase on hybrid gel fiber of CA-zirconium alkoxide by sol-gel process for the hydrolysis of sucrose [30].

Table 2.1 Selected examples of organic-inorganic hybrid materials applied for enzyme immobilization.

Support Material	Cross-Linking Agent	Immobilization Type	Immobilized Enzyme	References
Silica-lignin	-	Adsorption	Glucose oxidase	[18]
Sodium alginate-CNS	-	Entrapment	Glucose oxidase	[31]
SiO_2-DAS	-	Cross-link	Tyrosinase	[20]
CA-$Ti(OPr)_4$	-	Entrapment	β-galactosidase, α-chymotrypsine	[32]
CA-$Zr(OBu)_4$	-	Entrapment	β-galactosidase	[33]
CA-$Zr(OBu)_4$	-	Entrapment	Lipase	[22]
CA-$Zr(OBu)_4$	-	Entrapment	Urease	[34]

2.5 INORGANIC AND ORGANIC-INORGANIC HYBRID STRUCTURES BASED ON TIO_2 FOR ORGANIC POLLUTANTS REMOVAL

In several applications, including the photocatalytic destruction of pollutants and the photocatalytic synthesis of organic compounds, titanium dioxide (TiO_2) nanostructured materials have gained a lot of interest. The investigations are mainly focused on the design and synthesis of crystalline TiO_2 with tailored nanostructures, leading to the formation of diverse TiO_2 nanocrystals with controllable size, shape, defects, dopants, and hybridization which provides an excellent platform for not only revealing the relationship between structure and property but also improving the performances in their practical applications [35]. Crystalline TiO_2 can be used for photocatalytic reactions for the elimination of pollutants because of its abundance on Earth, low toxicity, chemical and thermal stability, and strong resistance to photo-corrosion. At the same time, numerous modification techniques have been used to enhance the photochemical characteristics of TiO_2, attempting to reduce the band gap and lengthen the duration of photogenerated charge carriers, such as hybridization with new species (including narrow band gap semiconductors, carbon materials, noble metals, and organic dyes), metal ion/nonmetal ion doping, and construction of defective TiO_2 with oxygen vacancies and/or trivalent titanium [36–40]. On the other hand, amorphous TiO_2 (am-TiO_2) has a typical long-range atomic disarray structure and isotropic physical and chemical properties, which may allow them to demonstrate high activity in photocatalysis due to better light harvesting and increased specific surface area. [41]. For instance, am-TiO_2 can show adsorption and photoactive performance under visible light irradiation for yellow color [35]. Furthermore, Wang et al. have reported on visible-light-induced photodegradation of Rhodamine B (Rh-B) by amorphous titania [42]. Buddee et al. described the removal of dyes by curcumin-sensitized am-TiO_2 under visible light irradiation [43]. Asai et al. reported on cellulose acetate (CA) fiber crosslinked am-TiO_2 (i.e. CA–amTiO_2), decomposed organic dyes, and reducing Cr(VI) by visible light irradiation [44]. In other respects, Lv et al. and

Nakane et al. developed mesoporous TiO_2 nanotubes prepared by electrospun PVA-titanium (IV) isopropoxide template, applied for photocatalytic MB removal [45,46].

2.6 POLYVINYL BUTYRAL (PVB)

Polyvinyl butyral (PVB) is a non-toxic, odorless, and environmentally benign polymer, and is an outstanding organic component for the development of organic/inorganic hybrid compounds [47]. PVB exhibits good mechanical properties, great adhesion to particles, and excellent dielectric properties, making it stable in aqueous environments [48]. PVB is a random copolymer, (**Scheme 2.1**) that is entirely amorphous and could be synthesized in an acidic medium from the reaction of polyvinyl alcohol and butyraldehyde. PVB was found to be polyhydroxy and polyacetal since it contains a predominant proportion of butyral, hydroxyl, and (very less) acetyl groups. Among the groups present in PVB moiety, the vinyl alcohol group is hydrophilic whereas the vinyl butyral group is hydrophobic. PVB may interact favorably with other macromolecules due to its non-polar and polar components, making it compatible with both hydrophilic and hydrophobic components. Additionally, it might make it easier to use PVB as a copolymer with potential miscibility where polymers are made up of quite different groups [49]. The hydrophilicity of PVB makes it a desirable material for creating a hollow fiber membrane [50]. Besides, PVB is soluble in polar solvents, which increases its ionic conductivity, resulting in less susceptibility to splashing by non-polar substances. [51,52].

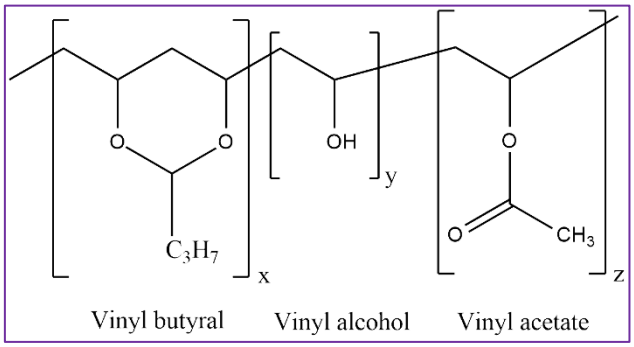

Scheme 2.1 Structural formula of polyvinyl butyral representing different functional groups.

2.6.1 Application of PVB, PVB-metal oxide blends, and others as hollow fiber membrane

Polymeric composite membranes have so far involved a variety of polymers including polyvinylidene fluoride (PVDF), polyethersulfone (PES), polysulfone (PSF), polyvinyl alcohol (PVA), polyacrylonitrile (PAN) and cellulose acetate (CA) [53–57]. However, compared to the above materials, increased surface hydrophilicity of PVB can effectively restrain membrane fouling and promote permeability. Hence numerous reports showed the development of PVB membranes by thermally-induced phase separation (TIPS) methods [58–61], non-solvent-induced phase separation (NIPS) methods [62–64], and wet spinning methods [65–67].

Furthermore, several reports showed their potential to immobilize different enzymes in PVB and PVB-prone membranes and nanostructures. PVB as an enzyme immobilization support was employed by Zhang et al. [68], and Jiang et al.[69] to produce many types of nanoparticles enhanced glucose oxidase (GOD) electrodes, such as hydrophobic SiO_2 nanoparticles and Au nanoparticles

enhanced GOD electrodes. Dong et al. developed a PVB nanofiber membrane for lipase immobilization using electrostatic spinning technology [70].

Metal-organic framework (MOF) is a kind of porous crystal material developed by metal ions and multifunctional organic ligands. Applications in adsorption and catalysis are possible for metalorganic matrix materials. Liu et al. reported on the MIL-88/PVB electrospun nanofiber for the degradation of TC-HCl [71]. Wang et al. synthesized a new hydrophilic boehmite-PVB/PVDF blended membrane supported by nano zero-valent iron for the removal of Cr(VI) [72]. In addition, a facile fabrication process is developed to prepare PVB-PVA blend polymer nanocomposite for the simultaneous removal of heavy metal ions from aqueous solutions [73].

REFERENCES

1 F. Zhang, P. C. Sherrell, W. Luo, J. Chen, W. Li, J. Yang and M. Zhu, *Advanced Science*, 2021, **8**, 2102859.

2 X. Jiang, S. Wang, L. Ge, F. Lin, Q. Lu, T. Wang, B. Huang and B. Lu, *RSC Advances*, 2017, **7**, 38965–38972.

3 M. H. Valkenberg and W. F. Hölderich, *Catalysis Reviews*, 2002, **44**, 321–374.

4 P. Reiss, E. Couderc, J. De Girolamo and A. Pron, *Nanoscale*, 2011, **3**, 446–489.

5 B. Samiey, C.-H. Cheng and J. Wu, *Materials*, 2014, **7**, 673–726.

6 P. Gómez-Romero, O. Ayyad, J. Suárez-Guevara and D. Muñoz-Rojas, *Journal of Solid State Electrochemistry*, 2010, **14**, 1939–1945.

7 C. Sanchez, B. Julián, P. Belleville and M. Popall, *Journal of Materials Chemistry*, 2005, **15**, 3559–3592.

8 J. N. Hay and H. M. Raval, *Chemistry of Materials*, 2001, **13**, 3396–3403.

9 J. Wen and G. L. Wilkes, *Chemistry of Materials*, 1996, **8**, 1667–81.

10 X.-F. Wen, K. Wang, P.-H. Pi, J.-X. Yang, Z.-Q. Cai, L. Zhang, Y. Qian, Z.-R. Yang, D. Zheng and J. Cheng, *Applied Surface Science*, 2011, **258**, 991–998.

11 K. G. DeFrates, R. Moore, J. Borgesi, G. Lin, T. Mulderig, V. Beachley and X. Hu, *Nanomaterials*, 2018, **8**, 457.

12 H. Cui, Z. Chen, S. Zhong, K. L. Wooley and D. J. Pochan, *Science*, 2007, **317**, 647–650.

13 S. Agarwal, A. Greiner and J. H. Wendorff, *Progress in Polymer Science*, 2013, **38**, 963–991.

14 A. Zucchelli, M. L. Focarete, C. Gualandi and S. Ramakrishna, *Polymers for Advanced Technologies*, 2011, **22**, 339–349.

15 C. Gualandi, A. Celli, A. Zucchelli, M.L Focarete, *Organic-Inorganic Hybrid Nanomaterials; Advances in Polymer Science*, 2014, **267**, 87-142.

16 X.-Y. Yang, G. Tian, N. Jiang and B.-L. Su, *Energy & Environmental Science*, 2012, **5**, 5540–5563.

17 M. Amirbandeh and A. Taheri-Kafrani, *International Journal of Biological Macromolecules*, 2016, **93**, 1183–1191.

18 A. Jędrzak, T. Rębiś, Lukasz Klapiszewski, J. Zdarta, G. Milczarek and T. Jesionowski, *Sensors and Actuators B: Chemical*, 2018, **256**, 176–185.

19 J. Li, H. Wu, Y. Liang, Z. Jiang, Y. Jiang and L. Zhang, *Journal of Biomaterials Science, Polymer Edition*, 2013, **24**, 119–134.

20 J. Zdarta, A. S. Meyer, T. Jesionowski and M. Pinelo, *Catalysts*, 2018, **8**, 92.

21 A. E. Lima Barros, A. M. P. Almeida, L. B. Carvalho Jr and W. M. Azevedo, *Brazilian Journal of Medical and Biological Research*, 2002, **35**, 459–463.
22 K. Nakane, K. Kuranobu, T. Ogihara, N. Ogata and Y. Kurokawa, *Sen'i Gakkaishi*, 2003, **59**, 99–103.
23 L.-S. Wan, B.-B. Ke and Z.-K. Xu, *Enzyme and Microbial Technology*, 2008, **42**, 332–339.
24 N. Shah, M. Ul-Islam, W. A. Khattak and J. K. Park, *Carbohydrate Polymers*, 2013, **98**, 1585–1598.
25 J. Zdarta, L. Klapiszewski, A. Jedrzak, M. Nowicki, D. Moszynski and T. Jesionowski, *Catalysts*, 2016, **7**, 14.
26 P. Vatsyayan, S. Bordoloi, and P. Goswami, *Biophysical Chemistry*, 2010, **153**, 36–42.
27 Y. Ikeda and Y. Kurokawa, *Journal of the American Oil Chemists' Society*, 2001, **78**, 1099–1103.
28 H. Zhao, Q. Cui, V. Shah, J. Xu and T. Wang, *Journal of Molecular Catalysis B: Enzymatic*, 2016, **126**, 18–23.
29M.-Y. Chang, H.-C. Kao and R.-S. Juang, *International Journal of Biological Macromolecules*, 2008, **43**, 48–53.
30 K. Nakane, T. Ogihara, N. Ogata and Y. Kurokawa, *Journal of Applied Polymer Science*, 2001, **81**, 2084–2088.
31 E. Han, X. Li, J.-R. Cai, H.-Y. Cui, and X.-A. Zhang, *Analytical Sciences*, 2014, **30**, 897–902.
32 Y. Ikeda, Y. Kurokawa, K. Nakane and N. Ogata, *Cellulose*, 2002, **9**, 369–379.
33 K. Nakane, T. Ogihara, N. Ogata and Y. Kurokawa, *Journal of Materials Research*, 2003, **18**, 672–676.
34 K. Nakane, K. Takahashi, F. Suzuki and Y. Kurokawa, *Sen'i Gakkaishi*, 1999, **55**, 563–568.
35 S. Sun, P. Song, J. Cui and S. Liang, *Catalysis Science & Technology*, 2019, **9**, 4198–4215.
36 C. W. Dunnill and I. P. Parkin, *Dalton Transactions*, 2011, **40**, 1635–1640.
37 B. Roose, S. Pathak, and U. Steiner, *Chemical Society Reviews*, 2015, **44**, 8326–8349.
38 J. Su, X.-X. Zou, Y.-C. Zou, G.-D. Li, P.-P. Wang and J.-S. Chen, *Inorganic Chemistry*, 2013, **52**, 5924–5930.
39 J. Su, X. Zou and J.-S. Chen, *RSC Advances*, 2014, **4**, 13979–13988.
40 J. Zhang, Y. Wu, M. Xing, S. A. K. Leghari and S. Sajjad, *Energy & Environmental Science*, 2010, **3**, 715–726.
41 S. Zeng, L. Zhang, W. Wang, D. Shao, and H. Hao, *Physical Chemistry Chemical Physics*, 2017, **19**, 29053–29056.
42 Q. Wang, X. Chen, K. Yu, Y. Zhang and Y. Cong, *Journal of Hazardous Materials*, 2013, **246**, 135–144.
43 S. Buddee and S. Wongnawa, *Journal of Sol-Gel Science and Technology*, 2015, **75**, 152–163.
44 H. Asai, S. Kato, and K. Nakane, *Solid State Sciences*, 2019, **88**, 67–73.
45 Y. Lv, Z. L. Xu, H. Asai, N. Shimada and K. Nakane, *RSC Advances*, 2016, **6**, 21043–21047.
46K. Nakane, N. Shimada, T. Ogihara, N. Ogata and S. Yamaguchi, *Journal of Materials Science*, 2007, **42**, 4031–4035.
47 L.-J. Chen, J.-D. Liao, S.-J. Lin, Y.-J. Chuang and Y.-S. Fu, *Polymer*, 2009, **50**, 3516–3521.
48 Y. Akinay, F. Hayat and B. Çolak, *Materials Chemistry, and Physics*, 2019, **229**, 460–466.
49 P. Kumar, N. Khan, and D. Kumar, *Green Chemical Technology Letters*, 2016, **2**, 185–194.
50 Y.-R. Qiu and H. Matsuyama, *Desalination*, 2010, **257**, 117–123.
51 M. A. El-Sherbiny and N. S. A. El-Rehim, *Polymer Testing*, 2001, **20**, 371–378.

52 T. Guinovart, G. A. Crespo, F. X. Rius and F. J. Andrade, *Analytica Chimica Acta*, 2014, **821**, 72–80.
53 S. Majeed, D. Fierro, K. Buhr, J. Wind, B. Du, A. Boschetti-de-Fierro and V. Abetz, *Journal of Membrane Science*, 2012, **403**, 101–109.
54 F. Peng, F. Pan, H. Sun, L. Lu and Z. Jiang, *Journal of Membrane Science*, 2007, **300**, 13–19.
55 S. Qiu, L. Wu, X. Pan, L. Zhang, H. Chen and C. Gao, *Journal of Membrane Science*, 2009, **342**, 165–172.
56 A. Rahimpour, M. Jahanshahi, S. Khalili, A. Mollahosseini, A. Zirepour and B. Rajaeian, *Desalination*, 2012, **286**, 99–107.
57 J. Zhang, Z. Xu, M. Shan, B. Zhou, Y. Li, B. Li, J. Niu and X. Qian, *Journal of Membrane Science*, 2013, **448**, 81–92.
58 X. Fu, H. Matsuyama, M. Teramoto, and H. Nagai, *Separation and Purification Technology*, 2005, **45**, 200–207.
59 X. Fu, H. Matsuyama, M. Teramoto and H. Nagai, *Separation and Purification Technology*, 2006, **52**, 363–371.
60 X. Ma, Q. Sun, Y. Su, Y. Wang and Z. Jiang, *Separation and Purification Technology*, 2007, **54**, 220–226.
61 Y.-R. Qiu, N. A. Rahman, and H. Matsuyama, *Separation and Purification Technology*, 2008, **61**, 1–8.
62 X. Fu, H. Matsuyama and H. Nagai, *Journal of Applied Polymer Science*, 2008, **108**, 713–723.
63 F. Shen, X. Lu, X. Bian, and L. Shi, *Journal of Membrane Science*, 2005, **265**, 74–84.
64 P. Zhang, Y. Wang, Z. Xu and H. Yang, *Desalination*, 2011, **278**, 186–193.
65 W.-Z. Lang, J.-P. Shen, Y.-T. Wei, Q.-Y. Wu, J. Wang and Y.-J. Guo, *Chemical Engineering Journal*, 2013, **225**, 25–33.
66 W.-Z. Lang, J.-P. Shen, Y.-X. Zhang, Y.-H. Yu, Y.-J. Guo and C.-X. Liu, *Journal of Membrane Science*, 2013, **430**, 1–10.
67 J. Wang, W.-Z. Lang, H.-P. Xu, X. Zhang and Y.-J. Guo, *Chemical Engineering Journal*, 2015, **260**, 90–98.
68 Y. Zhang and J. Shen, *International Journal of Hydrogen Energy*, 2007, **32**, 17–23.
69 F. Tang and L. Jiang, *Annals of the New York Academy of Sciences*, 1998, **864**, 538–543.
70 Y. Dong and F. Ma, *Journal of Nanoelectronics and Optoelectronics*, 2018, **13**, 1041–1047.
71 W. Liu, J. Zhou, L. Ding, Y. Yang and T. Zhang, *Chemical Physics Letters*, 2020, **749**, 137431.
72 X. Wang, T. Wang, J. Ma, H. Liu and P. Ning, *Separation and Purification Technology*, 2018, **205**, 74–83.
73 H. Azad, M. Mohsennia, C. Cheng and A. Amini, *Journal of Environmental Chemical Engineering*, 2021, **9**, 106214.

CHAPTER THREE

3. EXPERIMENTAL

3.1 MATERIALS

Materials used in the current study were briefly described in the published journal articles in chapters Four, Five, and Six. The detailed specification with relevant information on all the materials is also explained in this section. They are subdivided into some groups, including polymers, liquid organic and inorganic chemicals, enzymes, and dyes used for various experimental investigations.

3.1.1 Polymers

Different types of polyvinyl butyral (PVB) are used in this study which is described in **Table 3.1.**

Table 3.1 Detail specification of PVB[a].

Types of PVB	Molecular weight	Degree of acetalization	Solid (wt.%)	Company name
PVB B60T	50–60 kDa	69%–75%	≥ 97.5%	Kuraray Co. Ltd., Japan
PVB B60H	50–60 kDa	75%–81%	≥ 97.5%	Kuraray Co. Ltd., Japan
PVB B60HH	50–60 kDa	82%–88%	≥ 97.5%	Kuraray Co. Ltd., Japan

a Information collected from the Mowital technical datasheet.

3.1.2 Organic and inorganic chemicals

Several chemicals and enzymes (**Table 3.2**) were employed for the preparation of PVB-metal oxides hybrid fiber and their application in the field of enzyme immobilization and dye removal.

Table 3.2 Name of the chemicals and their suppliers.

Name of chemicals	Suppliers
Zirconium (IV) butoxide	Fujifilm Wako Pure Chemical Industries, Ltd., Japan
Titanium (IV) isopropoxide	Fujifilm Wako Pure Chemical Industries Ltd., Japan
Methanol	Nacalai Tesque Inc., Japan
Ethanol	Nacalai Tesque Inc., Japan
Acetone	Nacalai Tesque Inc., Japan
Hexane	Nacalai Tesque Inc., Japan
NaCl	Kanto Chemical Co., Ltd., Japan
$CaCl_2$	Nacalai Tesque Inc., Japan
Lactose monohydrate	Nacalai Tesque Inc., Japan
Citronellol	Nacalai Tesque Inc., Japan
Glucose-B test kit	Fujifilm Wako Pure Chemical Industries, Ltd., Japan
Novozym-435	MIK Pharm Co., Ltd., Japan
Linalool	Tokyo Chemical Industry, Ltd., Japan

3.1.3 Features of the enzymes used in this study

β-galactosidase and lipase are the two types of enzymes that have been used to explore the immobilization property of PVB-ZrO_2 hybrid fiber. β-galactosidase is a tetramer comprising four identical polypeptide chains, each of which has 1023 amino acids, which come together to form five distinct structural domains [1]. Substrates of different β-galactosidases include ganglioside GM1, lactosylceramides, lactose, and various glycoproteins. In contrast, lipase B from (EC 3.1.1.3; *Candida antarctica*) is an effective catalyst for the synthesis of esters of citronellol.

3.1.4 Dyes used for the measurement of the removal performance of PVB-amTiO_2 hybrid fiber

Several simulated dye structures (**Scheme 3.1**) namely methylene blue, methyl orange, and rhodamine B have been used to measure the adsorption and dye degradation behavior of PVB-TiO_2 hybrid fiber.

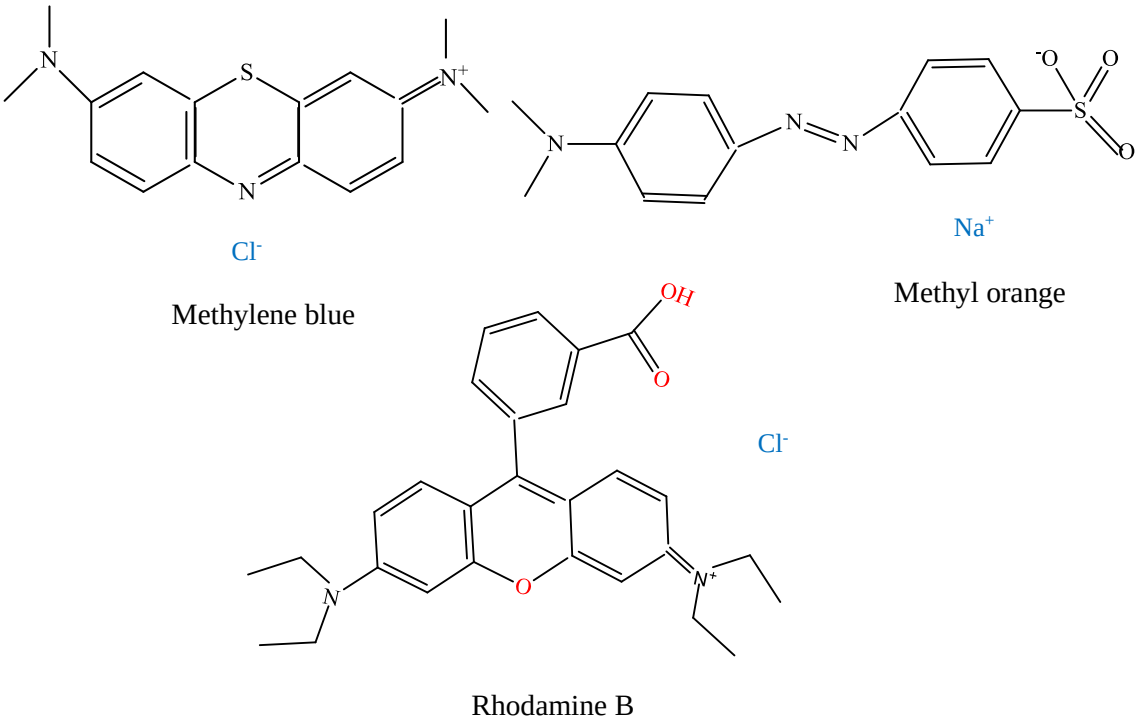

Scheme 3.1 Chemical structures of Methylene blue, Methyl orange, and Rhodamine B dyes.

3.2 METHODS

The detailed methods of the current study were described in the published journal articles [2–4] included in chapters Four, Five, and Six.

3.2.1 Preparation of PVB-metal alkoxides (PVB-Zr alkoxide, PVB-Ti alkoxide) hybrid hollow fiber by an air gap (dry-jet wet) spinning

The preparation of the PVB-Zr alkoxide and PVB-Ti alkoxide hybrid fiber was prepared by a simple air gap spinning method (**Fig. 3.1**) where the spinning dope of PVB is passed through an organic solvent-metal alkoxides coagulation bath with predetermined N_2 gas pressure, air gap

distance, and rotational speed of coagulation liquid. However, a fixed amount of enzymes (β-galactosidase and lipase) is added with spinning dope when the immobilized enzyme activity on PVB-metal alkoxides needs to measure [4].

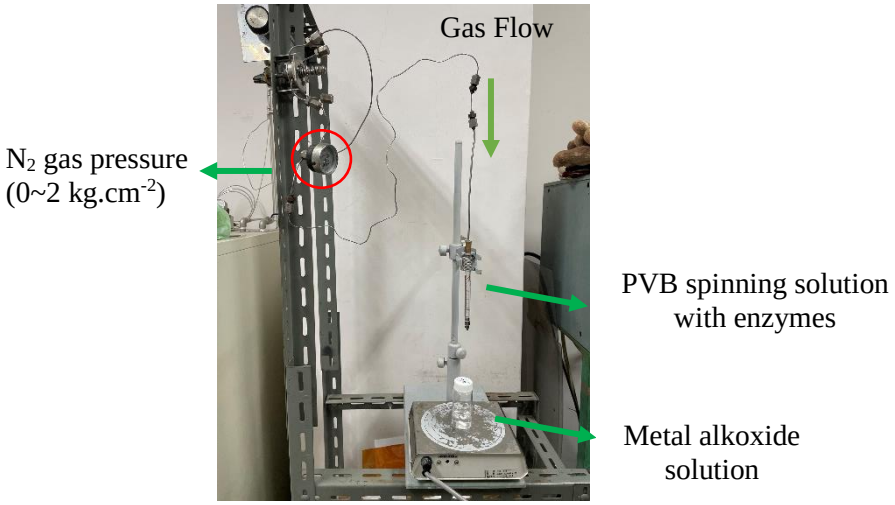

Fig. 3.1 Photograph of the preparation of enzyme immobilized PVB-Zr alkoxide hybrid hollow fiber.

3.2.2 Evaluation of β-galactosidase enzyme activity

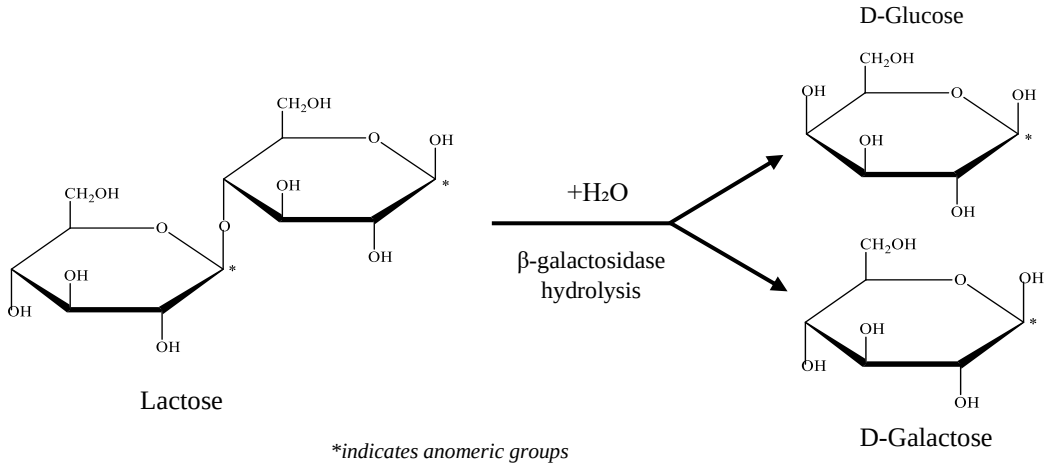

Scheme 3.2 Schematic illustration of lactose hydrolysis [5] reactions.

The activity of the enzyme was evaluated by the amount of hydrolysis of lactose to glucose shown in reaction **Scheme 3.2**. Lactose degradation was measured using a commercially available glucose-B (color reagent) measurement kit. The detailed activity of the β-galactosidase enzyme is explained in Chapter Five.

3.2.2.1 Substrate concentration dependence

The free enzyme (0.003 g) and the immobilized enzyme (0.1 g) were immersed in 5 mL of lactose solution at 37.5 ° C and pH 4.6 for 30 minutes. Each concentration of the lactose solution is 0.01

M (lactose: 0.036 g, citrate buffer: 10 mL), 0.03 M (lactose: 0.108 g, citrate buffer: 10 mL), 0.05 M (lactose: 0.18 g, citrate buffer: 10 mL), 0.1 M (Lactose: 0.36 g, citrate buffer: 10 mL), 0.15 M (lactose: 0.54 g, citrate buffer: 10 mL), 0.2 M (lactose: 0.72 g, citrate buffer: 10 mL) prepared. For comparison, experiments were performed under the same conditions using the Ca-alginate beads (0.2 to 0.35 g) is also prepared.

3.2.2.2 Repeatability

Enzyme-immobilized PVB-ZrO_2 hybrid fiber (0.1 g) in 5 mL of substrate solution (pH: 4.6) prepared in 0.1 M (lactose: 0.36 g, citrate buffer: 10 mL), and react for 30 minutes at 37.5 ° C. After that, it was impregnated with a citrate buffer solution (pH: 4.6) for 5 minutes, washed, and used again for the same reaction bath. This operation was repeated 10 times. For comparison, experiments were performed under the same conditions using the Ca-alginate beads (0.2 to 0.35 g).

3.2.2.3 Temperature dependence

The free enzyme (0.003 g) and the immobilized enzyme (0.1 g) were immersed in a 5 mL (0.1 M, Lactose: 0.36 g, citrate buffer: 10 mL) lactose solution at a specified temperature of pH 4.6 for 30 minutes. The temperature of the solution was set to 30 °C, 37.5 °C, 40 °C, 50 °C, 55 °C, 60 °C, 65 °C, 70 °C, and 80 °C, respectively. For comparison, experiments were performed under the same conditions using the Ca-alginate beads (0.2 to 0.35 g). After that, the glucose-B-test kit was used to measure the glucose concentration, and then the activity was calculated.

3.2.2.4 pH dependence

The free enzyme (0.003 g) and the immobilized enzyme (0.1 g) were immersed in a 5 mL (0.1 M, Lactose: 0.36 g, citrate buffer: 10 mL) lactose solution at 37.5 °C for 30 minutes. The pH was adjusted to 3, 3.5, 4, 4.5, 5, 5.5, 6, and 6.5, respectively. For comparison, experiments were performed under the same conditions using the Ca-alginate beads (0.2 to 0.35 g). After that, the glucose-B-test kit was used to measure the glucose concentration, and then the activity was calculated.

3.2.2.5 Measurement principle of enzyme activity

When the hydrolyzed glucose sample of **Scheme 3.2** is mixed with color reagent (glucose-B), β-D-glucose is oxidized by the action of glucose oxidase (GOD) to produce hydrogen peroxide. In the presence of peroxidase (POD), hydrogen peroxide formed yields a red pigment (**Scheme 3.3)** by oxidation condensation with phenol and 4-aminoantipyrine. The glucose concentration is obtained by measuring the absorbance (at 505 nm) of the red color in UV-Vis spectra. Afterward, β-galactosidase activity (A) was measured by the following equation (3.1) where the resultant glucose concentrations (X) were obtained from the absorbance versus concentration curve.

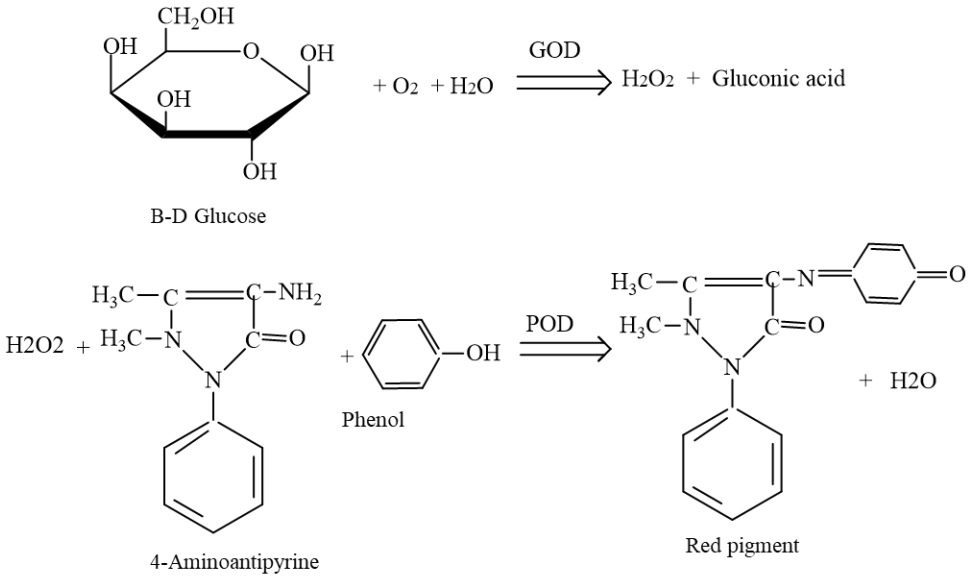

Scheme 3.3 Reaction mechanism of Glucose-B kit.

A (μmol/mL/min/mg-enzyme) = X (Concentration of glucose in mg/dl) × 1/M_w of glucose × 1/ reaction time (min) × solution amount (ml) × 1/enzyme amount (g) ---------- (3.1)

3.2.2.6 Determination of kinetic parameters

The obtained substrate concentration-activity curves were converted to Eadie-hofstee plots to determine the Michaelis-Menten constant (K_m) and the maximum reaction rate (V_{max}). The formula of Michaelis–Menten is in equation (3.2).

$$V_0 = V_{max}\,[S]/(K_m + [S])\text{---------- (3.2)}$$

The modified Eadie-Hofstee Plot from Michaelis–Menten formula is in equation (3.3)

$$V_0 = -K_m\,(V_0/[S]) + V_{max}\text{---------- (3.3)}$$

where [S] is substrate concentration and V_0 is the reaction velocity.

3.2.3 Evaluation of lipase enzyme activity

The activity was evaluated based on the amount of citronellol acetate synthesized using immobilized lipase as a catalyst. The reaction formula is shown in **Scheme 3.4**. The ester synthesis amount was measured by an internal standard method using gas chromatograph GC-12A manufactured by Shimadzu Corporation.

The analysis conditions of gas chromatography are shown below:
Detection method: FID (Hydrogen flame ionization detector)
Injection temperature: 250 ℃
Column temperature: 130 ℃
Column length: 1.8 m
Column packing material: Polyethylene glycol (PEG) 20 M

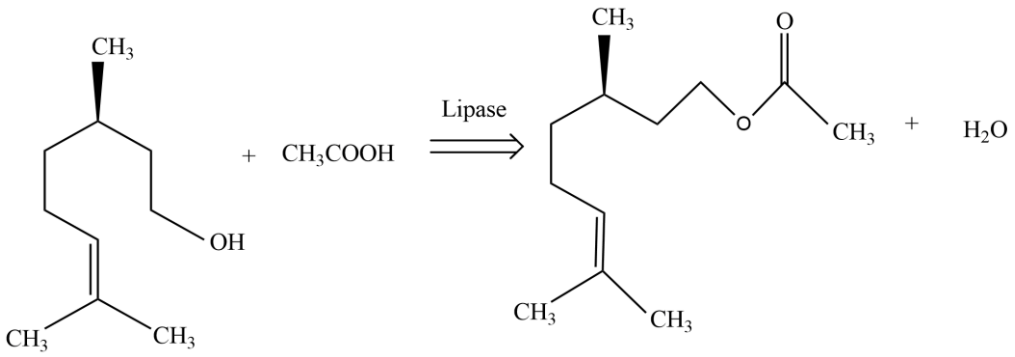

Citronellol Citronellol acetate

Scheme 3.4 Esterification reaction of citronellol by immobilized lipase.

In gas chromatography, the value of the peak area varies depending on the sample volume and reaction time. Therefore, along with citronellol, linalool was used as an internal standard, because it did not change regardless of the reaction. The peak ratio between citronellyl acetate and linalool in the chromatogram obtained from the following equation (3.4), was determined and utilized as an enzyme activity index.

Peak area ratio (PA ratio) = Citronellyl acetate area/Linalool area ---------- (3.4)

3.2.3.1 Preparation of calibration curve and calculation of enzyme activity and ester synthesis conversion

To determine the concentration of citronellyl acetate from the PA ratio, the PA ratio of each concentration of citronellyl acetate was measured, and a calibration curve was prepared. PA has obtained from gas chromatography after mixing 10 ml of hexane, 1 mol/L of citronellol, 0.5 mol/L of acetic acid, and 0.1 ml of linalool, and then calculating the concentration of citronellyl acetate using the prepared calibration curve. The activity (A) and conversion (C) were calculated from the following equations (3.5) and (3.6).

A (μmol/mL/min/mg-enzyme) = X (concentration of citronellyl acetate) × 1/(reaction time) × 1/(amount of enzyme) ---------- (3.5)

Conversion (%) = (mol of citronellyl acetate/mol of acetic acid) × 100 ---------- (3.6)

3.2.3.2 Reaction time dependence

The free enzyme (0.003 g) and the immobilized enzyme (0.1 g) were immersed in a substrate solution at 30 °C, and the conversion is measured at regular intervals. The substrate solution was adjusted to 10 ml of hexane, 0.1 mol/L of acetic acid, 0.2 mol/L of citronellol, and 0.1 ml of linalool.

3.2.3.3 Reaction temperature dependence

The free enzyme (0.003 g) and the immobilized enzyme (0.1 g) were immersed in a substrate solution at a specified temperature for 20 hrs, and the activity was measured. The temperature of the solution was adjusted to 30 °C, 40 °C, 50 °C, 60 °C, 70 °C, and 80 °C. The substrate solution

was adjusted to 10 ml of heptane solvent, 0.1 mol/L of acetic acid, 0.2 mol/L of citronellol, and 0.1 ml of linalool.

3.2.3.4 Repeatability

The free enzyme (0.003 g) and the immobilized enzyme (0.1 g) were immersed in a substrate solution at 30 °C for 20 hrs, and the activity was measured. After that, it was washed with hexane and reused for the reaction. The substrate solution was adjusted to 10 ml of hexane, 0.1 mol/L of acetic acid, 0.2 mol/L of citronellol, and 0.1 ml of linalool.

3.2.3.5 Water concentration dependence

The free enzyme (0.003 g) and the immobilized enzyme (0.1 g) were immersed in a substrate solution at 30 °C for 20 hrs, and the activity was measured. The substrate solution was fixed at 0.1 mol/L acetic acid, 0.2 mol/L citronellol, 0.1 ml linalool, and a water concentration of 10 wt.% (Hexane: 9 g, water: 1 g), 20 wt.% (Hexane: 8 g, water: 2 g), and 30 wt.% (Hexane: 7 g, water: 3 g) were adjusted.

3.3 CHARACTERIZATION AND PERFORMANCE MEASUREMENT OF THE MATERIALS

3.3.1 Morphological analysis

The surface morphology of the fiber was analyzed by using both a scanning electron microscope (SEM) (VE-9800, Keyence Co. Ltd., Japan) and field emission scanning electron microscope (FE-SEM) (Zeiss Ultra Plus, Carl Zeiss Microscopy GmbH, Germany). For both cases, the fiber surface was coated with Au and osmium coating respectively for 60 seconds using coating devices (SC-701; Sanyu Electron Co. Ltd., Japan) and (HPC-1SW, Japan) separately.

3.3.2 Elemental composition measurement

The elemental composition as well as the chemical and electronic state of the atoms within the fiber was measured by X-ray photoelectron spectroscopy (XPS) (JEOL JPS-9010 (Nippon Electronics Co. Ltd., Japan). Energy dispersive spectroscopy (EDS) was also performed to assess the elemental mapping.

3.3.3 ATR-FTIR spectroscopy

FTIR spectra for chemical characterization of the fibers were obtained by using a Fourier transform infrared spectrometer (IR Affinity-1, Shimadzu, Japan) integrated with an attenuated total reflectance (ATR) accessory. The experiment was run in transmission mode over the spectral range of 4000–400 cm^{-1} with at least three scans averaged, for each spectrum.

3.3.4 Measurement of β-galactosidase enzyme activity in continuous bio-reactor

Continuous reaction experiments for lactose hydrolysis were performed using a simple bioreactor; jacketed glass column (MBRS-051J; 500 ml volume; EYELA, Japan) (**Fig. 3.2**) with the immobilized enzyme. 400 ml substrate solution (lactose) was impregnated and subjected to continuous reaction at 37.5 ° C. The substrate solution was supplied to the reaction vessel at 45 ml/hrs. by a microtube pump (inner diameter: 1.15 mm, outer diameter: 3.25 mm), and the same amount of reaction solution was discharged.

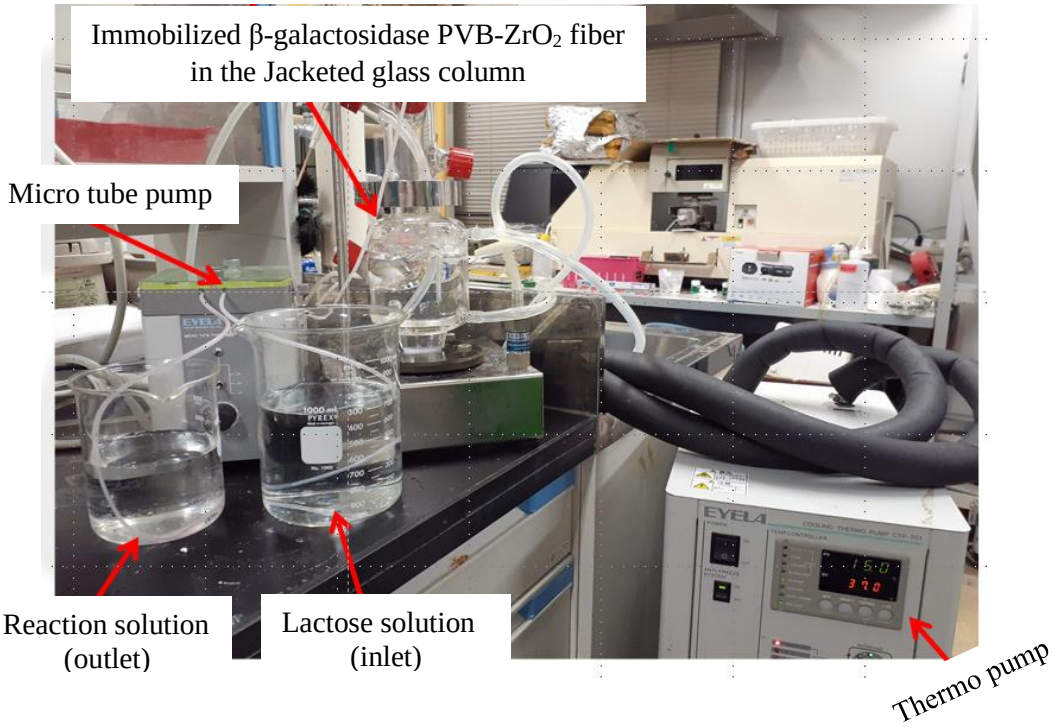

Fig. 3.2 Photograph of the lactose hydrolysis process performed by immobilized PVB-ZrO_2 fiber in continuous bio-reactor.

3.3.5 Batch adsorption and decomposition of dyes by PVB-TiO_2 hybrid fiber

The dark adsorption kinetics and decomposition of the dyes were tested by using a UV-vis spectrometer to monitor dye concentration at regular intervals. Once the adsorption had reached equilibrium, samples immersed in the solution were exposed to visible light (**Fig. 3.3).** Then the dispersion solution was constantly stirred with a stirring bar while being irradiated under a 100 W halogen lamp (Mega Light100-ROHS, SCHOTT) [3]. The absorbances for MB, MO, and Rh-B were measured at 664 nm, 463 nm, and 554 nm, respectively, for both adsorption and decomposition. Equations (3.7), (3.8), and (3.9) respectively, were used to determine adsorption efficiency (%), adsorption capacity, and normalized absorbance at the light.

$$\text{Adsorption efficiency (\%)} = (C_0 - C_t)/C_0 \times 100 \text{ --------- (3.7)}$$

$$Q_t \text{ (mg/g)} = (C_0 - C_t)/m \times V \text{ ---------- (3.8)}$$

$$A/A_1 = \exp(-Kt) \text{ ---------- (3.9)}$$

where, C_0 and C_t (mg/L) are the dye concentrations at times zero and arbitrary t, respectively. V (L) is the volume of the dye solution, m (g) is the mass of the fiber, Q_t is the fiber adsorption capacity in mg/g, K represents the rate constant, and t is the total time employed for the test.

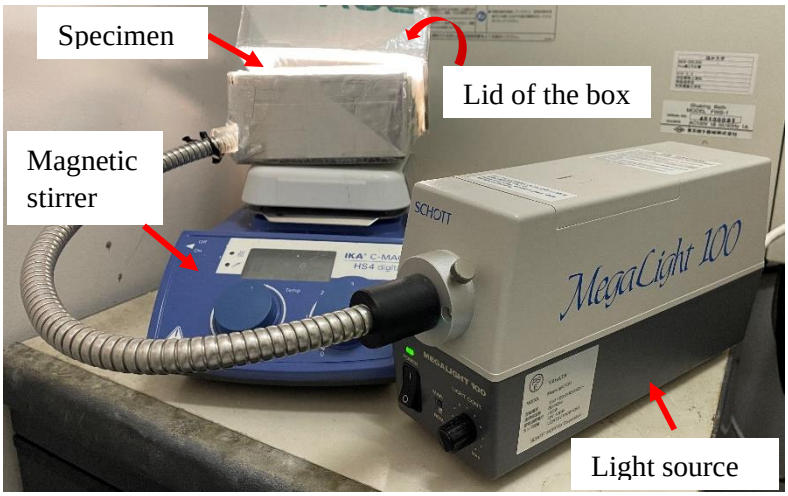

Fig. 3.3 Photograph of the visible-light irradiation experiment carried out in a dark place. Two samples could be irradiated at the same time.

REFERENCES

1 R. E. Huber, G. Kurz and K. Wallenfels, *Biochemistry*, 1976, **15**, 1994–2001.
2 A. H. Bhuiyan, T. Nagakawa, and K. Nakane, *Journal of Applied Polymer Science*, 2020, **138** (14), 50164.
3 A. H. Bhuiyan, M. Zakaria and K. Nakane, *RSC Advances*, 2022, **12**, 5300–5311.
4 A. H. Bhuiyan, T. Nagakawa, M. Zakaria and K. Nakane, *Journal of Materials Science*, 2021, **56**, 8668–8678.
5 M. Koller, D. Puppi and F. Braunegg, *International Journal of Pharmaceutical Sciences Research*, 2016, **3**, IJPSR-112.

CHAPTER FOUR

4. POLYVINYL BUTYRAL-ZIRCONIA HYBRID HOLLOW FIBERS PREPARED BY AIR GAP SPINNING

4.1 INTRODUCTION

Despite some demerits, polymers are still the main materials in hollow fiber preparation due to the facilities of good membrane forming capability, flexibility, and low cost [1–3]. However, limited chemical, mechanical and thermal resistance restricts the application of organic polymer materials [4,5]. As reported in literature [6,7], ceramic hollow fiber membranes have higher thermal and chemical resistance as well as a longer lifetime, but they are still expensive and brittle with poor membrane-forming ability. On the other hand, composite materials may combine basic properties of organic and inorganic materials and offer specific advantages for the preparation of artificial hollow fiber membranes with excellent separation performances, good thermal and chemical stability, and adaptability to harsh environments [8–11]. Therefore, organic-inorganic hybrid hollow fiber as a membrane has attracted more attention recently [12,13]. In the past, the most popular hollow fiber prepared from hydrophobic polymers exhibited fouling phenomena in special applications, such as bio-separation and membrane bioreactors [14,15]. To overcome these shortcomings, polymeric additives like polysulfone (PSF), polyethersulfone (PES), and polyvinylidene fluoride (PVDF), etc. were frequently used, which ascended the pore structure (increased pore sizes and numbers), and also modified the morphology of hydrophobic membranes [16–18]. On the contrary, the hydrophilic leading polymers can easily facilitate water diffusion, reclaim the irreversible adsorption of biomolecules on the membrane surface and lessen membrane clogging [4,19]. Polyvinyl butyral (PVB) is an effective hydrophilic polymer with good mechanical properties, may have wide application prospects, and also endure low temperatures, light, humidity, bacteria, micro-organism, alkali, diluent acids, and so forth. Numerous reports revealed the preparations of PVB hollow fiber membranes blended with other materials by thermally-induced phase separation [20–22], non-solvent-induced phase separation, and several wet spinning methods [23,24]. Furthermore, structural characterization and catalytic properties of inorganic ZrO_2/TiO_2 hollow fiber were studied via a template method coupled with the hydrothermal process. Another report revealed the preparation of zirconia hollow fiber by the sol-gel process and applied successfully on microextraction [25]. Up to now, our research group has focused on the interaction between transition metal alkoxides and organic materials to prepare organic-inorganic hybrid gel fibers by air gap spinning. In this manner, Nakane et al. confirmed the formation of cellulose acetate (CA)-zirconium (Zr) alkoxide and CA-tantalum (Ta) alkoxide gel fiber where CA and metal (Zr, Ta) alkoxides were coordinately bonded [26]. Like CA, PVB is a random hydrophilic copolymer having acetyl and hydroxyl groups which can make a similar coordinate bond with transition metal as a ligand [27]. Considering the above property of PVB, the formation of PVB-zirconia hybrid films is prepared with excellent thermal and mechanical properties followed by the sol-gel method [27]. However, no work has been reported on the preparation of PVB hollow fiber with transition metal zirconium alkoxide by air gap spinning.

In this present chapter, PVB-zirconia (ZrO_2) hybrid hollow fibers were successfully prepared by the air gap spinning method. The effects of spinning solution, coagulation liquid, and air gap

distance on the fiber properties such as morphologies, fiber diameters, amount of the Zr content, and porous structure were examined broadly.

4.2 EXPERIMENTAL

4.2.1 Materials

Three PVBs (Mowital® PVB B60T, PVB B60H, and PVB B60HH) have an almost similar molecular weight of 50-60 kDa and different butyral content (degree of acetalization) like 69-75%, 75-81%, and 82-88% respectively were purchased from Kuraray Co. Ltd. (Japan). All the PVBs had almost the same solid wt.% of 97.5. Zirconium (IV) butoxide 85-90% involved as a coagulation liquid was purchased from Fujifilm Wako Pure Chemical Industries, Ltd., (Japan). Other analytical grade solvents like methanol, ethanol, and acetone were purchased from Nacalai Tesque Inc., Japan. All chemicals were used without purification. Moreover, self-prepared distilled water was used for all experiments.

4.2.2 Preparation of spinning solution and coagulation liquid

PVB was added to dehydrated ethanol and dissolved while stirring at room temperature for 24 hrs to prepare a spinning solution. At that time, the concentration of the spinning solution was 15 wt.% (Ethanol: 8.5 g, PVB: 1.5 g), 20 wt.% (Ethanol: 8.0 g, PVB: 2.0 g), and 25 wt.% (Ethanol: 7.5 g, PVB: 2.5 g). In another beaker, zirconium (IV) butoxide was added to dehydrated acetone at room temperature and stirred uniformly to prepare a coagulation liquid. At that time, the concentration of the coagulation liquid was 10 wt.% (Acetone: 9.0 g, Zr: 1.0 g), 15 wt.% (Acetone: 8.5 g, Zr: 1.5 g), and 20 wt.% (Acetone: 8.0 g, Zr: 2.0 g). Dehydrated ethanol and dehydrated acetone were prepared by adding molecular sieves 3A to a bottle containing each organic solvent (approximately 50 g/L) and let stand for more than 24 hrs.

4.2.3 Fabrication of PVB-ZrO_2 hybrid hollow fiber

The PVB-ZrO_2 hybrid hollow fibers were prepared via an air gap spinning process at room temperature (**Fig. 4.1**). The PVB spinning solution passed through a spinneret (volume 2 mL, nozzle outer diameter 3 mm, and inner diameter 2 mm) into a coagulation bath under the pressure of N_2 gas measured 0~2 $kg.cm^{-2}$ when air gap was adjusted to 2 to 4 cm. Outer Zr alkoxide coagulation liquid was always stirred with a speed of 100 to 410 rpm. The detailed spinning conditions are summarized in **Table 4.1**. The fabricated PVB-Zr alkoxide hollow fiber formed in the coagulation liquid was taken out after a retention period of 20 min and cut both ends with tweezers, washed with methanol, and stored in water for at least 24 hrs to remove any residual solvent. In this period PVB-Zr alkoxide is hydrolyzed and transformed to PVB-ZrO_2 hybrid fiber. Later, the prepared fiber was dried by a freeze dryer for about 24 hrs at -50 ˚C and under 20 Pa.

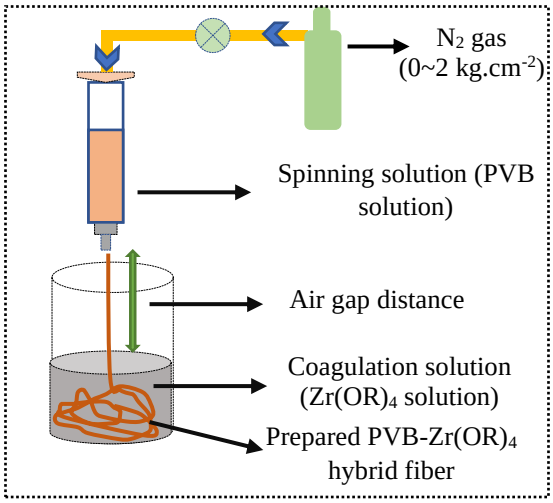

Fig. 4.1 Schematic diagram of air gap spinning for PVB-$Zr(OR)_4$ hybrid hollow fiber.

Table 4.1 Preparation conditions of PVB-$Zr(OR)_4$ hybrid hollow fibers.

Fiber No.	Spinning solution wt.% (PVB B60H: Ethanol)	Air gap distance (cm)	N_2 gas pressure (kg.cm^{-2})	Coagulation solution wt.% ($Zr(OR)_4$: Acetone)
F-1	20:80	2	2	10:90
F-2				15:85
F-3				20:80
F-4	15:85	2		10:90
F-5	20:80			
F-6	25:75			
F-7	20:80	2		
F-8		3		
F-9		4		

4.2.4 Characterizations of hollow fibers

The morphologies of PVB-ZrO_2 hybrid hollow fibers were measured by a Keyence SEM (VE-9800, Keyence Co. Ltd., Osaka, Japan) with an applied voltage of 5 kV. Cross-sectional images were examined to investigate the skin layer (internal and external) and pore morphologies. By an ion coater (SC-701; Sanyu Electron Co. Ltd., Tokyo, Japan), all samples were coated with Au/Pd sputtering under a vacuum. In addition, adobe photoshop CS_3 software was used to measure the average fiber outer diameter (D), and finally, standard deviations (σ) were obtained and visualized in histogram curves. 400-1400 cm^{-1} IR spectra of hollow fibers were measured by an IR spectrometer (IR-affinity-1, Shimadzu Corporation, Kyoto, Japan) equipped with a single reflection ATR accessory (MIRACLE 10; Shimadzu Corporation, Kyoto, Japan) holding diamond/ZnSe crystal. To investigate the coordination bonding between the Zr and acetyl group of PVB, the IR spectra of prepared fiber were compared with pure PVB film and pure ZrO_2

particle. Prior, a pure PVB film of 2 g PVB powder was prepared by the hot press at 180 °C. Furthermore, 10 wt.% hydrolyzed products of pure Zr (IV) butoxide (ZrO_2) was poured into a petri dish for drying at 40 ˚C and finely crushed by a mortar. The total Zr content of the hybrid fiber was examined by a thermogravimetric analyzer (DTG-60, Shimadzu Corporation, Japan) at a heating rate of 10 °C/min while the fiber weight was adjusted to 6-10 mg (Zr alkoxide varies by 10-20 wt.% in coagulation solution) for 30-600 °C. The presence of Zr content in the internal and external surface of the fabricated hybrid fiber was measured by JPS-9010 series X-ray photoelectron spectroscopy manufactured by JEOL Ltd., Japan. The etching rate was 65 nm per minute performed by Ar ions where Mg-kα ray was used as a source.

4.3 RESULTS AND DISCUSSION

4.3.1 Physio-chemical appearances of PVB-ZrO_2 hybrid hollow fiber

Fig. 4.2 (a) shows the overview of freeze-dried hollow fiber prepared by air gap spinning. Hollow fibers formed by combined PVB and zirconium alkoxide initially looked swollen in methanol and water bath (**Fig. 4.3**) but they significantly squeezed and shaped after drying. In **Fig. 4.2 (b)**, an illustration of organic-inorganic chemistry between the ligand oxygen and zirconium materialized behind the fiber preparation [28].

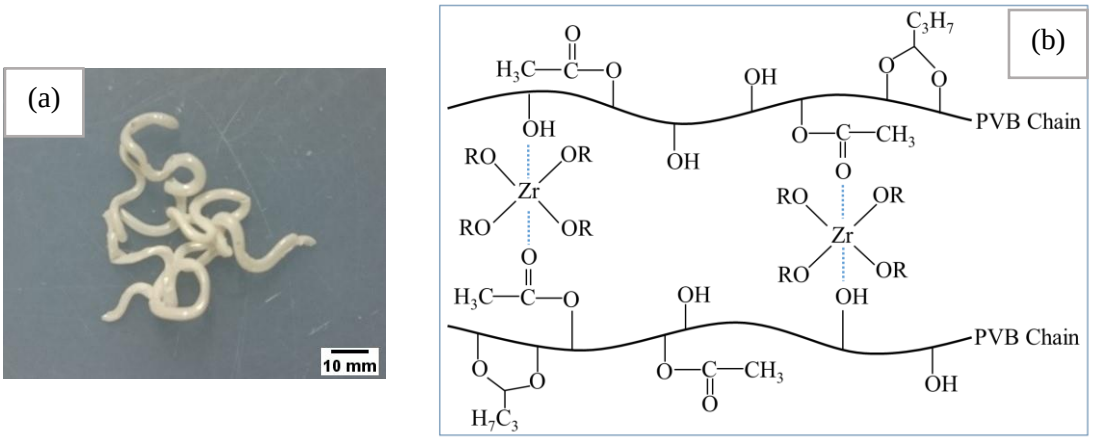

Fig. 4.2 Photograph of (a) freeze dried PVB-ZrO_2 hybrid hollow fiber, and (b) proposed coordinate bonding between PVB and $Zr(OR)_4$ while fiber is prepared.

Fig. 4.3 Photograph of PVB-ZrO_2 hybrid hollow fiber before drying (impregnated in methanol).

4.3.2 FTIR analysis of PVB-ZrO_2 hybrid hollow fiber

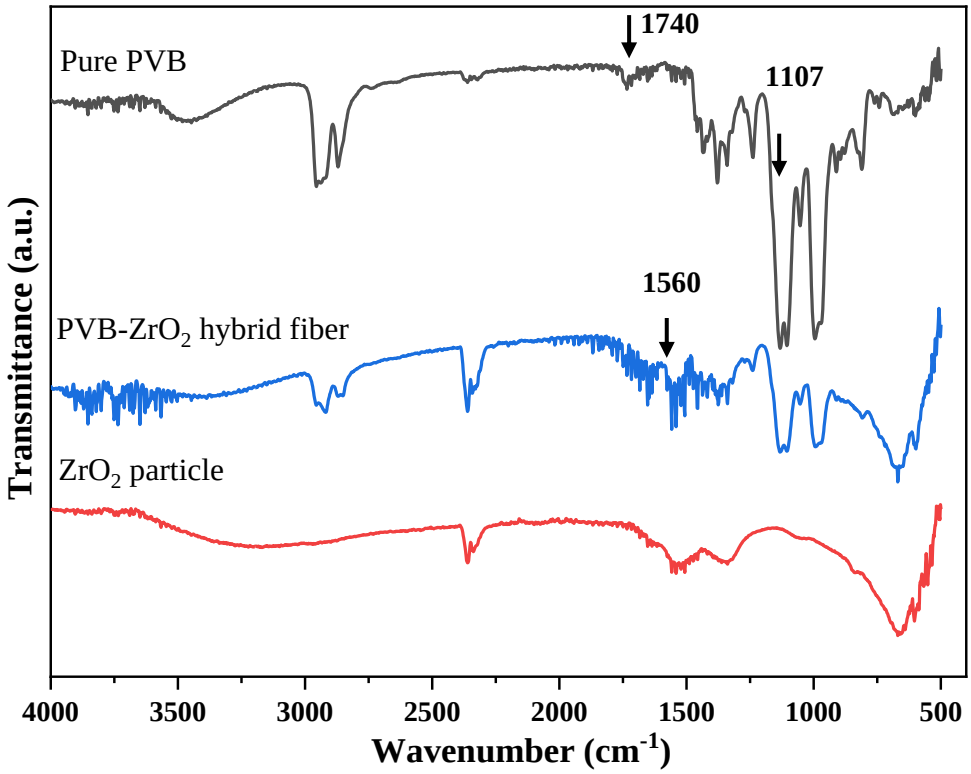

Fig. 4.4 ATR-FTIR spectra of pure PVB film (PVB/F), ZrO_2 particle (Zr/P) and PVB-ZrO_2 hybrid hollow fiber (PVB-Zr/F).

Fig. 4.4 shows the comparative spectrum study among PVB-ZrO_2 hybrid hollow fiber (PVB-Zr/F), pure PVB film (PVB/F), and ZrO_2 particle (Zr/P). As seen from the spectra, there is a peak of CO single bond stretching mode at 995 cm^{-1} for PVB/F and a little broader peak for PVB-Zr/F at the same position. Stretching bands of C−H between 2870 and 3000 cm^{-1} appeared while the bending bands between 1400 and 1280 cm^{-1} correspond to these alkynes for PVB existing samples [29]. However, there was no similar evidence for Zr/P. In addition, a probable ester band at about 1230 cm^{-1} is observed [29]. A weak band at 1740 cm^{-1} is assigned to the C=O of the acetyl group for both PVB-prone samples. Furthermore, some bands at 550-650 cm^{-1} are assigned for aliphatic esters [30] for zirconium-prone samples which are probably a little contaminated by oxygen. In PVB-Zr/F and PVB/F, three absorption peaks at 1130 cm^{-1},1107 cm^{-1}, and 1053 cm^{-1} are seen and attributed to the asymmetric and symmetric stretching vibration of C−O−C [31]. However, the peak at 1130 cm^{-1} and 1107 cm^{-1} for the PVB-Zr/F sample was a little wider and broader which could be the alteration of C−O−C stretching to Zr−O−C. This is thought to be probably due to the coordinate bonding between PVB and $Zr(OR)_4$. Moreover, a band of weak intensity appeared at 1560 cm^{-1} for PVB-ZrO_2 fiber which was due to the interaction of Zr−O−C.

4.3.3 Effect of coagulation liquid concentration

Fig. 4.5 shows the SEM micrographs and fiber diameter histograms of PVB-ZrO_2 hybrid hollow fiber when the concentration of the coagulation solution is changed. All fibers exhibit thick external surfaces while the inner structure persisted hollow. As can be seen from **Fig. 4.5**, fibers F-1, F-2, and F-3 possessed the outer diameter (*D*) of 1016.1 μm, 991.9 μm, and 972.9 μm respectively which suggested that the concentration of the coagulation liquid has a significant effect on the fiber outer diameter. But there was a typical asymmetry in the external skin of the fiber and postulated fragile structure when the concentration of coagulation liquid increased. In addition, the total Zr content of F-1, F-2, and F-3 fibers was measured by TG analysis at 600 ˚C

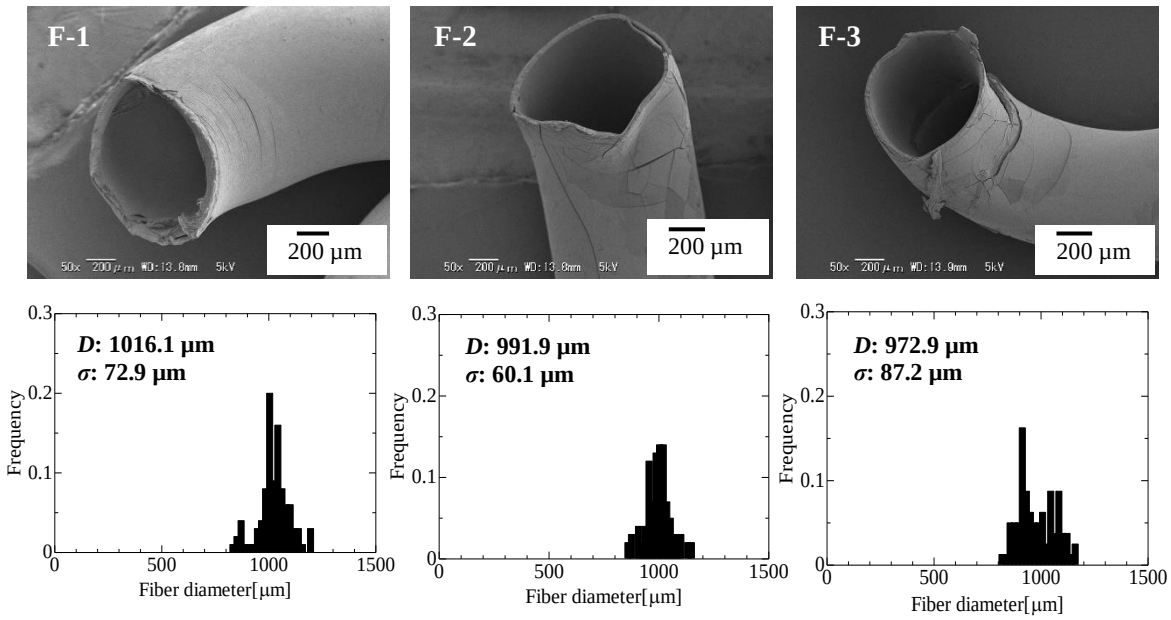

Fig. 4.5 SEM images and fiber diameter histograms of PVB-ZrO_2 hybrid hollow fibers spun with different $Zr(OR)_4$ concentration (F-1: 10 wt.%, F-2: 15 wt.%, F-3: 20 wt.%) with PVB 20 wt.% and 2 cm air gap.

showing the value of 14.47%, 16.55%, and 19.02% respectively which is thought to be caused due to incremental Zr concentration ascribed. From this, it is concluded that changing $Zr(OR)_4$ concentration (10 wt.%-20 wt.%) does lead to a little increment of Zr content in the formed hybrid hollow fiber.

4.3.4 Effect of spinning dope concentration

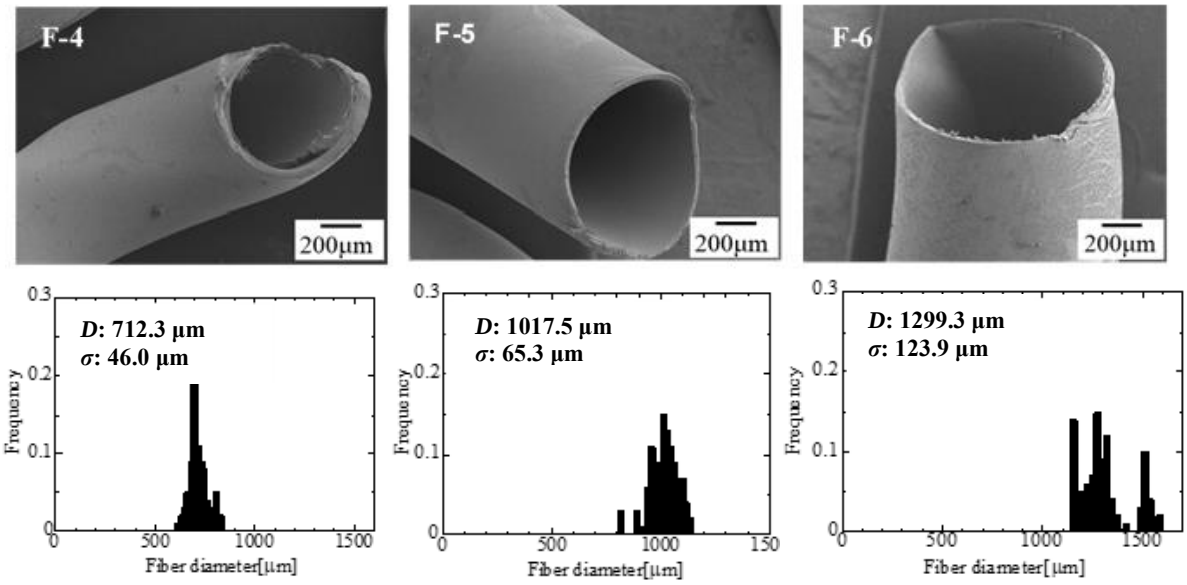

Fig. 4.6 SEM images and fiber diameter histograms of PVB-ZrO_2 hybrid hollow fibers spun with different PVB concentration (F-4: 15 wt.%, F-5: 20 wt.%, F-6: 25 wt.%) with $Zr(OR)_4$ 10 wt.% and 2 cm air gap.

The SEM image of the fiber cross-section and histograms of PVB-ZrO_2 hybrid hollow fibers are shown in **Fig 4.6**. All fibers exhibited an irregular morphology with a thin skin layer and were hollow. Unlike the internal surface, all developed symmetrical external surfaces confirmed the dominance of strong coordination bonding between PVB and zirconium. However, this structure indicates that the skin layer was induced by Zr alkoxide penetrated from both the external and internal surfaces of hollow fibers. As can be seen from **Fig. 4.6**, the transformation of overall fiber morphology was not vastly dependent on PVB concentration. The thermodynamic stability of the spinning solution does not change much after the increment of PVB; the change was mainly reflected in the kinetic effect which caused a small variation in fiber surface and irregularity. However, the diameter (*D*) of the fibers was decreased with the lowering of the PVB concentration. Compared to other fibers, F-5 and F-6 have the structure of a large macrovoid which caused a very thin regular external surface. But fiber diameter irregularity also appeared greatly for F-6 which is confirmed by the standard deviation value (σ=123.9 μm). This is thought to be because the thickness of the spinning solution was changed as the viscosity of the spinning solution changed which impacts the fiber diameter and surface irregularity.

4.3.5 Effect of air gaps

Fig. 4.7 shows the SEM photographs and histogram of the PVB-ZrO_2 hybrid hollow fibers when the air gap is changed. The outer diameter (*D*) of the fiber is decreased from 1017.5 µm to 718.1 µm for F-7 and F-9 respectively as the air gap is changed from 2 to 4 cm. This is triggered due to the spinning solution gradually becomes thinner when falling from spinneret die. The thickness of the wall of the fiber (*ca.* 27.2~30.9 µm) was also compared, but no significant difference was found.

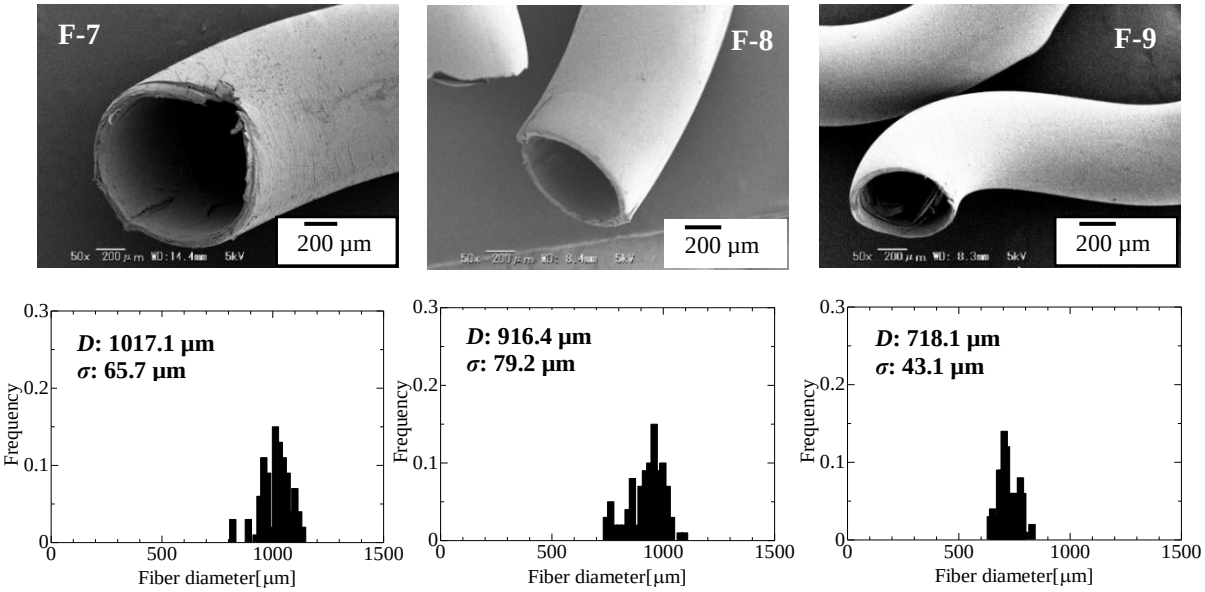

Fig. 4.7 SEM images and fiber diameter histograms of PVB-ZrO_2 hybrid hollow fibers spun with different air gap distance (F-7: 2 cm, F-8: 3 cm, F-9: 4 cm) with PVB 20 wt.% and $Zr(OR)_4$ 10 wt.%.

4.3.6 Effect of degree of acetalization on hollow fiber formation

Fig. 4.8 shows the micrograph of hollow hybrid fiber cross-sections when PVB was used with different degrees of acetalization in their composition. Other than PVB B60H, PVB B60T, and PVB B60HH were also employed to develop hollow fiber while spinning dope concentration, coagulation bath concentration, and air gap distance remained constant. Due to less acetyl group

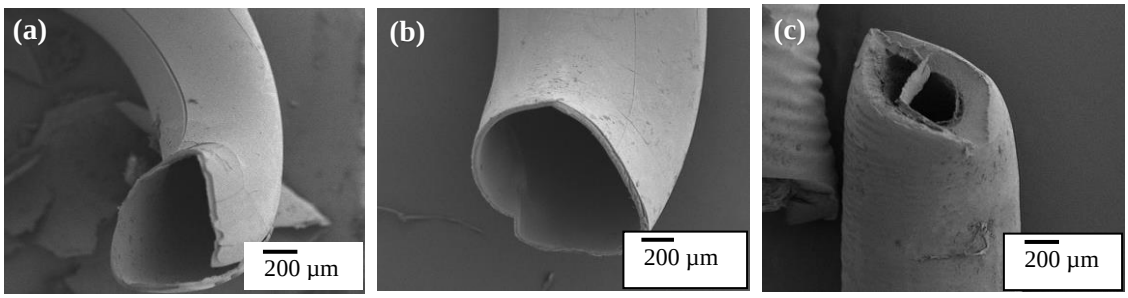

Fig. 4.8 SEM photographs of PVB-ZrO_2 hybrid hollow fibers spun with changing butyral content % (a: B60T, b: B60H, c: B60HH) with PVB 20 wt.%, $Zr(OR)_4$ 10 wt.% and 2 cm air gap.

in B60T, the developed fiber was more fragile in structure with an insufficient shape which was possibly caused by less interaction between PVB and Zr alkoxide. However, B60H and B60HH produced the thicker and more robust hollow structures with larger outer diameters. This might be the result of enhanced acetyl degree which caused the lower viscosity spinning solution (maximum viscosity 280 mPa·s) to extrude from the die. Furthermore, the B60H-engaged fiber cross-section shows a more regular and smoother surface compared to B60HH.

4.3.7 TG analysis

Fig. 4.9 shows (a) TGA curves and (b) residual weight as a function of $Zr(OBu)_4$ coagulation bath concentration used in this experiment. The residual weight contents correspond to the weight at 600 °C in the TGA curves. All samples are thermally decomposed in three stages, as stated by Hanna *et al.* [32]. The initial degradation (at about 150 °C) was attributed to bound water evaporation. The second and third decompositions took place at around 270 °C and 410 °C respectively. Considering that the amount of decomposition at the second stage decreased with increasing $Zr(OBu)_4$ bath concentrations, which must correspond with the degradation of PVB. A similar phenomenon was described for the other CA-metal oxide systems [33]. With increasing $Zr(OBu)_4$ bath concentration, the residual weight was considered to increase. However, a significant decrease in the inner diameter of the core hollow structure is observed at higher concentrations. Thus, hollow-structured fiber with a weight percentage of 10 wt.% to 20 wt.% is considered. These results indicated that the number of interactions between the PVB molecular chain and $Zr(OBu)_4$ molecules influences the total Zr content in the fiber.

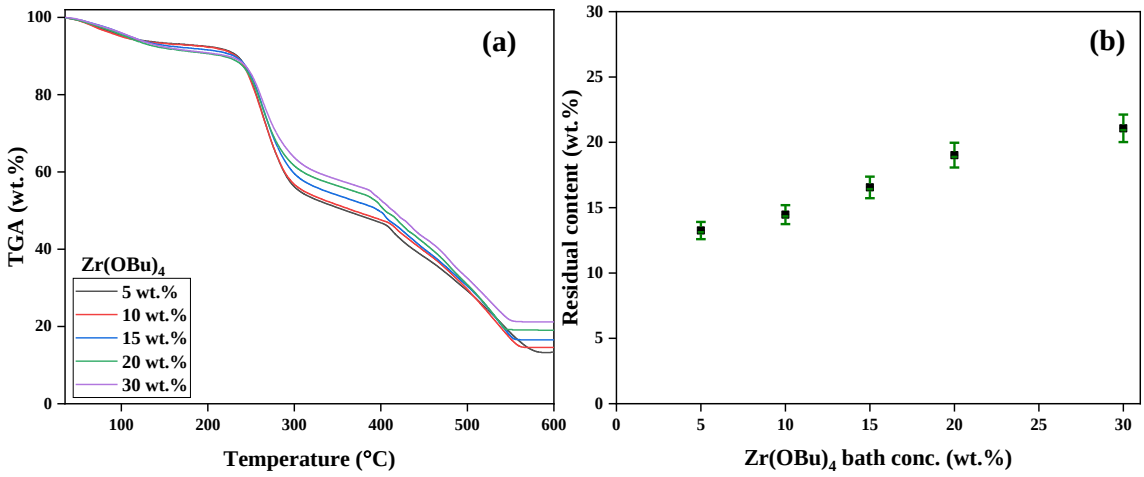

Fig. 4.9 (a) TGA profiles, and (b) residual weights of the PVB-ZrO_2 hybrid hollow fibers at 600 °C as a function of $Zr(OBu)_4$ bath concentration.

4.3.8 EDS measurement

To further understand the distribution of Zr within the fiber, we then carried out EDS measurements of the fiber. **Fig. 4.10** shows C, O, and Zr mapping pictures for fiber samples of 10 wt.% $Zr(OBu)_4$ bath concentration. Throughout the wall of the fiber, we assume both C and O distributions were nearly consistent. However, Zr mapping demonstrated the uniform distribution of Zr within the fiber. High-intensity Zr distribution spectrum also suggested the homogeneous diffusion of Zr from the surface to the center.

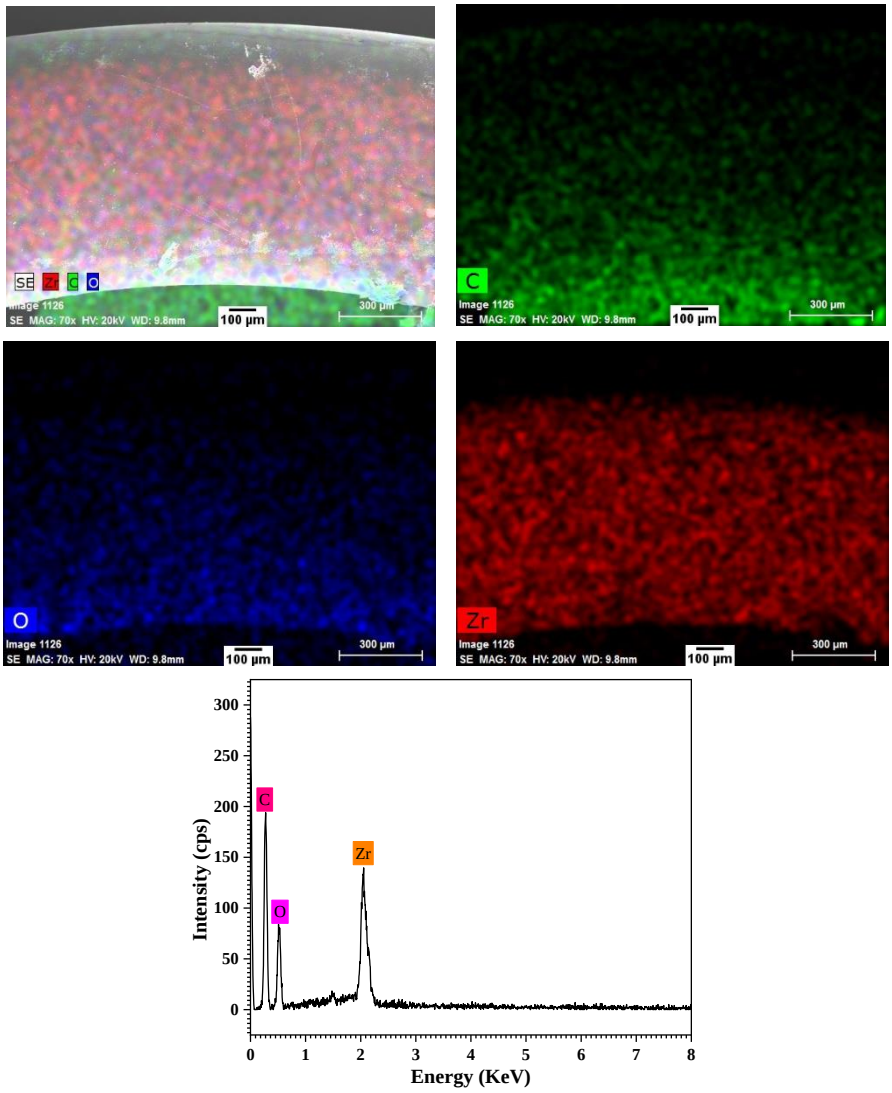

Fig. 4.10 EDX elemental mapping (top), and Zr distribution spectrum (bottom) at the center point of the PVB-ZrO_2 hybrid hollow fiber prepared with 10 wt.% $Zr(OBu)_4$ bath concentration.

4.3.9 Surface content measurement of hybrid hollow fiber

SEM photographs of both external and internal surfaces are shown in **Fig. 4.11**. High viscosity along with less reaction time led to form a dense external surface with high zirconium content whereas internal surface morphology shows irregularities due to reduced solidification rate. Compared to the external surface, the Zr precipitation rate at the internal side lessens considerably when the spinning solution viscosity is increasing. **Fig. 4.12** (a, b) shows the O 1s and Zr 3d XPS measurement results of the internal and external surfaces of PVB-ZrO_2 hybrid hollow fiber. Pure ZrO_2 particles (hydrolyzed product of $Zr(OBu)_4$) and pure PVB were taken as a comparison sample. Both spectra were fitted by Gaussian distribution. Other than pure PVB, all O 1s peaks can be deconvoluted at ~532.5 and ~530.2 eV denoted as O_I and O_{II}, which correspond to the defect oxygen and lattice oxygen respectively [34]. It is known that the peak centered at ~530.0 eV represents the oxygen ions (O^{2-}) combined with metal cations in ZrO_2 particles. Similarly, peaks located at ~532.2 eV are related to the O^{2-} ions located in oxygen-vacancy regions in the structure and the bonded oxygen such as O_2, OH^-, or H_2O [35] which happened in the case of both the external and internal surfaces of PVB-ZrO_2 hybrid fiber. Moreover, the peak at 535.5 eV for pure PVB was attributable to −COO [36]. To analyze the change of Zr 3d binding energy, Zr 3d spectra with spin-orbit doublets ($d_{5/2}$ and $d_{3/2}$) indicate the formation of ZrO_x structures. It can be seen from **Fig. 4.12** (b) that signals corresponding to ZrO_2 (Zr^{4+}) and Zr(OH)x (Zr^{3+}) are observed in the Zr $3d_{5/2}$ and Zr $3d_{3/2}$ peaks at 182.4 and 184.9 eV for the pure ZrO_2 particles [34]. But both signals tended to shift towards higher binding energy, up to ~182.6 and 185.1 eV respectively for PVB-ZrO_2 hybrid fiber. Since the electronegativity of O is stronger than that of Zr, electrons around Zr would easily transfer towards O atoms, which causes the decrease of Zr electron cloud density and results in the increasing of Zr $3d_{5/2}$ binding energy. In brief, Zr-O-Zr bond is transformed into O-Zr-O structure.

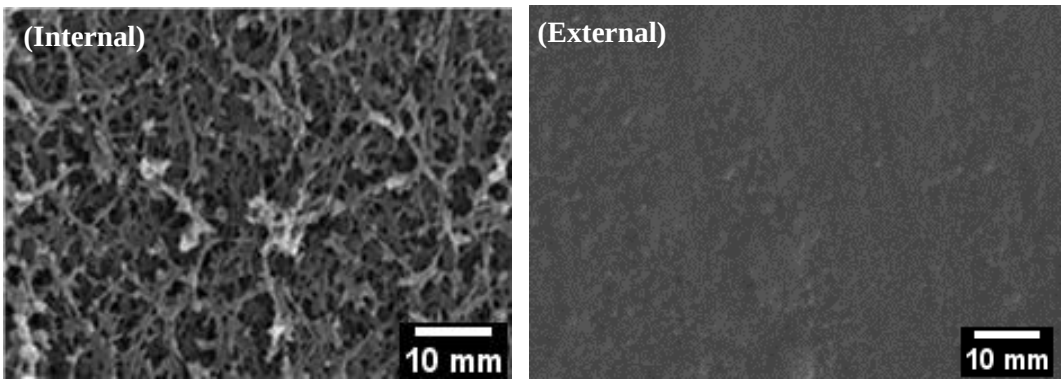

Fig. 4.11 SEM photographs of internal and external surface of F-5.

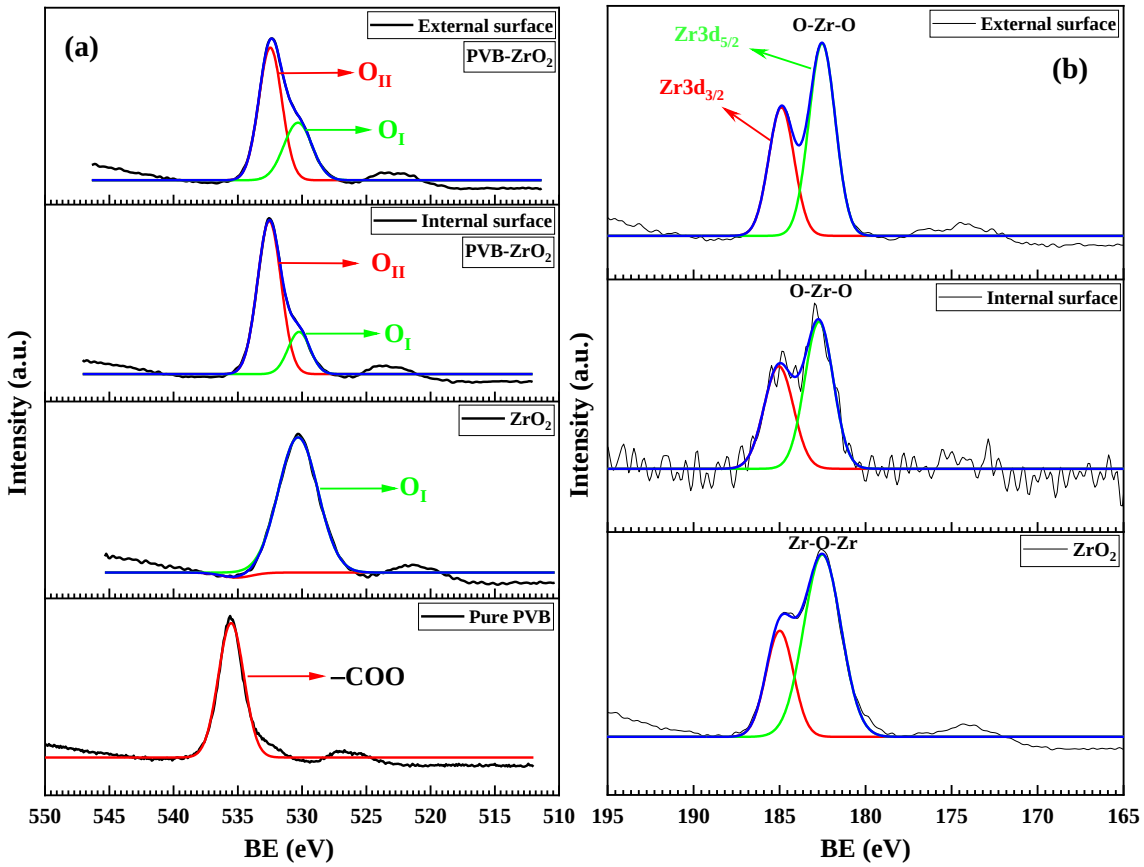

Fig. 4.12 (a) O 1s spectra of F-5, ZrO_2 particle and pure PVB, and (b) Zr 3d XP spectra of the external and internal surface of F-5 and ZrO_2 particle.

4.4 CONCLUSION

In this work, PVB-ZrO_2 hybrid hollow fiber was developed via a simple air gap (dry-jet wet) spinning technique. The results indicate that the developed hybrid fiber exhibited a typical asymmetrical structure containing a thick layer outside while the inside was hollow. The diameter of fiber increased at a particular point with increased PVB content. However, along the fiber axis, the maximum variation of fiber diameter was produced when more PVB was added. With the increment of PVB acetyl degree, the surface robustness improved while a fragile structure was formed for reduced acetyl content. Data illustrates that Zr alkoxide vastly affected the fiber's external surface since most of the coordination bonding between PVB and Zr alkoxide started from that site. XPS measurements confirmed the authenticity of maximum electron excitement at both internal and external surfaces.

REFERENCES

1 J. Xu and Z.-L. Xu, *Journal of Membrane Science*, 2002, **208**, 203–212.
2 Z.-L. Xu and F. A. Qusay, *Journal of Membrane Science*, 2004, **233**, 101–111.
3 T.-S. Chung, Z.-L. Xu and W. Lin, *Journal of Applied Polymer Science*, 1999, **72**, 379–395.
4 A. V. R. Reddy, D. J. Mohan, A. Bhattacharya, V. J. Shah and P. K. Ghosh, *Journal of Membrane Science*, 2003, **214**, 211–221.
5 Z.-L. Xu, T.-S. Chung and Y. Huang, *Journal of Applied Polymer Science*, 1999, **74**, 2220–2233.
6 G. Clarizia, C. Algieri and E. Drioli, *Polymer*, 2004, **45**, 5671–5681.
7 Y. Yang and P. Wang, *Polymer*, 2006, **47**, 2683–2688.
8 C. Guizard, A. Bac, M. Barboiu and N. Hovnanian, *Separation and Purification Technology*, 2001, **25**, 167–180.
9 Z. Lu, G. Liu and S. Duncan, *Journal of Membrane Science*, 2003, **221**, 113–122.
10 P.-C. Chiang, W.-T. Whang, M.-H. Tsai and S.-C. Wu, *Thin Solid Films*, 2004, **447**, 359–364.
11 A. Taniguchi and M. Cakmak, *Polymer*, 2004, **45**, 6647–6654.
12 T.-S. Chung and Z.-L. Xu, *Journal of Membrane Science*, 1998, **147**, 35–47.
13 Z.-L. Xu and F. A. Qusay, *Journal of Applied Polymer Science*, 2004, **91**, 3398–3407.
14 A. Amanda and S. K. Mallapragada, *Biotechnology Progress*, 2001, **17**, 917–923.
15 H. Yang and M. Ulbricht, *Macromolecular Materials and Engineering*, 2008, **293**, 419–427.
16 Z. Yuan and X. Dan-Li, *Desalination*, 2008, **223**, 438–447.
17 B. Chakrabarty, A. K. Ghoshal and M. K. Purkait, *Journal of Membrane Science*, 2008, **315**, 36–47.
18 M.-J. Han and S.-T. Nam, *Journal of Membrane Science*, 2002, **202**, 55–61.
19 M. Ulbricht and H. Yang, *Chemistry of Materials*, 2005, **17**, 2622–2631.
20 X. Fu, H. Matsuyama, M. Teramoto and H. Nagai, *Separation and Purification Technology*, 2005, **45**, 200–207.
21 X. Fu, H. Matsuyama, M. Teramoto and H. Nagai, *Separation and Purification Technology*, 2006, **52**, 363–371.
22 Y.-R. Qiu and H. Matsuyama, *Desalination*, 2010, **257**, 117–123.
23 J. Wang, W.-Z. Lang, H.-P. Xu, X. Zhang and Y.-J. Guo, *Chemical Engineering Journal*, 2015, **260**, 90–98.
24 P. Zhang, Y. Wang, Z. Xu and H. Yang, *Desalination*, 2011, **278**, 186–193.
25 T. Wang, Q. Yu, and J. Kong, *International Journal of Applied Ceramic Technology*, 2018, **15**, 472–478.
26 K. Nakane, N. Ogata and Y. Kurokawa, *Journal of Applied Polymer Science.*, 2006, **100**, 4320–4324.
27 K. Nakane, K. Mizutani, R. Zhang, K. Sugimoto and N. Ogata, *World Journal of Engineering*, 2012, **9**, 233–238.
28 Y. Ikeda, Y. Kurokawa, K. Nakane and N. Ogata, *Cellulose*, 2002, **9**, 369–379.
29 E. Corroyer, M.-C. Brochier-Salon, D. Chaussy, S. Wery and M. N. Belgacem, *International Journal of Polymer Analysis and Characterization*, 2013, **18**, 346–357.
30 C. T. Lynch, K. S. Mazdiyasni, J. S. Smith and W. J. Crawford, *Analytical Chemistry*, 1964, **36**, 2332–2337.
31 P. Peer, M. Polaskova and P. Suly, *Chinese Journal of Polymer Science*, 2018, **36**, 742–748.

32 A. A. Hanna, A. H. Basta, H. El-Saied and I. F. Abadir, *Polymer Degradation and Stability*, 1999, **63**, 293–296.
33 T. Uesaka, N. Ogata, K. Nakane, K. Shimizu and T. Ogihara, *Journal of Applied Polymer Science*, 2002, **83**, 1750–1758.
34 J. Gu, Z. Xin, M. Tao, Y. Lv, W. Gao and Q. Si, *Applied Catalysis A: General*, 2019, **575**, 230–237.
35 G. X. Liu, A. Liu, Y. Meng, F. K. Shan, B. C. Shin, W. J. Lee and C. R. Cho, *Journal of Nanoscience and Nanotechnology*, 2015, **15**, 2185–2191.
36 Y. I. Jinxin, H. U. O. Zhipeng, T. A. N. Xiaoli, C. Changlun, A. M. Asiri, K. A. Alamry and L. I. Jiaxing, *Plasma Science and Technology*, 2019, **21**, 095502.

This article was published in the *Journal of Applied Polymer Science*, 2020; 138(14), 50164.

CHAPTER FIVE

5. UTILIZATION OF POLYVINYL BUTYRAL-ZIRCONIUM ALKOXIDE HYBRID HOLLOW FIBER AS AN ENZYME IMMOBILIZATION CARRIER

5.1 INTRODUCTION

Recent years have witnessed the modification of organic and inorganic polymers for improving their physical and mechanical properties since they possessed distinguish limitations [1], and also utilize them as enzyme support [2]. These modified hybrid materials have been showing the potential to become an enzyme carrier with superior properties to those of many organic materials and also inorganics. Many reports revealed the processing of hybrid gel, fiber, film, and membrane by sol-gel method and employed these products as highly efficient and stable enzyme support. These include cellulose acetate (CA)-metal (Ti, Zr) alkoxide [3], CA-polysulfone polymethylmethacrylate [2], chitosan-polyvinyl alcohol [4], polypropylene-glutaraldehyde [5], chitosan-Fe_3O_4 [6], calcium (Ca)-alginate [7].

Polyvinyl butyral (PVB) has gained the attention of researchers due to its hydrophilicity, endurance in low temperatures, alkali, diluent acid, and so forth [8]. That's why PVB and ZrO_2 together have already been used to fabricate hybrid gel fiber where the acetyl group of PVB and Zr bonded together is considered [9]. Moreover, Nakane et al. reported the efficacy of successful enzyme-immobilized CA-ZrO_2 hybrid fiber where the fiber showed greater stability on several electrolyte buffer solutions and organic solvents [10,11]. In both cases, the designated enzyme was entrap-immobilized within the coordinate bonded CA-zirconium network. To the author's knowledge, there is little information available in the literature about the use of PVB as an enzyme immobilization support. However, individually hydrous ZrO_2 has been manifested to be suitable as immobilization matrices [12]. Though CA and PVB have almost similar functional groups in their structure, PVB-zirconium alkoxide hybrid hollow fiber could be an alternative efficient support matrix for enzyme immobilization. Yet, there is only one report on organic-inorganic hybrid hollow fiber derived from PVB and zirconium (IV) butoxide through a simple air gap spinning method [13].

Many techniques have been used previously for enzyme immobilization, including entrapment [14], cross-linking [15,16], adsorption [17], or a combination of these methods [18]. Among them, adsorption and entrapment are often used in industrial applications due to their low process costs and suitability in mild conditions [19]. Ca-alginate and *k*-carrageenan gels are broadly used as entrapping matrices for enzyme immobilization [20], but their performance is negotiated by their low durability, their possibility of compaction under high pressure in a reaction column, and their low stability in phosphate buffer solutions and solutions with high ionic concentrations [10].

β-galactosidase and lipase are crucial in enzyme families due to their outstanding catalytic performances in lactose hydrolysis and esterification reaction respectively [21,22]. The use of these enzymes in their free or soluble forms evidences some difficulties related to the generation of microbial growth, instability against operational parameters, difficulty to recover, and subsequent reuse [23]. However, appropriate immobilization techniques can be employed to overcome such

problems [24], besides, once immobilized, enzymes show greater resistance to parameters like pH, temperature, and storage variations [25–29].

Hence, in this study, a simple air gap spinning method has been developed to entrap-immobilize β-galactosidase and lipase on PVB-Zr alkoxide hybrid hollow fiber. The effect of various physical denaturants and solvents on the activity of the immobilized enzyme has been investigated. The relative activity and reusability of enzyme-immobilized fiber are compared with native enzymes and other support matrices.

5.2 EXPERIMENTAL

5.2.1 Materials

PVB (Mowital® PVB B60H, M_w 50-60 kDa, degree of acetalization 75-81%) was obtained from Kuraray Co. Ltd., (Japan). Zirconium (IV) butoxide 85-90% involved as a coagulation liquid was purchased from Fujifilm Wako Pure Chemical Industries, Ltd., Japan. β-galactosidase (EC 3.2.1.23; *Aspergillus oryzae*) and lipase (EC 3.1.1.3; *Candida antarctica*) were purchased from Sigma Chemical Co., Japan, and Roche Diagnostics, Switzerland respectively. Lactose monohydrate and citronellol were from Nacalai Tesque Inc., Japan where a glucose-B test kit was supplied by Fujifilm Wako Pure Chemical Industries, Ltd., Japan. Other chemicals were of annular or equivalent quality.

5.2.2 Formation of enzyme immobilized PVB-ZrO_2 hybrid hollow fiber and its characterization by scanning electron microscopy

The PVB-ZrO_2 hybrid hollow fiber was formed by loading a 20 wt.% PVB-ethanol solution (spinning solution) containing dispersed enzymes (β-galactosidase and lipase weighted separately by 3 wt.%/g PVB) into a syringe, fitting a needle to the end of the syringe, and then using compressed N_2 gas (1 $kg.cm^{-2}$) to extrude the solution through the needle into a stirred acetone solution (coagulation solution bath) containing 10 wt.% zirconium (IV) butoxide from a height of 2 cm above the surface of the coagulation liquid (**Fig. 5.1**). After standing for 20 min at room temperature (17 ± 2 °C), the resultant fiber was removed from the solution, washed with methanol (approx. 10 ml/0.35 g fiber) 2 times to remove the residual PVB and alkoxide. Following this, the prepared PVB-Zr alkoxide hybrid fiber was washed and impregnated into distilled water for at least 2 hrs to transform the alkoxide into a hydrolyzed product (PVB-ZrO_2 hybrid fiber). Later, β-galactosidase immobilized fiber was stored overnight in citrate buffer (pH 4.6) at 5 °C whereas the lipase immobilized fiber was kept in phosphate buffer (pH 6.0). Finally, the prepared hollow fiber was dried by freeze dryer for about 24 hrs at -50 °C and under 20 Pa. The morphologies of enzyme-immobilized fiber were observed by a Keyence SEM (VE 9800, Keyence Co. Ltd., Osaka, Japan) with an applied voltage of 5 kV where all fiber samples were Au/Pd sputtering coated first.

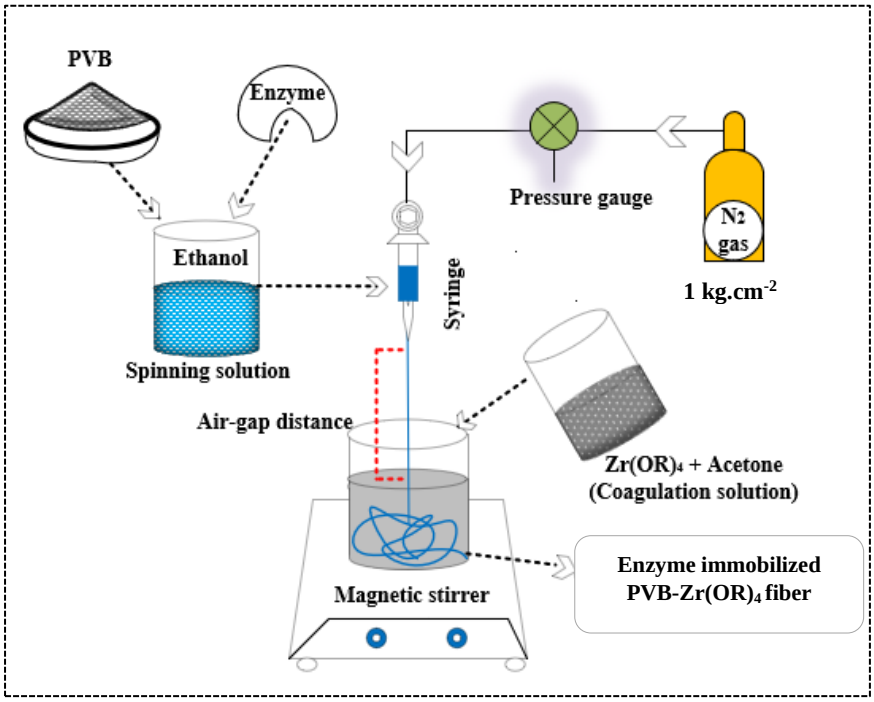

Fig. 5.1 Schematic diagram of air gap spinning for the preparation of enzyme immobilized PVB-Zr alkoxide hybrid hollow fiber.

5.2.3 Preparation of other support matrices for comparison

Ca-alginate beads (about 3 mm in diameter) immobilized with β-galactosidase were obtained by the conventional procedure. To prepare this, 1 wt.% aqueous solution of sodium alginate (Nacalai Tesque Co. Ltd.) containing β-galactosidase was added by drops to a 1 wt.% aqueous solution of calcium chloride (Nacalai Tesque Co. Ltd., Japan) [10]. Subsequently, lipase immobilized CA-ZrO_2 fiber was prepared by air gap spinning method [11].

5.2.4 Measurement of β-galactosidase activity

The free β-galactosidase (0.003 g) and the immobilized β-galactosidase (IβG) (0.1 g) were immersed into a predetermined amount of lactose solution (concentration 0.01 M-0.15 M) at 37.5 °C for 30 minutes. Bath pH (3.0-6.5) was controlled by citrate buffer solution which was used during lactose solution preparation. With varied pH values, temperature (30-80 °C) was changed to the purpose of each preparation. A 0.02 ml aliquot was taken from the reaction solution, added to 3 ml of the glucose-B kit solution, and kept at 37.5 °C for 5 minutes, and finally color developed. The absorbance was measured at 505 nm using an ASUB-1100 UV spectrophotometer. Next, a jacketed glass column (MBRS-051J; 500 ml volume) (EYELA, Japan) was packed with IβG (4 g), the temperature was adjusted to 37.5 °C, and a continuous flow reaction was commenced by simultaneously supplying and withdrawing a lactose solution [0.05 M, 400 ml, citrate buffer (pH 4.6)] through the bottom of the column at a flow rate of 40 ml/hrs. Finally, sample products were collected from the top of the column and assessed for glucose content at regular intervals.

β-galactosidase activity (A) was determined by the following equation (5.1) where the resultant glucose concentrations (X) were measured from the absorbance versus concentration curve.

A (μmol/mL/min/mg-enzyme) = X (Concentration of glucose in mg/dl) × 1/M_w of glucose × 1/ reaction time (min) × solution amount (ml) × 1/enzyme amount (g) ---------- (5.1)

5.2.5 Determination of kinetic parameters

Eadie-Hofstee plot was utilized to measure the Michaelis constant (K_m) and maximum reaction rate (V_{max}) for IβG.

5.2.6 Reusability of IβG

A 0.1 g IβG aliquot was immersed into 0.1 M lactose solution at 37.5 °C, pH 4.6 for 30 mins for assaying the activity of the enzyme. After each activity was determined, IβG was withdrawn from the solution, washed with citric acid-sodium citrate buffer, and again reused in a fresh reaction bath. The activity determined on the first run was adopted as 100% for the calculation of the remaining activity.

5.2.7 Esterification method for immobilized lipase (IL)

Esterification was conducted in screw-capped glass tubes. Unless elsewise specified, free lipase (CHIRAZYME) (0.003 g), Novozym-435, Japan [(lipase B from *Candida antarctica* immobilized on microporous polyacrylate resin; bead size 0.3-0.9 mm, activity~10,000 propyl laurate units/g)] (0.01 g), PVB-ZrO_2 hybrid fiber immobilized lipase (0.1 g) was added to a 10-mL hexane solution containing 0.2 mol/L citronellol, and 0.1 mol/L acetic acid, respectively. Linalool (0.1 mL) was also added as an internal standard. The solutions were shaken at 80 strokes/min in a thermostatic water bath at 30 °C. An aliquot was periodically withdrawn from the reaction solution and analyzed by gas chromatograph Shimadzu GC-12A, Japan (flame ionization detector) packed polyethylene glycol (PEG) 20 M stainless column (1.8 m); column temperature 130 °C; injection and detection temperature 250 °C. The peak area ratio between the citronellol acetate and linalool is calculated from the chromatogram and finally, the calibration curve is prepared [19]. From this calibration curve, the lipase activities were evaluated. The effect of the reaction cycle on activity was examined for the same lipase. One reaction period was 20 hrs. After each run, the lipase preparation was washed with fresh hexane (10 mL) and used further. The effect of water content in solvent on activity was measured by a reaction containing water (10-30%) mixed with hexane. A reaction temperature profile was taken for fiber-immobilized lipase, Novozym-435, and free lipase. In that case, heptane (10 ml) was used as the solvent.

5.3 RESULTS AND DISCUSSION

5.3.1 Preparation and characterization of enzyme-immobilized PVB-ZrO_2 hybrid hollow fiber

Fig. 5.2 (a) shows the photograph of the resultant β-galactosidase (βG) immobilized PVB-ZrO_2 hybrid hollow fiber. Uniform dispersion of βG within a hollow fiber was considered though undissolved βG powder remained its original color. The surface of the fiber was nonporous, and inside a large area hollow structure was observed by SEM cross-section [**Fig. 5.2 (b)**]. Compared with the non-immobilized fiber [30], it might have been confirmed that the addition of enzymes didn't alter the hollow structure significantly.

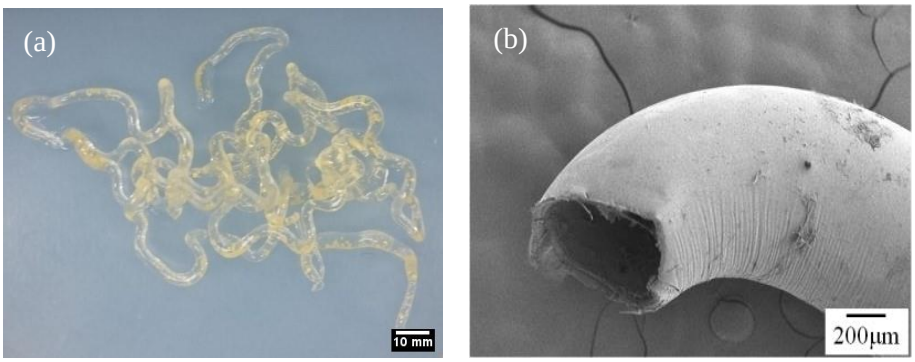

Fig. 5.2 (a) Overview, and (b) cross-sectional image of βG immobilized PVB-ZrO_2 hybrid hollow fiber.

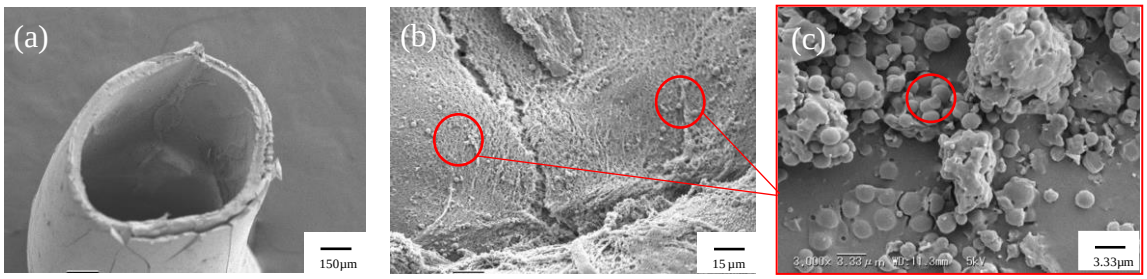

Fig. 5.3 (a,b) SEM view of lipase immobilized on PVB-ZrO_2 hybrid hollow fiber, (c) CHIRAZYME particles (Red circle).

Besides, the immobilization of lipase (CHIRAZYME) was confirmed by the presence of white particles at the inner wall of the hollow sphere (**Fig. 5.3**). The stability of immobilized (βG) fiber in various solutions was compared with Ca-alginate beads. The fiber showed its stability in phosphate buffer and electrolyte solutions as represented in **Table 5.1** which confirmed the strong coordinate bonding between PVB and $Zr(OBu)_4$.

Table 5.1 Comparative solution stabilities of PVB-ZrO_2 hybrid hollow fiber and Ca-alginate beads (matrices immersed in solution at 37 °C for 2 days).

Aqueous solution	Support matrices	
	Ca-alginate beads	PVB-ZrO_2 hybrid fiber
0.1 M NaCl	Swelling	No change
1.0 M NaCl	Highly swelling	No change
0.1 M $CaCl_2$	No change	No change
1.0 M $CaCl_2$	No change	No change
0.1 M Phosphate buffer (pH 6.0)	Swelling	No change
0.1 M Phosphate buffer (pH 7.0)	Highly swelling	No change
0.1M Phosphate buffer (pH 8.0)	Highly swelling	No change

5.3.2 Enzyme reaction by β-galactosidase immobilized (IβG) PVB-ZrO_2 hybrid fiber

To investigate the activity of IβG, the leakage test of the free enzyme (only β-galactosidase), IβG, immobilized Ca-alginate beads, and pure PVB-ZrO_2 hybrid fiber (without enzyme) were examined. In **Fig. 5.4**, an increase in absorbance was observed for free enzymes due to the presence of the peptide groups. However, compared to a pure PVB-ZrO_2 hybrid fiber, a tiny incremental absorbance was found for IβG at the initial stage and this difference remained the same later. This was thought to be the presence of loosely immobilized enzymes in the vicinity of the surface. It indicates that β-galactosidase was entrap-immobilized firmly in the hollow tube. **Fig. 5.5** shows the effect of substrate concentration on β-galactosidase activity (procedure described in chapter three**)**. Activity increased linearly up to about 0.04 mol/L for each β-galactosidase. The activity of fiber immobilized enzyme was about one-third of its native activity. However, the enzyme immobilized in beads had a lower level of activity, as shown in **Fig. 5.5.**

Furthermore, continuous reaction experiments for substrate (lactose) hydrolysis were performed using a simple bioreactor. **Fig. 5.6** shows that the activity remains close to 60 mg/dL even after 600 hrs. However, the glucose concentration initially increased over 12 hrs and then drop-down to 90 mg/dL. We consider two reasons behind that. One could be done by the untrapped free enzyme held in the surface of the fiber network and hydrolyzing the substrate at a higher rate while the other reason could be the reaction inhibition process done by the degraded glucose or galactose.

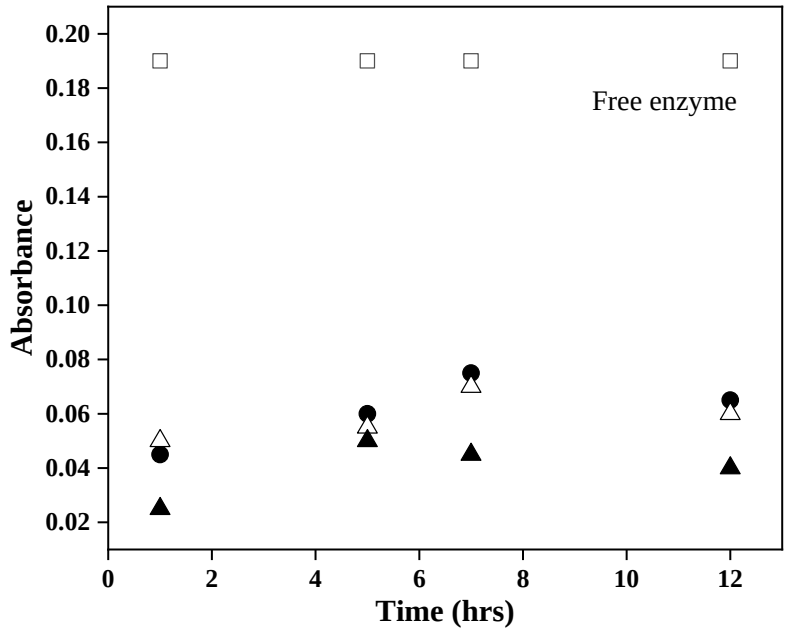

Fig. 5.4 Time course of absorbance at 280 nm of the water containing (□) free enzyme (●) immobilized PVB-ZrO_2 hybrid fiber, (△) immobilized Ca-alginate beads, and (▲) pure PVB-ZrO_2 hybrid fiber.

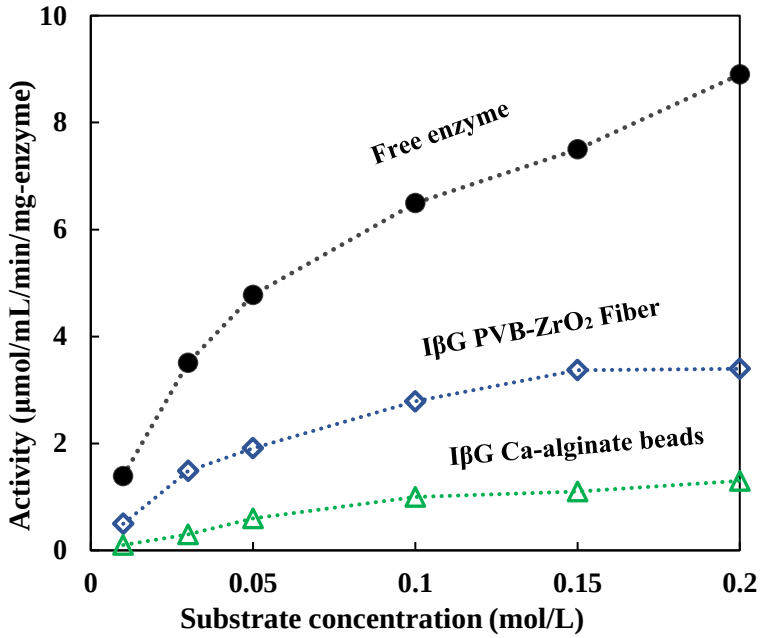

Fig. 5.5 Effects of substrate concentration on *β*-galactosidase activities for free enzyme, IβG PVB-ZrO_2 hybrid fiber, and βG immobilized Ca-alginate beads.

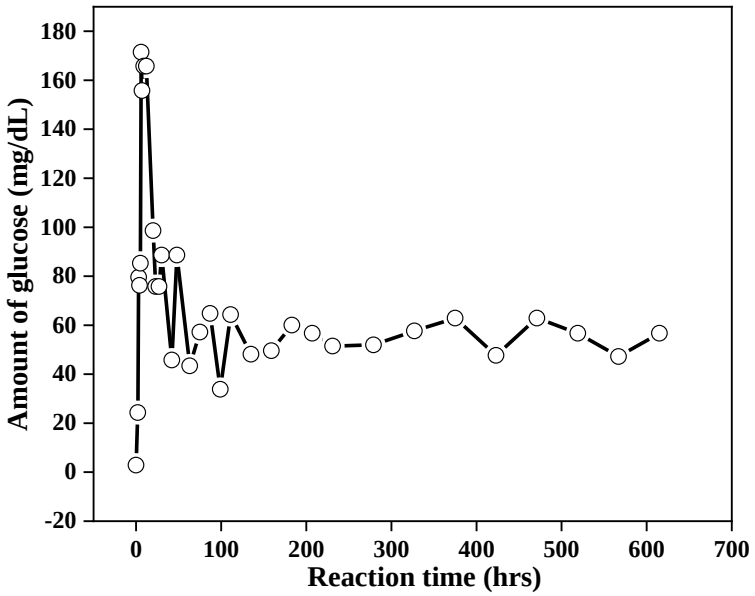

Fig. 5.6 Continuous lactose hydrolysis reaction in bio-reactor.

The applicability of the Michaelis-Menten law was ascertained in the low concentration range by an Eadie-Hofstee plot (**Fig. 5.7**). Here this plot was created by transforming **Fig. 5.5** into it. The apparent Michaelis constant (K_m: mol/l) and maximum reaction velocity (V_{max}: µmol/min/mg-enzyme) were obtained from the slope and intercept of the straight line. A plot of V_0 against V_0/[S] will hence yield V_{max} as the y-intercept, V_{max}/K_m as the x-intercept, and K_m as the negative slope. The apparent K_m of IβG (0.079) was a little higher than that of the free enzyme (0.067), while the V_{max} of IβG (4.9) showed a significantly lower value than the free enzyme (11.5) as projected in **Table 5.2**. This resultant K_m value of IβG confirms comparatively the less affinity of the substrate to the enzyme. The surface of the immobilized PVB-ZrO_2 was non-porous; hence there was a possibility of very fewer diffusion of the substrate into the fiber. So, preferably the enzyme entrapped on the fiber surface only participated in the reactions considered. But this K_m value shows better activity than cylindrical non-hollow CA-ZrO_2 hybrid fiber (Fiber diameter 200 µm-1000 µm, K_m= 0.174) prepared by Nakane et al.. For CA-ZrO_2 fiber, the lower surface area restricts the diffusion of the enzyme into the fiber [10]. However, the reduced V_{max} value of PVB-

Table 5.2 Kinetic parameters for the free enzyme, IβG PVB-ZrO_2 hybrid hollow fiber, and immobilized Ca-alginate beads.

β-galactosidase form	Enzyme kinetic parameters	
	K_m (mol/l)	V_{max} (µmol/min/mg-enzyme)
Free enzyme	0.067	11.5
Immobilized (PVB-ZrO_2 fiber)	0.079	4.9
Immobilized (Ca-alginate beads)	0.158	2.2

ZrO_2 fiber was thought to be induced by steric hindrance of the enzyme and substrate to the carrier. This lower V_{max} value also declares that the enzyme that took part in the catalysis reaction is saturated early with its substrate.

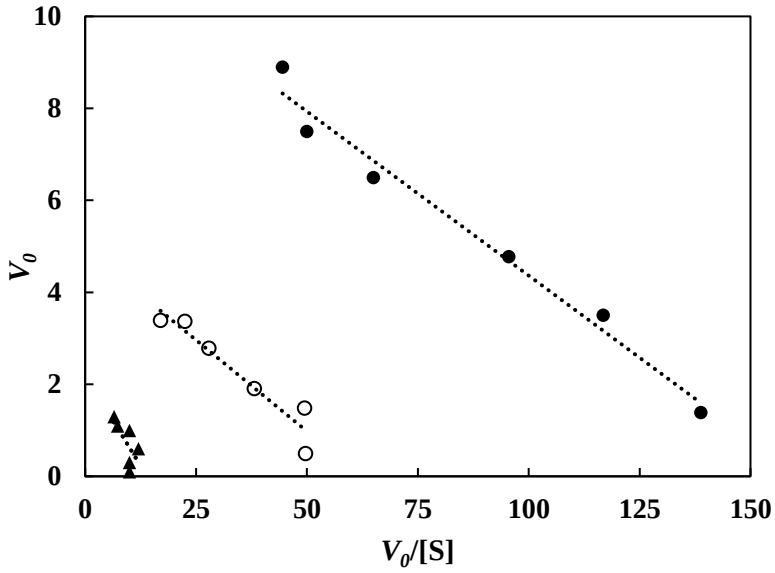

Fig. 5.7 Eadie-Hofstee plot; (○) immobilized PVB-ZrO_2 hybrid fiber, (▲) immobilized Ca-alginate beads, (●) free**.**

Since the immobilized enzyme is subjected to undergo repetitive reactions, it is very crucial to maintain good stability of the fiber. **Fig. 5.8** shows the effect of repeated use on the residual activity of IβG, tested by repeating a 15 min reaction on the same fiber at 10 min intervals. For PVB-ZrO_2 hybrid hollow fiber, about 90% of the initial activity was held after 10 reaction cycles, suggesting that β-galactosidase does not leak from the fiber in significant amounts. On the other hand, a similar experiment with enzyme-immobilized alginate beads demonstrated drastic decreases in activity. This noticeable difference between the durability of Ca-alginate beads and PVB-ZrO_2 hybrid fiber may cause by their different matrix formation mechanism (ionic reaction of alginate bead versus coordinate bond for PVB-ZrO_2 hybrid fiber).

The dependence of the immobilized enzyme catalytic activity on pH was compared with those of the free enzyme and alginate beads. **Fig. 5.9** shows the pH profiles versus the relative activity curve for each enzyme. The optimal pH ranges of the free enzyme are around 4.5. But the immobilized enzyme confirmed greater activity levels at higher pH ranges (4.5-6.0) compared to the other two. Since, the β-galactosidase has two active-site carboxyl groups, one protonated and one ionized; these side chain carboxyl groups are weak acids but can exist as $–COO^-$ (as nucleophile) and –OH (as proton donor) in the same time around neutral pH [31]. The changes in optimum pH may depend on the charge of the enzyme protein and the fiber surfaces. It seems that the changed electronic state occurred on the enzyme sites whether Zr alkoxide could show amphoteric ion-exchange property against the solution pH [10]. However, alginate beads have shown lower activity at higher pH ranges. **Fig. 5.10** shows the relationship between the reaction temperature and the activity level. The optimum temperature for both immobilized β-

galactosidases was more active in a higher temperature range than the free enzyme. This is because the fixation made it less likely to be affected by heat, so the optimal temperature shifted. Besides, compared to the free enzyme, the immobilized enzyme maintains its activity even at high temperatures. This is probably because the immobilization made it difficult to thermal modification of three-dimensional structured enzyme. Furthermore, in the higher temperature range, the PVB-ZrO_2 fiber was more active than the alginate beads. This could be due to the soft immobilization of enzyme on the alginate gel, in which thermal denaturation is favorable.

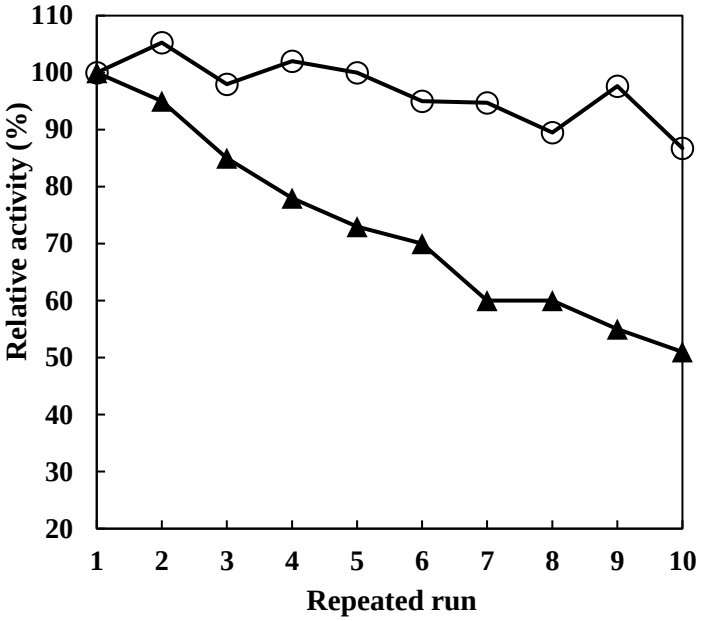

Fig. 5.8 Effect of repeated run on enzyme activities. Initial activity was assumed 100% for pH 4.6 and temperature 37.5 °C; (○) for immobilized PVB-ZrO_2 hybrid fiber, and (▲) for immobilized Ca-alginate beads.

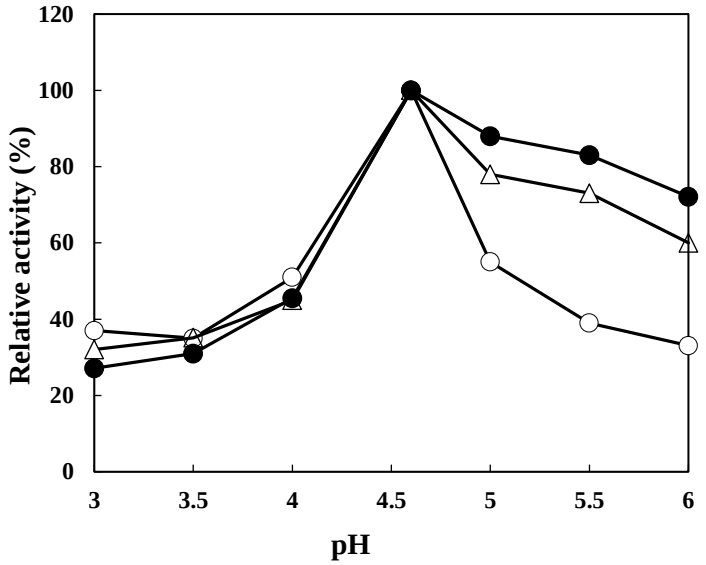

Fig. 5.9 Effect of pH on enzyme activities. The optimal pH was 4.6; adopted as 100%; (○) free, (●) immobilized PVB-ZrO_2 hybrid fiber, (△) immobilized Ca-alginate beads.

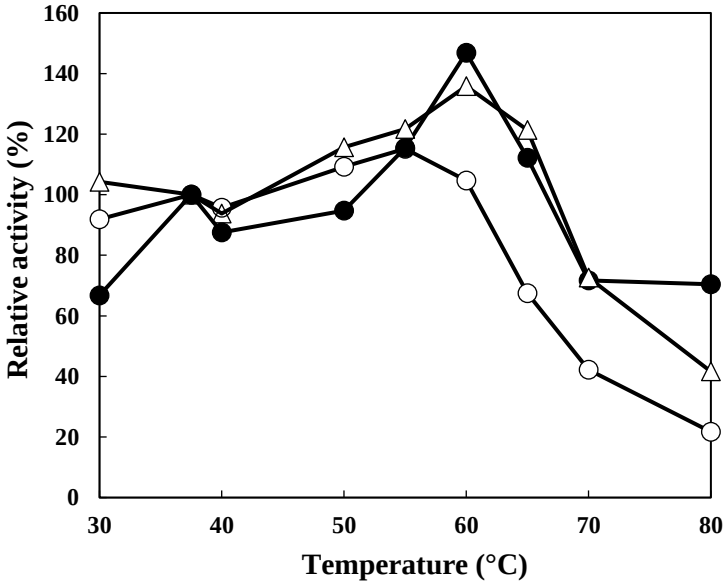

Fig. 5.10 Effect of temperature on enzyme activities. Activity at 37.5 °C was adopted as 100%; (○) free, (●) immobilized PVB-ZrO_2 hybrid fiber, (△) immobilized Ca-alginate beads.

5.3.3 Organic reactions by immobilized lipase (IL)

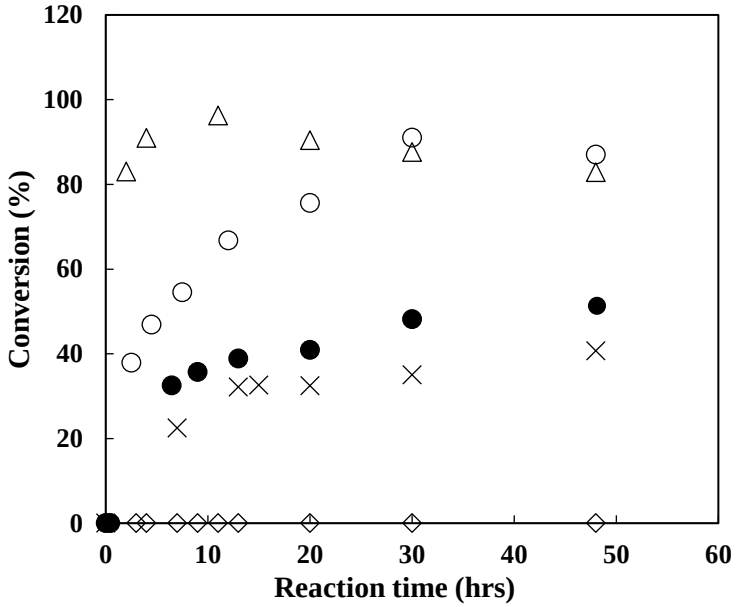

Fig. 5.11 Time course of lipsase-catalyzed synthesis of citronellyl acetate. Esterification was carried out in hexane at 30 °C; (○) free, (●) immobilized PVB-ZrO_2 hybrid fiber, (△) Novozyme, (×) immobilized CA-ZrO_2 hybrid, and (◇) pure PVB-ZrO_2 hybrid fiber.

Fig. 5.11 shows the time courses of the synthesis of citronellyl acetate by IL. Though the esterification rate was slow initially for IL, the conversion increased with progressed reaction time and finally reached 52% after 50 hrs. However, free lipase has shown better susceptibility against raised temperature. In the case of IL, this was thought to be less diffusion of substrates towards the active sites of lipase in the fiber, and probably catalysis by IL was mostly done at the surface of the fiber [11]. Compared to CA-ZrO_2 hybrid fiber immobilized lipase, IL on PVB-ZrO_2 hybrid fiber shows a higher conversion rate and longer reaction activity. Although CA-ZrO_2 hybrid fibers and PVB-ZrO_2 hybrid fibers had little difference in fiber diameter (**Table 5.3**), only the hollow structure and increased specific surface area of fiber made it possible to have more contact between lipase and substrate, which eventually led to more ester synthesis.

Table 5.3 Effect of spinning solution variation on the fiber matrix structure.

Fiber type	Diameter (μm)	Std. deviation (μm)
PVB-ZrO_2	718	43.1
CA-ZrO_2	678	57.1

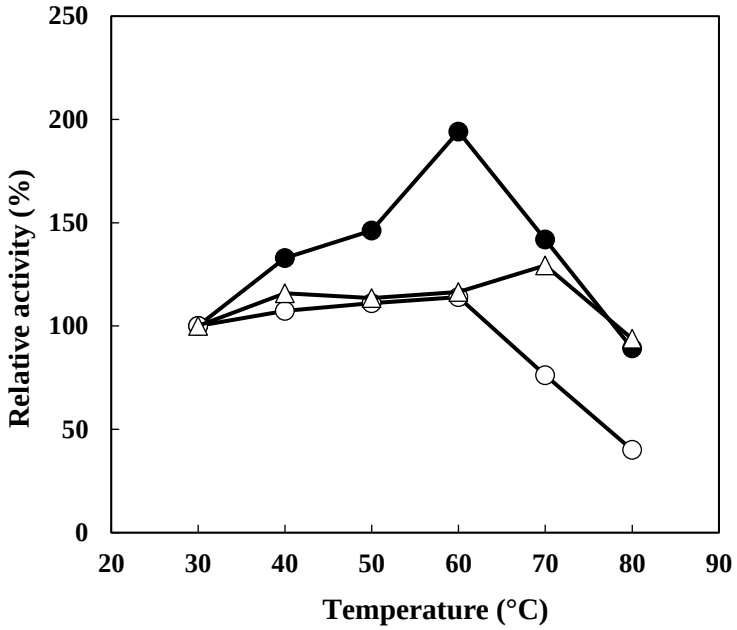

Fig. 5.12 Temperature profile of lipase-catalyzed synthesis of citronellyl acetate. Esterification was carried out in heptane for 20 hrs. Activity at 30 °C was adopted as 100%; (○) free (●) immobilized PVB-ZrO_2 hybrid fiber, and (△) Novozymes.

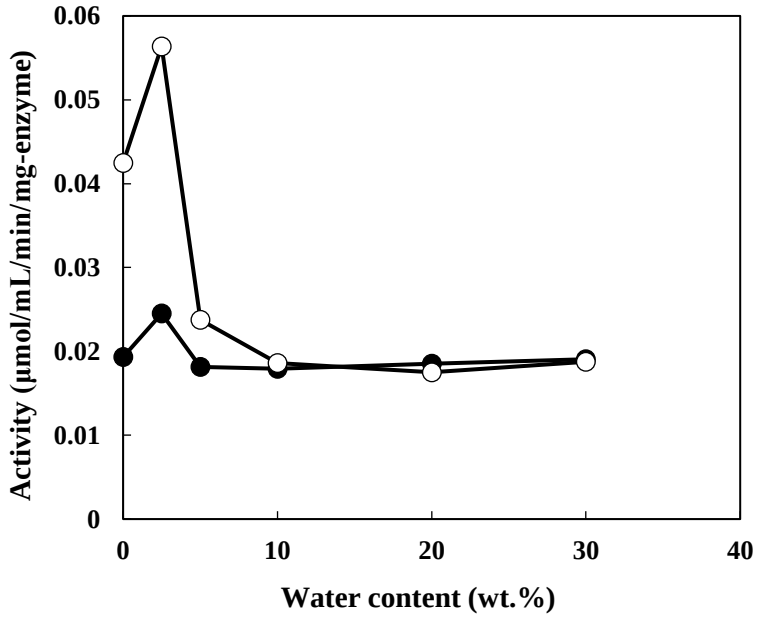

Fig. 5.13 Effect of water content on lipase-catalyzed synthesis of citronellyl acetate at 30 °C; (○) free and (●) immobilized PVB-ZrO_2 hybrid fiber.

Fig. 5.12 shows the effect of reaction temperature on the esterification. The figure clearly shows evidence of good activity for IL at a higher temperature range. This is due to the rigid immobilization of lipase on hollow fibers made the prevention of thermal denaturation. However, ester catalysis at the water/oil interface results in the dehydration of the hollow fiber which led to activity decrement at above 60 °C [11]. **Fig. 5.13** shows the effect of water content on the enzyme activity in the esterification reaction. Generally, water acts as an inhibitor and prefers to reduce enzyme activity. That's why it was likely to decrease activity for both cases when more water is involved in the reaction. But, compared to the immobilized lipase, free lipase was strongly affected by the presence of water and showed more vulnerability up to saturation. It may be caused by the decreasing contact area between the lipase and the substrate resulting from hydration and aggregation of the lipase particles in water. Usually, enzymes require a small amount of water in order to retain the conformation of their active sites in the organic solvent. Also, water plays an important role in maintaining the stability and polarity of the active site, but an excessive amount of water leads to enzyme inactivation. However, at 10 wt.% (water content 1 g) and afterward, the bulk water content did not influence the activity of free and immobilized lipase. In **Fig. 5.14**, the activities of lipase powder, and lipase immobilized PVB-ZrO_2 hybrid fiber are plotted against the number of reaction cycles. After 8 runs IL retained about 62% of the activity level of the first run, whereas the activity for free lipase dropped steeply after the second run and reached about 10% at the end. The activity decrement of free lipase might be caused by the less contact area between substrate and enzyme resulting from adsorbed water onto lipase molecules due to hydration [11]. Indeed, lipase powder develops a gelatinous mass by hydration which restricts it not to reuse [32]. Conversely, immobilized PVB-ZrO_2 hybrid fiber can be recovered very easily from the reaction solution after a certain period.

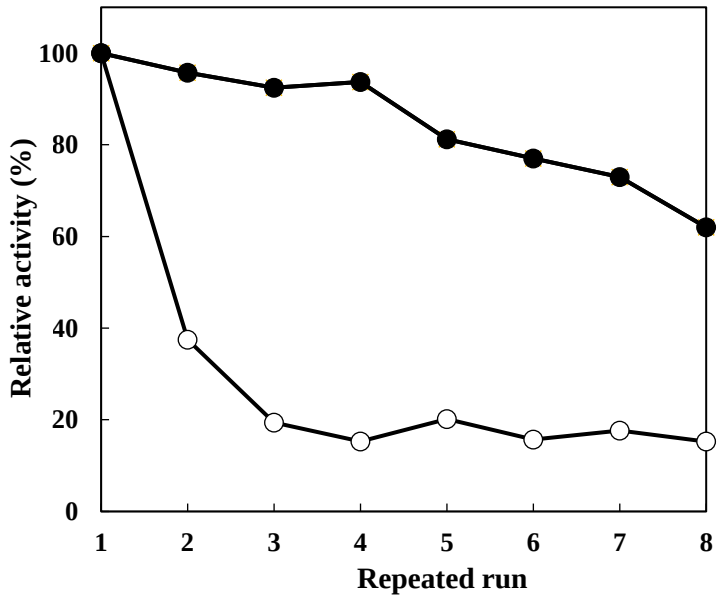

Fig. 5.14 Effect of repeated runs on lipase catalyzed synthesis of citronellyl acetate. Activity of first run was adopted as 100%; (○) free and (●) immobilized PVB-ZrO_2 hybrid fiber.

5.4 CONCLUSION

An air gap spinning method was developed to prepare a coordinately bonded PVB-Zr alkoxide hybrid hollow fiber. Afterward, PVB-ZrO_2 hybrid fiber may prove to be an important support matrix for entrap-immobilizing β-galactosidase and lipase due to its low-cost, larger surface area, and stability in electrolyte solutions, phosphate buffer, and organic solvents. Conversion of lactose to glucose and galactose performed by immobilized β-galactosidase (IβG) retained much of their activity in wider ranges of pH and temperature than that of free β-galactosidase. Moreover, immobilized lipase (IL) appeared to be an effective catalyst for terpene ester synthesis in organic solvents. IL showed stability over repeated runs, water content change, and reaction temperature for different organic solvents. Overall, the activity of the immobilized enzyme became higher for the increased specific surface area of the hybrid fiber which indicates that hydrolysis and catalysis both occurred in the vicinity of the hollow structure. Thus, we conclude that PVB-ZrO_2 hybrid hollow fiber would be a useful enzyme carrier for lactose hydrolysis and ester synthesis in various reaction systems.

REFERENCES

1 J. Wen and G. L. Wilkes, *Chemistry of Materials*, 1996, **8**, 1667–81.

2 S. A. Ansari, R. Satar, S. Kashif Zaidi and A. Ahmad, *International Scholarly Research Notices*, 2014, **2014**, 163987.

3 Y. Ikeda, Y. Kurokawa, K. Nakane and N. Ogata, *Cellulose*, 2002, **9**, 369–379.

4 S. Haghju, M. R. Bari and M. A. Khaled-Abad, *Carbohydrate Polymers*, 2018, **200**, 137–143.

5 N. Vasileva, V. Iotov, Y. Ivanov, T. Godjevargova and N. Kotia, *International Journal of Biological Macromolecules*, 2012, **51**, 710–719.

6 R. R. Monteiro, P. J. Lima, B. B. Pinheiro, T. M. Freire, L. M. Dutra, P. Fechine, L. R. Gonçalves, M. de Souza, J. Dos Santos and R. Fernandez-Lafuente, *International Journal of Molecular Sciences*, 2019, **20**, 4018.

7 K. Won, S. Kim, K.-J. Kim, H. W. Park, and S.-J. Moon, *Process Biochemistry*, 2005, **40**, 2149–2154.

8 W.-Z. Lang, J.-P. Shen, Y.-X. Zhang, Y.-H. Yu, Y.-J. Guo and C.-X. Liu, *Journal of Membrane Science*, 2013, **430**, 1–10.

9 K. Nakane, K. Mizutani, R. Zhang, K. Sugimoto and N. Ogata, *World Journal of Engineering*.

10 K. Nakane, T. Ogihara, N. Ogata and Y. Kurokawa, *Journal of Materials Research*, 2003, **18**, 672–676.

11 K. Nakane, K. Kuranobu, T. Ogihara, N. Ogata and Y. Kurokawa, *Sen'i Gakkaishi*, 2003, **59**, 99–103.

12 C. A. White and J. F. Kennedy, *Enzyme and Microbial Technology*, 1980, **2**, 82–90.

13 A. H. Bhuiyan, T. Nagakawa and K. Nakane, *Journal of Applied Polymer Science*, 2020, **138**(14), 50164.

14 L. Betancor, H. R. Luckarift, J. H. Seo, O. Brand and J. C. Spain, *Biotechnology and Bioengineering*, 2008, **99**, 261–267.

15 Y. Wang, X. Wang, G. Luo and Y. Dai, *Bioresource Technology*, 2008, **99**, 3881–3884.

16 J. Synowiecki and S. Wolosowska, *Enzyme and Microbial Technology*, 2006, **39**, 1417–1422.

17 S. Salman, S. Soundararajan, G. Safina, I. Satoh and B. Danielsson, *Talanta*, 2008, **77**, 490–493.
18 S. F. D'souza, *Current Science*, 1999, **77**, 69–79.
19 Y. Ikeda and Y. Kurokawa, *Journal of American Oil Chemists' Society*, 2001, **78**, 1099–1103.
20 M. M. Elnashar, G. E. Awad, M. E. Hassan, M. S. Mohy Eldin, B. M. Haroun, and A. I. El-Diwany, *The Scientific World Journal*, 2014, **2014**, 571682.
21 C. Mateo, J. M. Palomo, G. Fernandez-Lorente, J. M. Guisan and R. Fernandez-Lafuente, *Enzyme and Microbial Technology*, 2007, **40**, 1451–1463.
22 T. Haider and Q. Husain, *Biochemical Engineering Journal*, 2009, **43**, 307–314.
23 S. Datta, L. R. Christena and Y. R. S. Rajaram, *3 Biotech*, 2013, **3**, 1–9.
24 J. C. Dos Santos, H. L. Bonazza, L. J. de Matos, E. A. Carneiro, O. Barbosa, R. Fernandez-Lafuente, L. R. Gonçalves, H. B. de Sant'Ana and R. S. Santiago-Aguiar, *Biotechnology Reports*, 2017, **14**, 16–26.
25 O. Barbosa, R. Torres, C. Ortiz, Á. Berenguer-Murcia, R. C. Rodrigues and R. Fernandez-Lafuente, *Biomacromolecules*, 2013, **14**, 2433–2462.
26 U. Hanefeld, L. Gardossi, and E. Magner, *Chemical Society Reviews*, 2009, **38**, 453–468.
27 R. A. Sheldon and S. van Pelt, *Chemical Society Reviews*, 2013, **42**, 6223–6235.
28 C. Garcia-Galan, Á. Berenguer-Murcia, R. Fernandez-Lafuente and R. C. Rodrigues, *Advanced Synthesis & Catalysis*, 2011, **353**, 2885–2904.
29 R. C. Rodrigues, C. Ortiz, Á. Berenguer-Murcia, R. Torres and R. Fernández-Lafuente, *Chemical Society Reviews*, 2013, **42**, 6290–6307.
30 A. H. Bhuiyan, T. Nagakawa and K. Nakane, *Journal of Applied Polymer Science*, 2021, **138**, 50164.
31 Q. Z. K. Zhou and X. D. Chen, *Biochemical Engineering Journal*, 2001, **9**, 33–40.
32 K. Nakane, T. Hotta, T. Ogihara, N. Ogata and S. Yamaguchi, *Journal of Applied Polymer Science*, 2007, **106**, 863–867.

This article was published in the *Journal of Materials Science*, 2021; 56, 8668-8678.

CHAPTER SIX

6. STRUCTURAL ANALYSIS AND DYE REMOVAL BEHAVIOR OF AMORPHOUS TITANIA EMBEDDED POLY(VINYL BUTYRAL) HYBRID FIBER

6.1 INTRODUCTION

Synthetic dyes are considered the most perilous type of pollutant, posing a threat to both human health and aquatic life [1]. Among them, methylene blue (MB) has a planar structure and is highly soluble in water. As a result, it may damage marine life due to hindering the entrance of sunlight into water bodies, and reoxygenation of the marine system is interrupted. Although MB is not poisonous, it can induce health problems, such as chest pain, cyanosis, dizziness, high blood pressure, nausea, and abdominal pain when consumed in amounts greater than 7.0 mg/kg [2]. Furthermore, light can effortlessly photosensitize the MB, causing it to release detrimental oxygen that can harm our DNA structure, especially when present in large volumes [3].

In the past, several techniques have been employed for dye removal, including advanced oxidation, membrane separation, electrolysis, and photocatalytic degradation. But, visible-light-induced photocatalysis and adsorption methods are considered the most effective techniques in the field of organic pollutant remediation because of their high efficiencies, low cost, less harmful by-products, and low energy consumption [4].

As a porous material, metal-organic frameworks (MOFs) represent diverse applications in wastewater treatment, generated from organic-inorganic hybrids [1]. Recently, MOF-based composites such as MIL-101(Fe)@PDopa@Fe_3O_4, Fe_3O_4/MIL-101(Fe), α-Fe_2O_3@UiO-66, and BiOI@UIO-66(NH_2)@g-C_3N_4 have been developed to establish the efficacy of MOFs in this field [4]. In addition, carbon-based materials especially graphene oxide and reduced graphene oxide have shown promising results as photocatalysts in dye degradation [5].

Furthermore, organic-inorganic hybrid structures driven by transition metal titanium dioxide (TiO_2) are also effective in the field of adsorption and photodegradation for organic pollutants [6]. Although crystalline TiO_2 is suitable for photocatalytic reactions due to low toxicity, chemical-thermal stability, and good resistance to photo corrosion, it has several well-known drawbacks, including ineffective utilization of visible and near-infrared light and high recombination of photo-generated charge carriers, which greatly hinder the improvement of its photocatalytic activity [7]. Conversely, amorphous metal oxides have several potential advantages over crystalline phases [8]: they are easier to make at room temperature, with a significantly larger surface area, and can have a variety of chemical compounds doped or embedded into their matrices. Despite amorphous TiO_2 ($amTiO_2$) having long been thought to be nearly inactive due to the easier recombination of photogenerated electrons and holes when exposed to light [9], some research has found that the surface area of $amTiO_2$ is preferable to its crystal structure for increasing photocatalytic activity. Buddee *et al*. developed curcumin-sensitized $amTiO_2$ for the successful photodegradation of MB dye [6]. Later, Wang *et al*. showed that $amTiO_2$ was faster than crystalline TiO_2 for the visible-light-induced photodegradation of rhodamine B (Rh-B), implying that $amTiO_2$ was a good mediator for electron transfer from excited dyes to oxygen [10]. They stated

that the synergistic dye degradation dynamics were mainly controlled by the higher surface area of amTiO$_2$ rather than crystallinity. Meanwhile, in the past, Kanna *et al*. [11] and Sriprang *et al*. [12] effectively decolorized crystal violet (CV) and malachite green (MG) dyes, respectively, by amTiO$_2$ where the adsorption property of the adsorbent mainly dominated the decoloration process. Consequently, in 2019, we reported not amTiO$_2$ particles, but cellulose acetate (CA) fiber crosslinked amTiO$_2$ (i.e. CA-amTiO$_2$ fibers), decomposing organic dyes, and reducing Cr(VI) when exposed to visible light [13].

Accordingly, herein, we aimed to fabricate a PVB-amorphous titania hybrid fiber considered an efficient candidate for organic dye removal. The fiber was prepared *via* an air gap spinning process. The activity of the fiber was thought suitable for the adsorption of MB dye since the matrix of the fabricated fiber has anionic functional groups, suggesting some possible interactions with MB dye. This study also investigated the possibility of using this fiber as a photocatalyst for MB decomposition upon exposure to visible light. The ability of the developed PVB-amorphous titania fiber (PVB-amTiO$_2$F) for MB dye removal is estimated and discussed. The adsorption kinetics of the process and the possibility of reuse of PVB-amTiO$_2$F are also assessed.

6.2 EXPERIMENTAL

6.2.1 Materials

PVB (Mowital® PVB B60H), with a molecular weight of 50–60 kDa was received from Kuraray Co. Ltd., Japan. Titanium (IV) isopropoxide (TTIP) was purchased from Fujifilm Wako Pure Chemical Corporation, Japan. Aeroxide P25 (commercial TiO$_2$ powder) was purchased from Nippon Aerosil Co. Ltd., Japan. The acetone and ethanol used in this study were dehydrated by 3A molecular sieves. Several dyes, namely methylene blue (MB), methyl orange (MO), and rhodamine B (Rh-B) were purchased from Nacalai Tesque Inc., Japan. All reagents were of analytical grade and used without further purification.

6.2.2 Preparation of PVB-amTiO$_2$F and a comparison sample

The sample preparation method [14], known as air gap spinning, is shown schematically in **Fig. 6.1**. Firstly, 2 g PVB and 8 g of dehydrated ethanol were used to make a 20 wt.% PVB-ethanol solution (spinning solution). To make a coagulation solution, TTIP was dissolved in dehydrated acetone at different concentrations. The PVB spinning solution (2 mL) was then spun from a syringe into

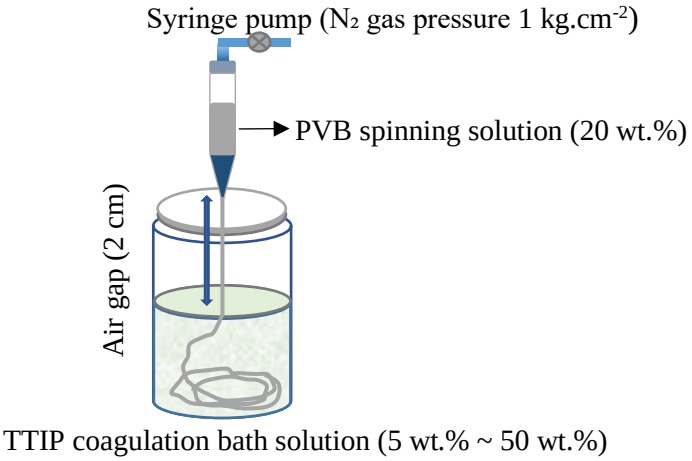

Fig. 6.1 Preparation method of PVB-Ti alkoxide hybrid fiber by air gap spinning.

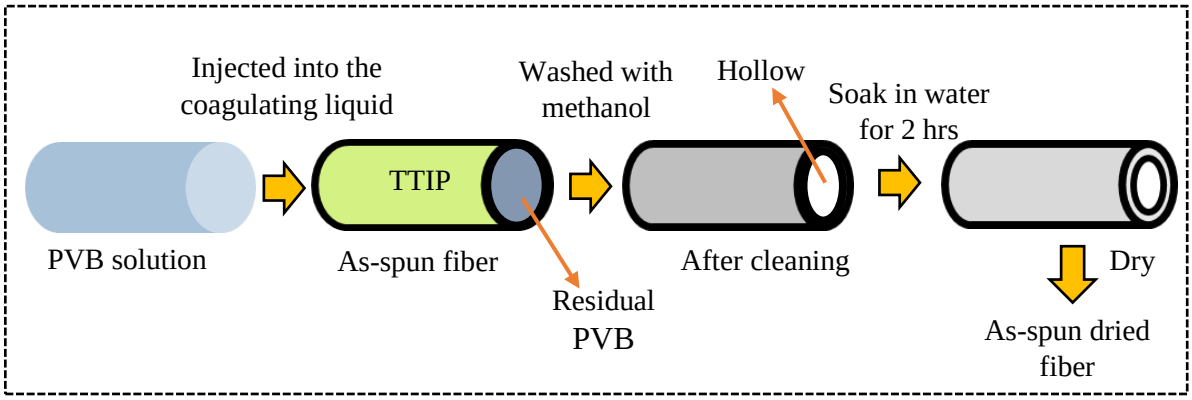

Fig. 6.2 Schematic principle of as-spun fiber preparation.

a stirred coagulation bath with a syringe pump, rapidly forming a fibrous material (PVB-Ti alkoxide hybrid fiber). After 30 min immersion time, the resultant fibers were repeatedly washed with methanol to eliminate unreacted components, followed by soaking in distilled water to obtain the hydrolyzed product of TTIP (**Fig. 6.2**). This as-spun fiber is denoted PVB-amTiO_2F. All samples were vacuum-dried before being used for other measurements. The TTIP bath concentrations were 5 wt.%, 10 wt.%, 15 wt.%, 20 wt.%, and 50 wt.%. The nozzle-to-bath (air gap) distance, spinning solution volume, spinning rate, and N_2 gas pressure were 2 cm, 2.0 mL, 4 mL/min, and (1 kg.cm^{-2}) respectively. For comparison, the amTiO_2 powder was also prepared according to previous research [10]. Here, 5 mL TTIP was added dropwise into 50 mL distilled water without the addition of any strong acids or organic solvents. The instantly formed white suspension was kept at room temperature for 2 hrs to allow for complete hydrolysis, then separated by a sieve and washed five times with 20 mL of distilled water to remove any impurities. The powders were then dried in an oven at 70 °C for 2 hrs. The as-prepared amorphous TiO_2 powder is designated amTiO_2P.

6.2.3 Characterization

A Keyence scanning electron microscope (SEM) (VE-9800, Keyence Co. Ltd., Japan) was used to examine the morphological structure of PVB-amTiO_2F at a voltage of 5 kV. Using an ion coater (SC-701; Sanyu Electron Co. Ltd., Japan), all samples were previously coated with Au/Pd sputtering under a vacuum. Thermogravimetric (TG) measurements were carried out in the air, using a thermogravimetric analyzer (DTG-60, Shimadzu, Japan) at a heating rate of 10 °C/min from 30 to 600 °C. For fibrous samples, an X-ray diffractometer (Ultima-IV, Rigaku, Japan) was used to perform crystallographic measurements. In addition, a separate X-ray diffraction (XRD) measurement was taken using a CuKα with Ni filter (30 kV, 15 mA) (Rigaku MiniFlex II, Japan) for the powder sample. For comparison, the crystallite size of the powder sample was also calculated using Scherrer's equation. Equation (6.1) can be denoted as:

$$L = \frac{K\lambda}{\beta \cos\theta} \text{ ---------- (6.1)}$$

where θ is the Bragg angle of the peaks (°), λ is the wavelength of the X-ray (0.15418 nm), and β is the line broadening at half the maximum intensity (FWHM) (rad). The shape factor K is 0.89. An infrared (IR) spectrometer (IR Affinity-1, Shimadzu, Japan) arrayed with an attenuated total reflection (ATR) ancillary (MIRacle 10, Shimadzu, Japan) bearing a diamond/ZnSe crystal was used to perform ATR-FTIR experiments at ambient temperature. Nitrogen adsorption isotherms were measured at -196 °C using a BELSORP mini II, MicrotracBEL Corp., Japan. The Brunauer–Emmett–Teller (BET) method was used to compute specific surface areas. From the isotherm, the pore-size distribution (PSD) curves were measured using the Barrett–Joyner–Halenda (BJH) algorithm. X-ray photoelectron spectroscopy (XPS) was performed with a JEOL JPS-9010 (JEOL Ltd., Japan) instrument with Mg-Kα (hν =1253.6 eV) source at a residual gas pressure of $5x10^{-6}$ Pa. Energy dispersive spectroscopy (EDS) was performed coupled with a field emission scanning electron microscope (FE-SEM) (Zeiss Ultra Plus, Carl Zeiss Microscopy GmbH, Germany) to assess the purity and elemental composition of the fibers. Prior, osmium conduction was employed on the fiber surface by using a coating device (HPC-1SW, Japan). The absorption spectra from 400 to 800 nm were recorded using a UV-vis spectrometer (ASV11D, AS ONE Corporation, Japan).

The net charge of the PVB-amTiO_2F surface was measured based on pH changes of a NaCl solution containing 0.2 g of fiber [12]. Initially, the pH of these solutions was adjusted and recorded as the initial pH, pH_i. At the end of the experiment, the pH was measured as the final pH, pH_f. Finally, pH_{pzc} was calculated from the crossover point of the predetermined pH_i vs pH_f plot curve.

6.2.4 Batch adsorption and decomposition studies

Unless otherwise stated, the test dispersions were typically prepared by adding 0.2 g PVB-amTiO_2F fibers to a 10 mL aqueous solution containing 10 mg/L dyes with a specified pH. In the initial stage of the study, the dark adsorption kinetics of the dyes were tested by using a UV-vis spectrometer to monitor dye concentration at regular intervals. Once the adsorption had reached equilibrium, samples immersed in the solution were exposed to visible light. Then dispersion solution was constantly stirred with a stirring bar while being irradiated under a 100 W halogen lamp (Mega-Light100-ROHS, SCHOTT) [13]. The absorbances for MB, MO, and Rh-B were recorded at 664 nm, 463 nm, and 554 nm, respectively for both adsorption and decomposition

measurements [15–17]. Equations (6.2) and (6.3), respectively, were used to calculate adsorption efficiency (%) and adsorption capacity.

$$\text{Adsorption efficiency (\%)} = (C_0 - C_t)/C_0 \times 100 \text{ ---------- (6.2)}$$

$$Q_t\,(\text{mg/g}) = (C_0 - C_t)/m \times V \text{ ---------- (6.3)}$$

where, C_0 and C_t (mg/L) are the dye concentrations at times zero and t, respectively. V (L) is the dye volume, and m (g) is the mass of the fiber.

6.2.5 Adsorption kinetics

The adsorption kinetics of MB onto the PVB-amTiO$_2$F was evaluated using Lagergren pseudo-first-order [18] and pseudo-second-order [19] models by fitting the Q_t data acquired empirically with equations (6.4) and (6.5), respectively;

$$\ln (Q_e - Q_t) = \ln Q_e - k_1 t \text{ ---------- (6.4)}$$

$$t/Q_t = 1/k_2 Q_e^2 + t/Q_e \text{ ---------- (6.5)}$$

Here, Q_e and Q_t symbolize the adsorptive removal capacity of MB under equilibrium conditions and at time t respectively, and k_1 and k_2 are the pseudo-first-order and pseudo-second-order rate constant, respectively.

6.3 RESULTS AND DISCUSSION

6.3.1 Structural analysis by SEM

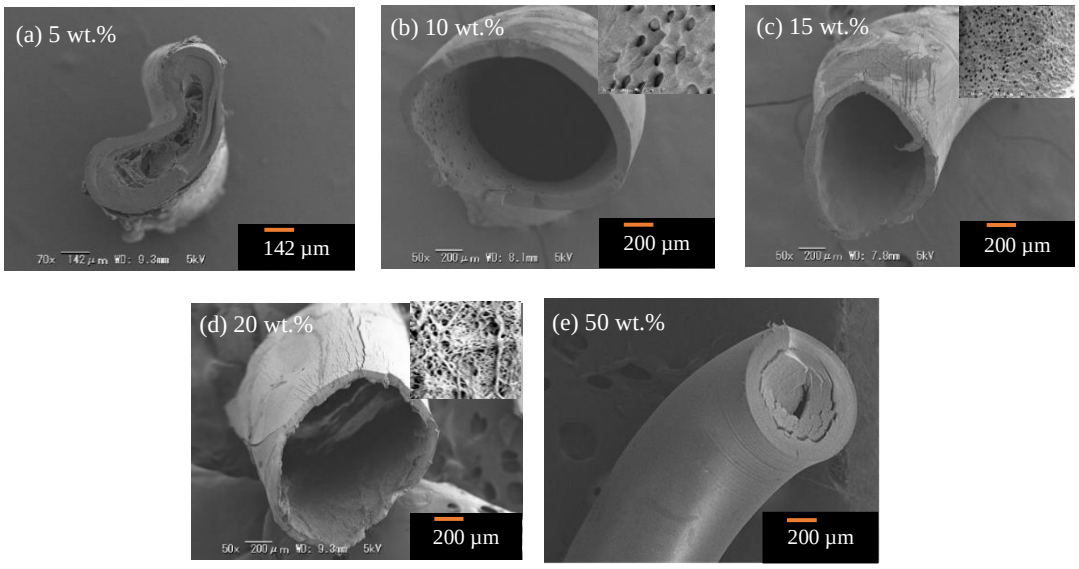

Fig. 6.3 SEM images of the PVB-amTiO$_2$F prepared at TTIP bath concentrations of (a) 5 wt.% (b) 10 wt.%, (c) 15 wt.%, (d) 20 wt.% (insets the inner layer of the fibers), and (e) 50 wt.%.

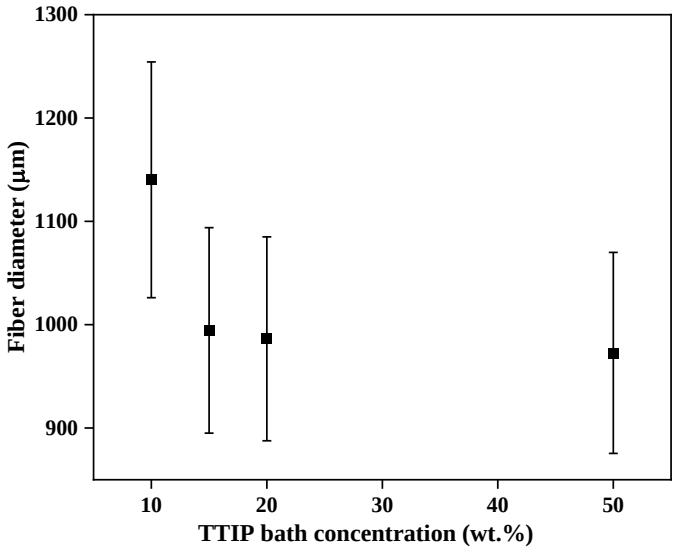

Fig. 6.4 Effect of TTIP bath concentrations on the PVB-amTiO$_2$F diameters.

Fig. 6.3 shows the SEM micrographs of the fibers prepared at various TTIP coagulation bath concentrations. At 5 wt.%, the prepared fibers look like a very entangled and limp structure, making it difficult to remove the remaining PVB. Easy-to-handle fibers could be yielded at concentrations from 10 wt.% to 50 wt.%. These fibers exhibited a core structure that is almost comparable to PVB-zirconia fibers reported by Bhuiyan *et al.* [14]. However, some micropores are observed on the inner wall (inset pictures) of the low-TTIP concentration fibers. At increased bath concentrations, the fibers gained a flattened shape with a reduced hollow structure. The diameter of the fiber decreased as the concentration of the TTIP bath increased, indicating that the alkoxide wt.% had a substantial influence on the fiber structure (**Fig. 6.4**). This was because a higher TTIP concentration restricts the swelling of the PVB solution within the coagulation bath. As a result, the produced fibers were highly brittle (dry stage) and thin in diameter at concentrations close to 50 wt.%. The cross-linking reaction speed between PVB and TTIP was considered slow, which led to some unreacted alkoxide components at lower

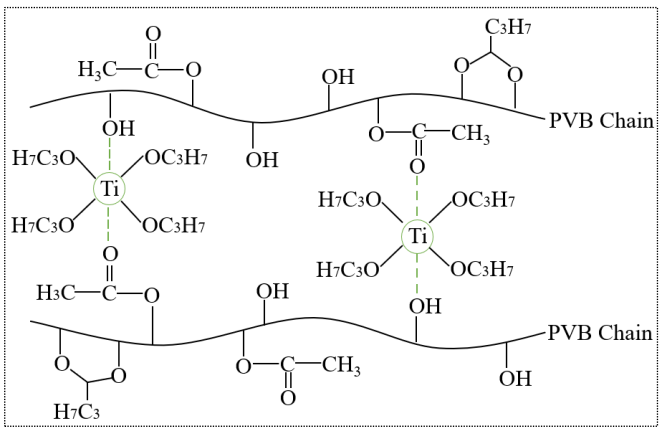

Fig. 6.5 Schematic reaction chemistry of the PVB-amTiO$_2$F formation.

concentrations. The proposed reaction chemistry of the prepared PVB-amTiO2F is depicted in **Fig. 6.5** [20]. The isopropoxy groups in the TTIP would be hydrolyzed during the preparation process and yield hollow hydrous fibers.

6.3.2 TG analysis

Fig. 6.6 shows (a) TG curves and (b) residual TiO_2 weight content for fiber samples as a function of TTIP coagulation bath concentrations. The residual weights in the TG curves correspond to the weight at 600 °C. All samples are thermally decomposed in three stages, as reported by Hanna *et al*. [21]. The first degradation stage was ascribed from room temperature to ~250 °C corresponding to the evaporation of water content in the samples. The degradation of the PVB main chains causes the second stage, which is initiated at ~250 °C and ended at ~440 °C. The third step took place at 440 °C, which indicated the carbonization of the products to ash. With increasing TTIP bath

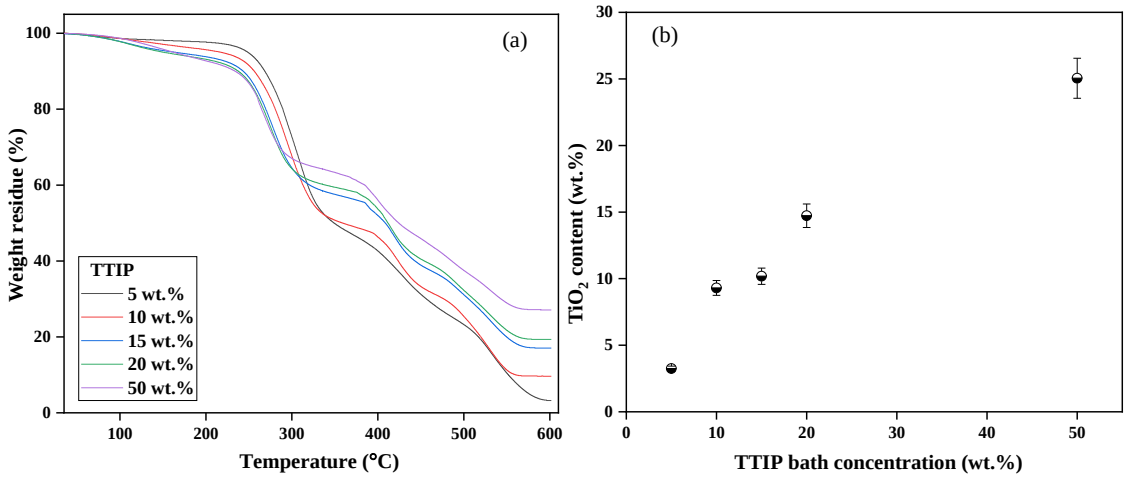

Fig. 6.6 (a) Typical TG profiles, and (b) residual TiO_2 weight of the PVB-amTiO2F samples at 600 °C as a function of TTIP bath concentration.

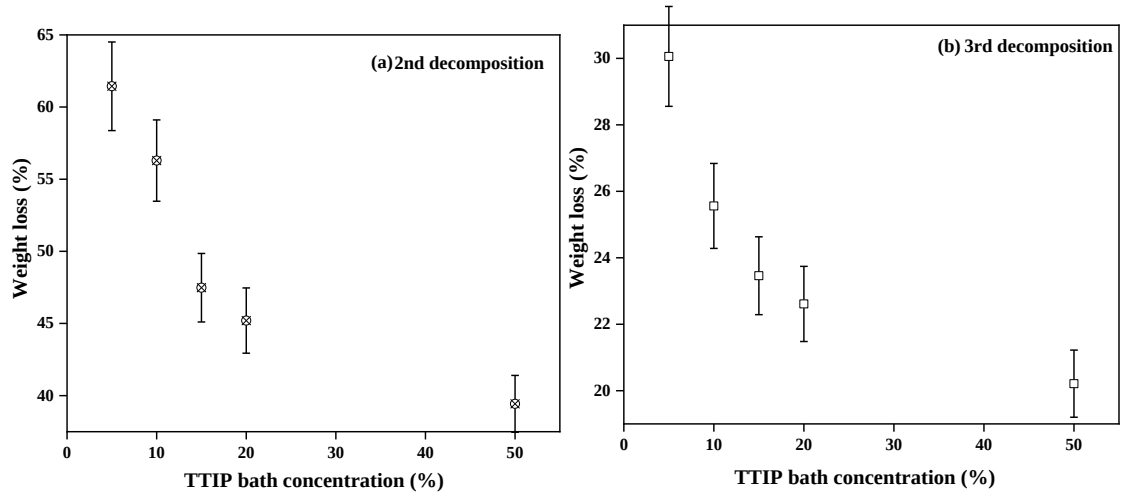

Fig. 6.7 Variation of the weight loss at (a) 2nd decomposition and (b) 3rd decomposition stage as a function of the TTIP bath concentration.

concentration, the residual weight was considered to increase (**Fig. 6.6** (b)). Following that, we were not able to prepare well-structured fibers. However, an increased number of cross-links is assumed for very high TTIP bath concentrations where a spontaneous diffusion of Ti from the fiber's surface to the center is considered. This may be due to the high diffusion of TTIP from the cross-linking point to the PVB polymer chain at higher concentrations. The amount of decomposition in the second and third stages is thought to be affected by the number of reactions between PVB and TTIP, as well as by the diffusion rates of Ti into the PVB polymer chain. The amount of decomposition at the second and third stages is summarized in **Fig. 6.7**. Meanwhile, unless 50 wt.% fibers, morphological characteristics of 10~20 wt.% PVB amTiO$_2$F remained almost the same. But we have considered the 20 wt.% PVB-amTiO$_2$F for subsequent measurements pondering its relative Ti content and internal porous distribution.

6.3.3 ATR-FTIR measurement

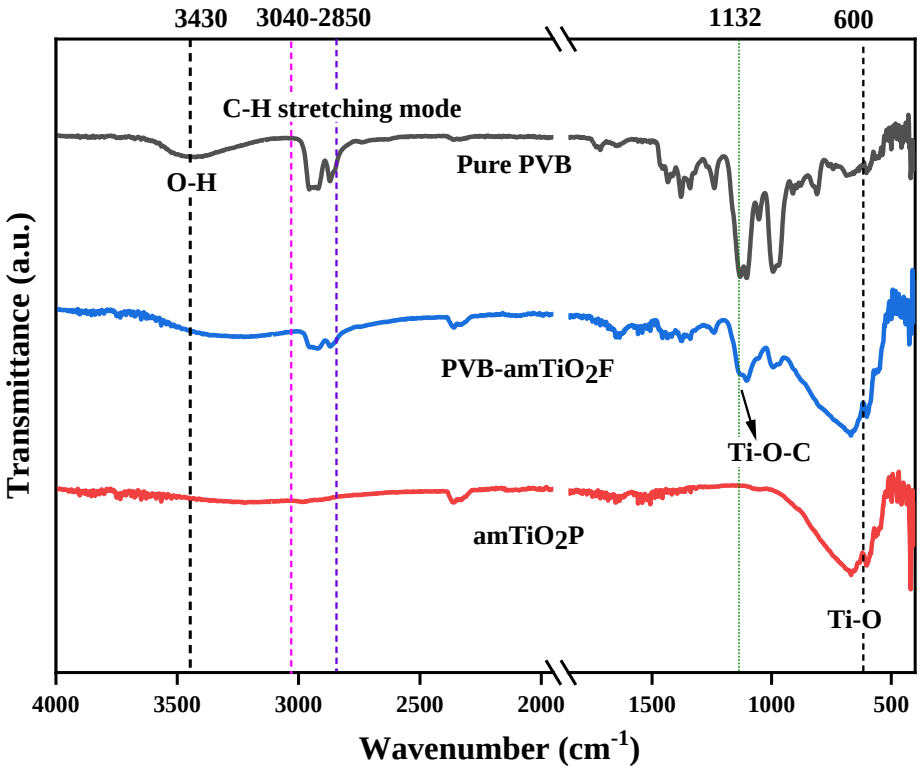

Fig. 6.8 ATR-FTIR spectra of pure PVB, amTiO$_2$P, and PVB-amTiO$_2$F.

FTIR was used to investigate the chemical structures of pure PVB, PVB-amTiO$_2$F, and amTiO$_2$P samples. **Fig. 6.8** shows a comparison of the infrared ATR-FTIR spectra. For pure PVB, there is a wide band corresponding to the —OH group in the range 3200-3600 cm^{-1}, and the stretching modes of C—H in the range 2850-3000 cm^{-1} [22]. Moreover, the bending modes of C—H groups were also discernible in the range 1300-1500 cm^{-1} [23]. However, significant differences were observed in the C—O—C band at the 950-1200 cm^{-1} range. The bands determined at wavenumbers of 1132, 1107, and 1053 cm^{-1} were for typical PVB [22]. These are visible in the measured spectra in **Fig. 6.8**. But their shapes seem to be little affected in the case of the PVB-

amTiO2F sample. In this case, the band at 1053 cm^{-1} has not fully disappeared, but a small shoulder can be seen. However, the C—O—C band is transformed to Ti—O—C at 1132 cm^{-1} due to coordinate bonding between PVB and $Ti(OR)_4$. Also, the peak at 600 cm^{-1} is ascribed to absorption bands of Ti—O, related to flexion vibration [24].

6.3.4 XRD

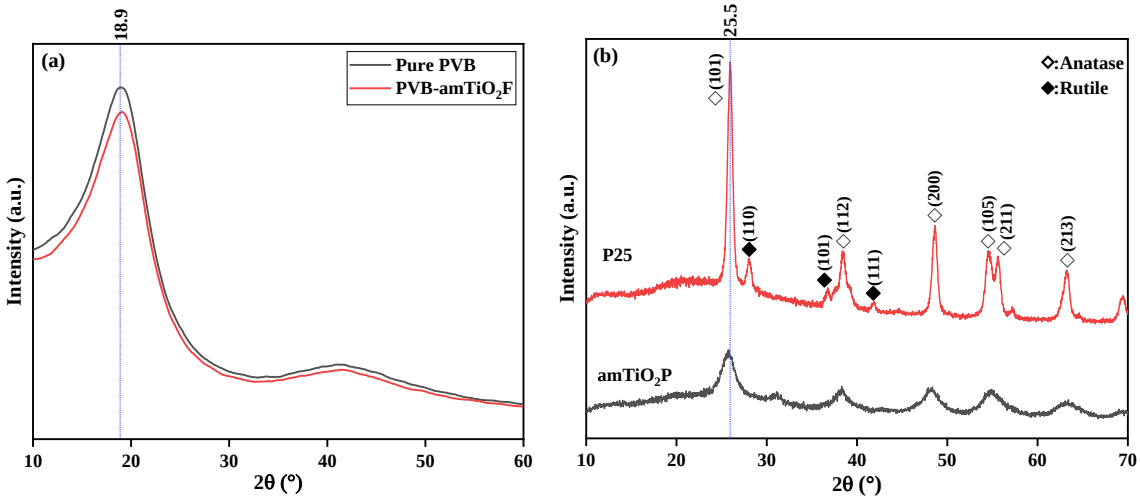

Fig. 6.9 XRD patterns of (a) pure PVB and PVB-amTiO2F; and (b) synthesized amTiO2P and commercial titania powder, P25.

The crystallographic structures and phase alignment of the materials were confirmed by XRD. As shown in **Fig. 6.9** (a), pure PVB has a broad diffraction peak at around 18.9°, suggesting that the polymer matrix is amorphous [25]. However, no characteristic peak of PVB-amTiO2F appeared in this XRD data, indicating that coordinately bonded TiO_2 had a small impact on the fiber's molecular alignment. Furthermore, for confirmation of the characteristic phase of amTiO2 belonging to PVB–amTiO2F, a comparative XRD profile of amTiO2P (hydrolyzed product of TTIP) and commercial P25 is also examined. The diffraction pattern of P25 and amTiO2P is shown in **Fig. 6.9** (b), confirming the identical main peak around the 25.5° value, which corresponds to the anatase (101) phase [26]. We also used Scherrer's method (Lorentz peak fitting) to compute the crystallite sizes of both samples to determine the peak area. The average crystallite sizes were 16.23 nm and 4.32 nm for P25 and amTiO2P, respectively. As a result, it may be concluded that amTiO2P is mostly amorphous titania with traces of crystalline anatase. Therefore, PVB-amTiO2F is suggested to be amorphous despite the presence of small traces of crystal-sized anatase TiO_2.

6.3.5 EDS measurement

To better understand the distribution of Ti within the fiber, we used EDS measurement on the fiber cross-section. C and Ti mapping pictures represented by green and red colors respectively for the fiber samples prepared at different TTIP bath concentrations; shown in **Fig. 6.10**. The illustration shows that Ti mostly existed at the surface for fibers prepared at low TTIP bath concentrations. This small Ti diffusion from the vicinity to the center is thought to be caused by the slow reaction between PVB and TTIP. However, Ti diffusion could be increased and also uniformly distributed across the fibers prepared at higher concentrations (~50 wt.%). Similar

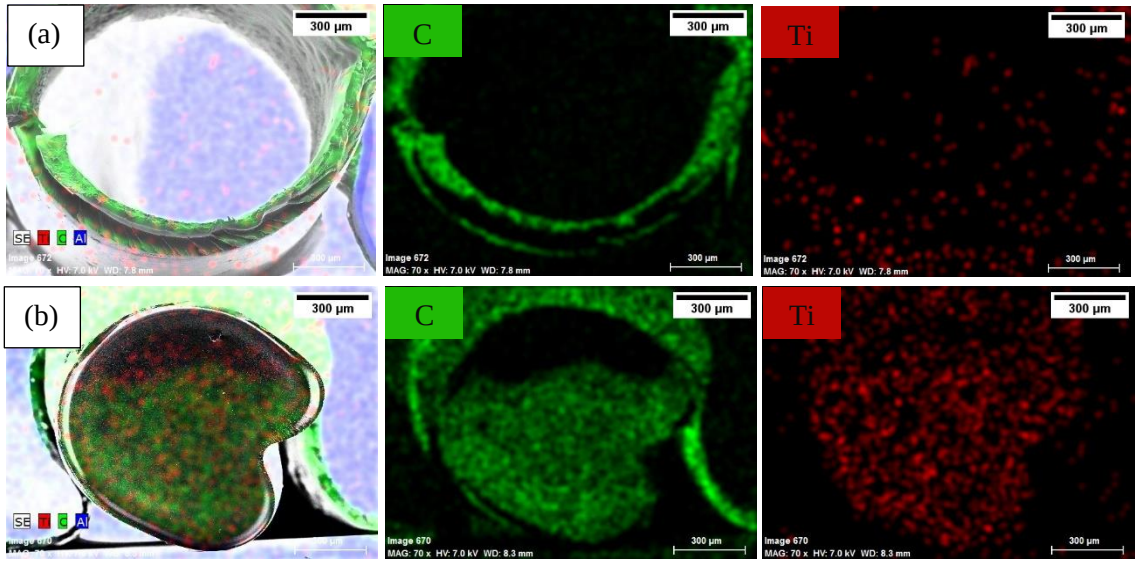

Fig. 6.10 EDS elemental mapping of PVB-amTiO$_2$F cross-sections prepared with (a) 10 wt.% TTIP bath concentrations, and (b) 50 wt.% TTIP bath concentrations.

findings were also investigated by point analyses (**Fig. 6.11**), where more detailed and precise elemental data is obtained. These results indicated that the reaction proceeded from the fiber's outer surface. The 10 wt.% TTIP concentration may have been small to react with PVB, resulting in small diffusion which only led to local Ti distribution mostly at the fiber's outer surface. But, for 50 wt.%, a uniform distribution of Ti is observed within the fiber, which indicates easy diffusion of interacted Ti to the reactive sites.

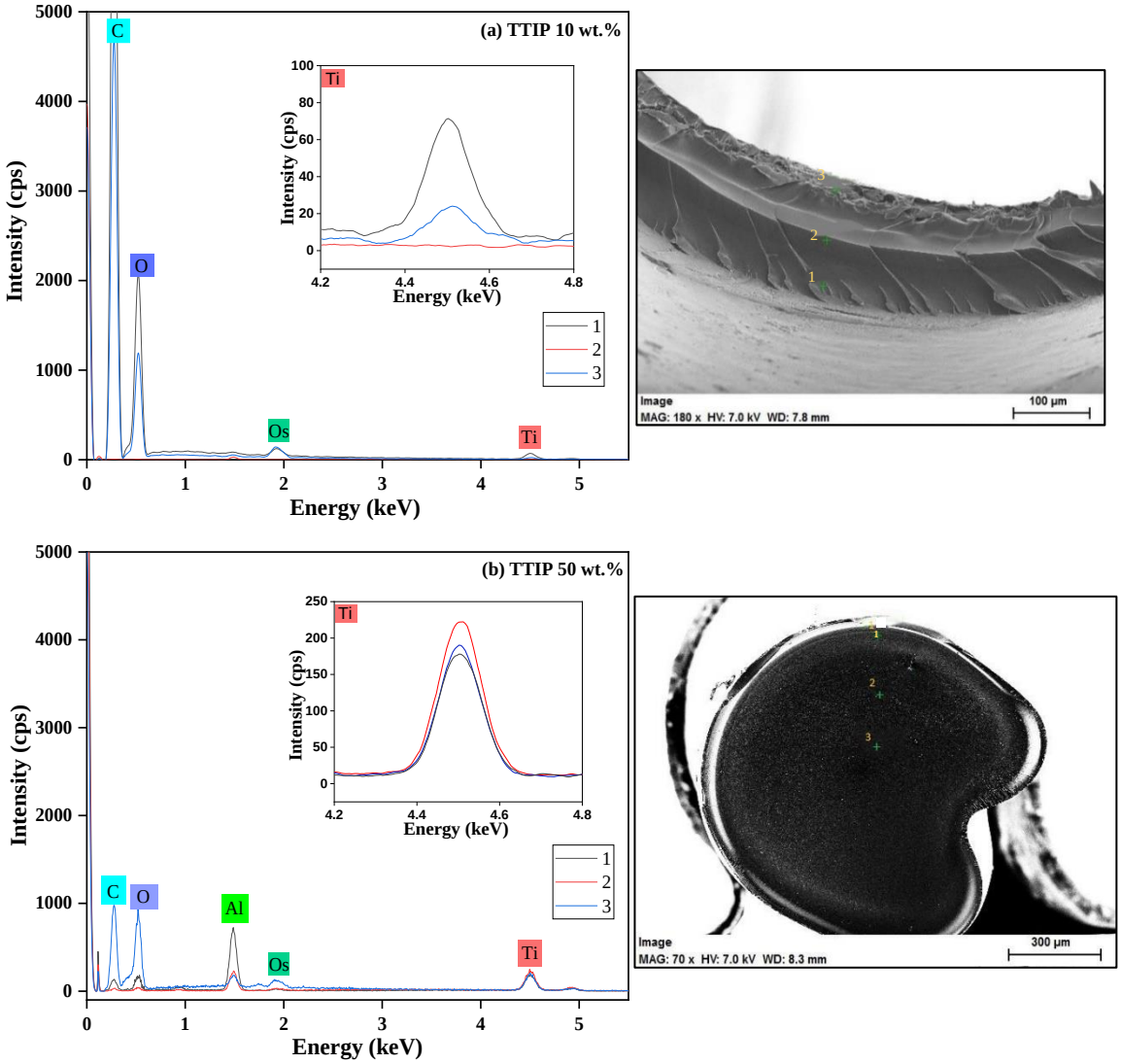

Fig. 6.11 Point analysis of EDS for the PVB-amTiO$_2$F samples. 3 analysis points were indicated by green cross in the right-side pictures; point 1 indicates the surface, point 2 indicates the intermediates of the other two and point 3 indicates the center position of the fiber cross-section. Al might appear from the sample holder. The magnified plot (inset) illustrates Ti distribution at three points for both fibers.

6. 3.6 XPS measurements

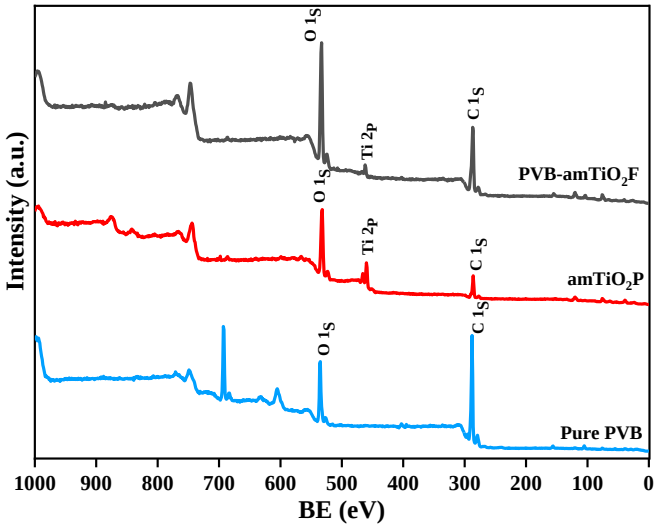

Fig. 6.12 Wide-scan XP spectra of pure PVB, amTiO$_2$P, and PVB-amTiO$_2$F.

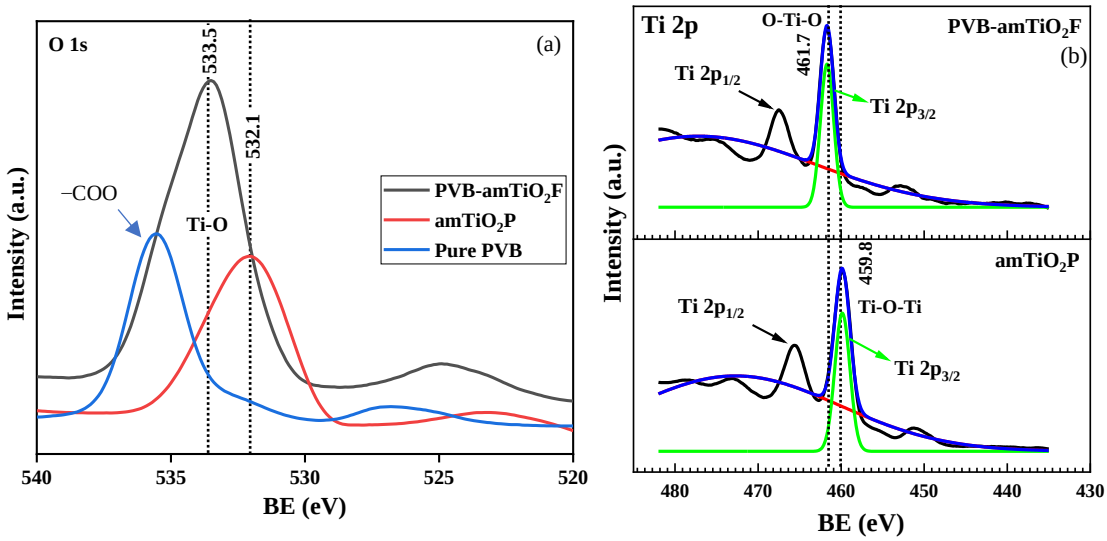

Fig. 6.13 XP spectra of pure PVB, amTiO$_2$P, and PVB-amTiO$_2$F; (a) O 1s orbital, and (b) Ti 2p orbital.

The electron structure on the surface of PVB-amTiO$_2$F is analyzed using XPS to obtain chemical information about C, O, and Ti atoms while bare amTiO$_2$P and pure PVB samples were used as controls (**Fig. 6.12**). PVB-amTiO$_2$F and amTiO$_2$P showed obvious peaks of C 1s, O 1s, and Ti 2p, while the XPS pattern of Ti 2p was absent only for pure PVB. The spectral analysis O 1s results of the PVB-amTiO$_2$F, amTiO$_2$P, and pure PVB samples are enlarged in **Fig. 6.13** (a). The O 1s

peak of amTiO$_2$P at 532.1 eV can be ascribed to the Ti–O bond [27]. However, there was a positive shift in the Ti–O bond binding energy for PVB-amTiO$_2$F, which was most likely due to the coordination of titanium to –OH and acetyl CO groups on a pyranose ring. For amTiO$_2$P, the spin-orbit splitting (5.7 eV) of Ti 2P led to the appearance of two 2p peaks at around 459.8 and 465.5 eV, corresponding to Ti 2p$_{3/2}$ and Ti 2p$_{1/2}$ respectively (**Fig. 6.13** (b)). According to the splitting, it is suggested that Ti was mostly Ti^{4+}. Since the oxygen element was more electronegative than the titanium, the two Ti 2p peaks of PVB-amTiO$_2$F were 1.9 eV higher than those of amTiO$_2$P, reaching 461.7 eV and 467.5 eV respectively [28]. The positive Ti 2p$_{3/2}$ shifts resulting from the replacement of certain Ti–O–Ti bond [29] with O–Ti–O bond for PVB-amTiO$_2$F can be attributed to the low-intensity fitted peaks. Besides, there is a shoulder near the Ti 2p$_{3/2}$ peak that existed, which can be considered the Ti^{3+} state [30].

6.3.7 Porous structure analysis

Fig. 6.14 shows the N$_2$ adsorption isotherms and the corresponding BJH total pore volume plots of PVB-amTiO$_2$F with different TTIP bath concentrations. At relatively high pressure, the curve exhibits convexity to the *P/P$_0$* axis in **Fig. 6.14** (a), which is attributed to a type III isotherm where adsorbent and adsorbate had low interactions [31]. The BJH adsorption pore size distribution of the fibers was narrow, with a mean value of 6.8 nm, suggesting that the materials have a typical mesoporous layer in the internal surface. No significant changes in pore size distribution were observed when TTIP bath concentration was changed, as shown in **Fig. 6.14** (b). However, lower the pore volume of the 50 wt.% TTIP concentration sample confirmed a relatively dense external fiber surface which may be due to less PVB swelling during fiber preparation. For 10 wt.% to 50 wt.% samples, the BET surface area is represented in **Table 6.1**. These differences are ascribed to the collapse of some mesopores at the non-hollow structure and the agglomeration of the

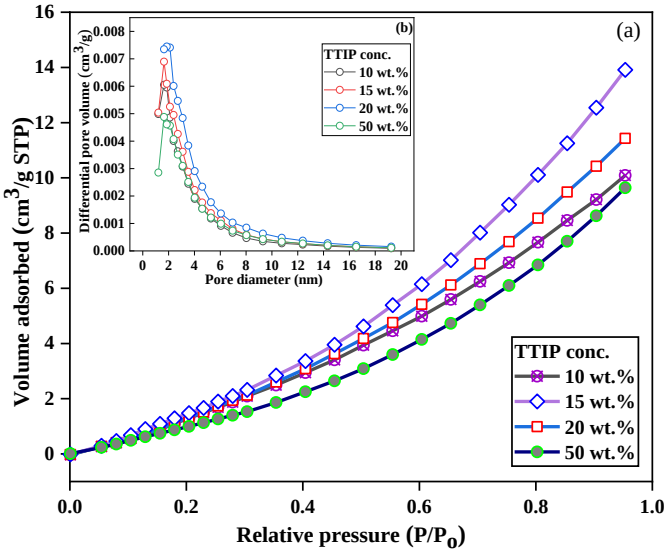

Fig. 6.14 (a) N$_2$ adsorption isotherms (-196 °C), and (b) the corresponding BJH pore size distribution plots of PVB-amTiO$_2$F with different TTIP bath concentrations.

Table 6.1 Effect of TTIP bath concentration on the specific surface area of PVB-amTiO$_2$F fibers.

TTIP wt.%	BET surface area (m^2g^{-1})
10	15.30
15	14.12
20	16.75
25	12.40

amTiO2 particles on the external surface. Also, the bonded Ti species on the mesostructured network is increased due to the diffusion of amTiO2, which subsequently preserves the relatively low surface area with an integrated non-hollow structure.

6.3.8 Effects of pH on MB adsorption

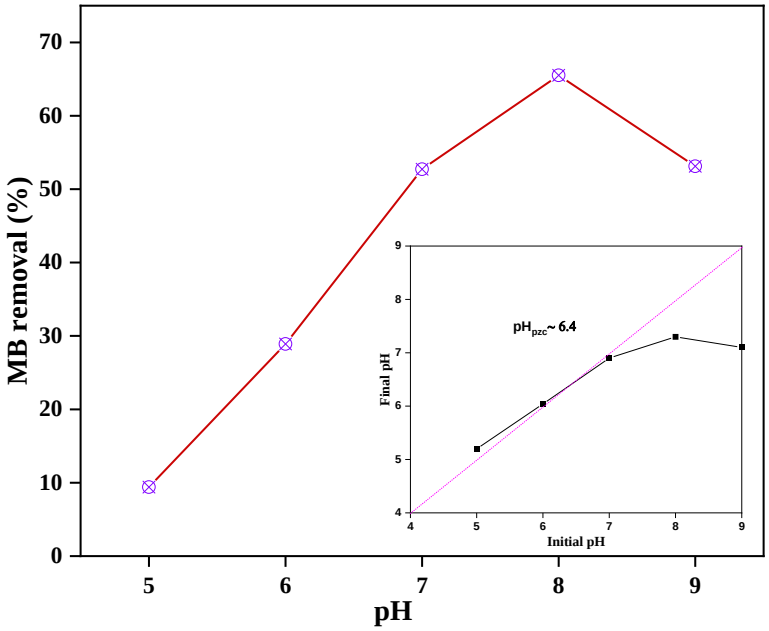

Fig. 6.15 Effect of the solution pH on equilibrium MB dye adsorption performance exhibited by 20 wt.% PVB-amTiO2F.

This series of tests was carried out using 0.2 g of 20 wt.% PVB-amTiO2F, 10 mL (10 mg/L) of dye, and equilibrium adsorption time in the dark. Solution pH is an important factor that affects the magnitude of the adsorbent surface charge and the dye molecule's ionization state. **Fig. 6.15** shows the adsorption of MB increased from 10 to 65% when the pH was increased from 5 to 8 and then a decrease started due to desorption. In an aqueous medium, MB shows a pKa of 5.8 indicating that it can exist in the molecular form when the pH < pKa and ionized form when the pH > pKa [32]; meaning that higher than pH 5.8 could be suitable for MB adsorption by electrostatic attraction. In this work, the pH_{pzc} of the as-prepared PVB-amTiO2F was 6.4 (inset **Fig. 6.15**), measured by the pH drift method [33,34], which is considered comparable with CA-TiO_2 composite gel fiber prepared by Kurokawa [20]. At $pH<pH_{pzc}$, a repulsive electrostatic force was generated due to the increased number of positively charged sites on the fiber surface which did not favor the adsorption of dye cations. Conversely, the higher uptake values were obtained at $pH>pH_{pzc}$ because of electrostatic attractions between the positively charged dye cationic and the negatively charged fiber TiO_2 according to equation (6.6) [20,35–37]. Electrostatic attractions probably become predominant in MB adsorption at higher pH when PVB-amTiO2F was deprotonated. Considering the above points, a pH of 8 was chosen as the experimental pH for the removal of dye in the subsequent experiments.

$$H_2O + TiOH_2^+ \xleftarrow[pH<pH_{pzc}]{H_3O^+} TiOH \xrightarrow[pH>pH_{pzc}]{OH^-} TiO^- + H_2O \text{ ---------- (6.6)}$$

6.3.9 MB adsorption performance

We conducted adsorption studies in the dark to clarify the adsorption ability of PVB-amTiO2F before analyzing its photoreduction performance. **Fig. 6.16** shows the change in the MB concentration as a function of time when the PVB-amTiO2F samples were kept in the test solutions. In this diagram, *A* denotes the absorbance at each given time whereas A_0 indicates the test solution's initial absorbance. It can be seen that the adsorption capacity of different PVB-amTiO2F was related to their porous structure and relative Ti content. As depicted in **Fig. 6.16**, the removal % increased with increasing residual Ti content and the relevant porous property of the PVB-amTiO2F, adsorbing a maximum of about 70% MB when reaching equilibrium. Meanwhile, the adsorption of dye molecules by 15 wt.% PVB-amTiO2F seemed to be rather perplexing, showing down to about 48% uptake for a similar timespan. This might be attributed to the fiber's changing surface area and the variations in its mesoporous outer wall where diffusion starts from one site to another. A similar result was also reported by Asai *et al*. [13].

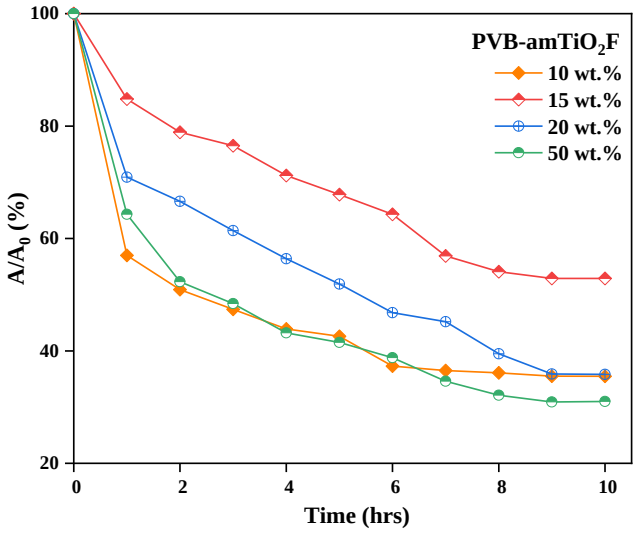

Fig. 6.16 The adsorption dynamics of MB in different reaction systems, when the samples were immersed into the MB solutions in the dark. Reaction conditions: Fiber: 0.2 g, 10 mL (10 mg/L) MB, pH~8.0, at 18 °C.

6.3.10 Adsorption kinetics

The adsorption kinetic results of MB on PVB-amTiO2F were evaluated using Lagergren pseudo-first-order and pseudo-second-order models, as depicted in **Fig. 6.17**(a) and (b), and **Table 6.2**. The best fit of the linear equations suggested that the pseudo-second-order kinetics model gave the $Q_{e,cal}$ values close to the experimental Q_e values. Furthermore, the regression coefficient (R^2)

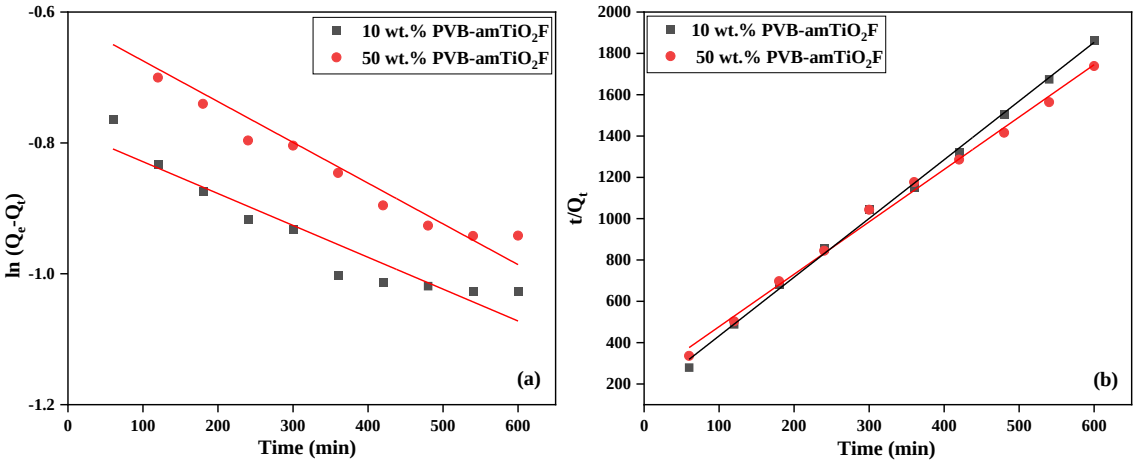

Fig. 6.17 The adsorption kinetics plots of MB on PVB-amTiO$_2$F fitted with (a) pseudo-first-order, and (b) pseudo-second-order model.

for the pseudo-second-order kinetics model was 0.997 and 0.994 for MB absorption on 10 wt.% and 50 wt.% PVB-amTiO$_2$F, respectively, better than the Lagergren pseudo-first-order kinetic model. This result indicated that the pseudo-second-order model of MB's adsorption kinetics on PVB–amTiO$_2$F provides more in-depth information, so the kinetics could be categorized as chemisorption [38], because of electrostatic interactions between the fiber and the dye functional groups [12]. Similar MB adsorption kinetics on the other adsorbents have also been commonly studied [39]. But, in our study, higher adsorbent dose and longer adsorption equilibrium time have a great influence on the kinetics and hinder the adsorption capacity. The efficient adsorptive removal of MB using the PVB-amTiO$_2$F was compared with other amorphous titania adsorbents in **Table 6.3**. It was clear from the data that most of the amorphous titania particles had shown good adsorption efficiency for other dyes like CV, MG, and CR. In addition, TiO$_2$ sulfonated carbon composite had a very good removal performance upon MB dyes. However, compared to CA-amTiO$_2$F, PVB-amTiO$_2$F have a high adsorption capacity for MB dyes. This high adsorption capacity could be a result of higher surface area and greater adsorption sites in PVB-amTiO$_2$F.

Table 6.2 The adsorption kinetics parameters of MB on PVB-amTiO$_2$F were calculated from the best fitting of pseudo-first-order and pseudo-second-order models.

Kinetics model	**Parameters**	**10 wt.% PVB-amTiO$_2$F** $Q_{e,exp}$ (mg g^{-1}) = 0.34	**50 wt.% PVB-amTiO$_2$F** $Q_{e,exp}$ (mg g^{-1}) = 0.367
Pseudo-first-order			
	$Q_{e,cal}$ (mg g^{-1})	0.458	0.542
	K_1 (min^{-1})	-8.11x 10^{-7}	-1.03x 10^{-6}
	R^2	0.887	0.922
Pseudo-second-order			
	$Q_{e,cal}$ (mg g^{-1})	0.351	0.394
	K_2 (min^{-1})	0.054	0.028
	R^2	0.997	0.994

6.3.11 Decomposition abilities for MB

We continued to examine the reduction ability of MB under visible light after the adsorption experiments described above. The absorbance was normalized by the absorbance after 10-11 hrs dark adsorption, denoted by A_1, given in the equation below,

$$A/A_1 = \exp(-Kt) \text{ ---------- (6.7)}$$

where K represents the rate constant, and t is the total time employed for the test.

Table 6.3 Comparison on equilibrium adsorption % of dye onto different amorphous titania adsorbents.

Adsorbent	Adsorbent type	Dye	Adsorption (%)	References
Amorphous TiO_2	Particle	CV	87-98	([11])
Curcumin-sensitized	Composite	MB	40-60	([6])
Amorphous TiO_2		Orange-II	45	
Amorphous TiO_2	Particle	MG	~80	([12])
		CV	~97	
TiO_2 sulfonated carbon	Composite	MB	~99	([37])
		CR	~98	
CA-amTiO$_2$F	Fiber	MB	~60	([13])
PVB-amTiO$_2$F	Fiber	MB	68-70	This study

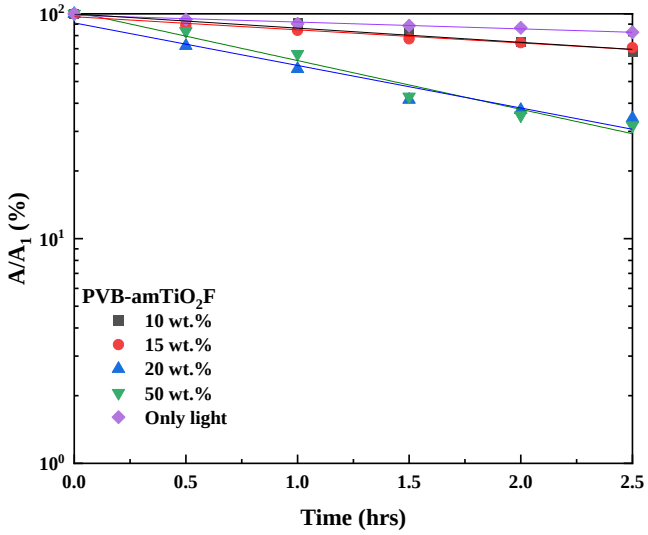

Fig. 6.18 Variation in normalized absorbance for MB concentrations by visible light irradiation, as a function of immersion time. The lines represent the fitting results using equation (6.7).

Fig. 6.18 shows the variation in fitting lines for A/A_1 in MB reduction using equation (6.7). The measured K values from the line fits are illustrated in **Fig. 6.19**. Overall, the lower Ti content PVB-amTiO2F showed very low K_{MB} values which are almost comparable to 'only-light' samples,

suggesting an absence of photodegradation. However, setting 10 wt.% and 15 wt.% aside, the 20 wt.% and 50 wt.% fiber samples showed little and slow photoactivity. This is evidence confirming the low photocatalytic property for amorphous TiO_2 hybrid fibers which is a similar result to that shown by Kanna *et al*. [11] and Asai *et al*. [13].

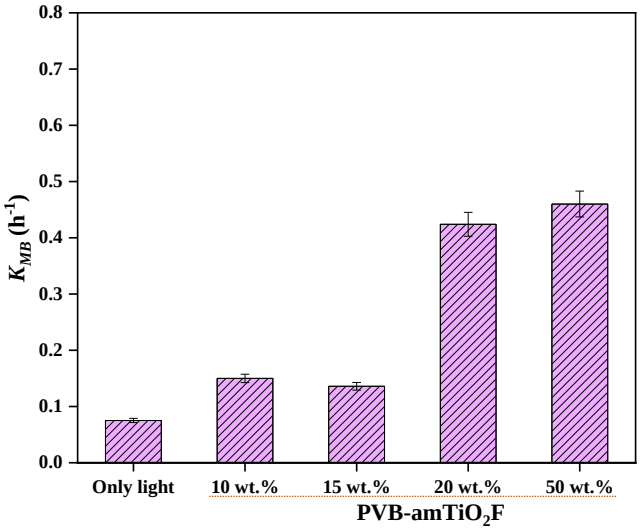

Fig. 6.19 Decomposition rate constant for MB obtained from the fitting in **Fig. 6.18**.

6.3.12 Removal abilities against other dyes

For the comparison with MB dye, we also investigated the adsorption and decomposition ability of PVB-amTiO2F on other dyes such as acidic MO and zwitterionic Rh-B. According to **Fig. 6.20**

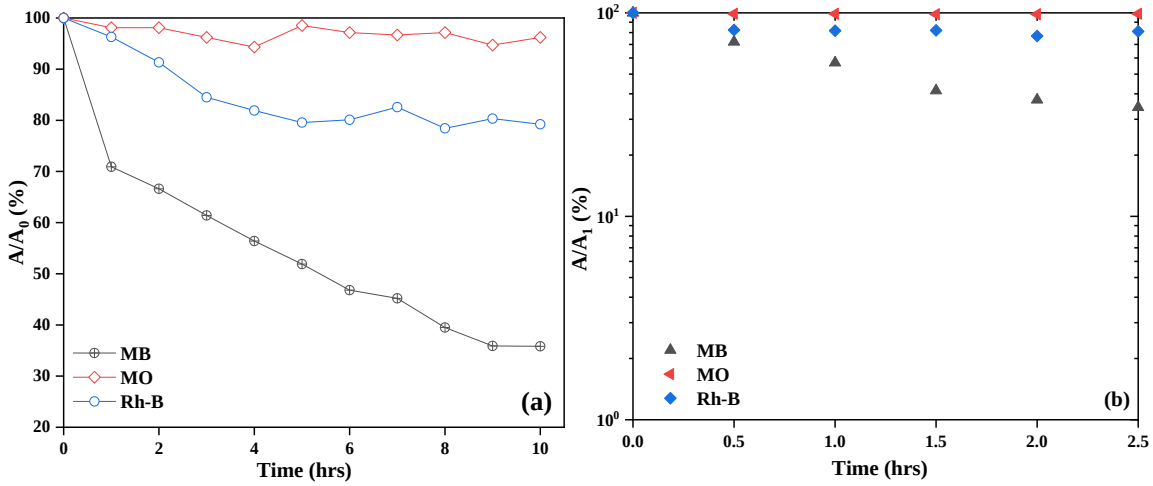

Fig. 6.20 (a) The capacity of adsorbed MB, MO, and Rh-B dyes in the dark, and (b) dye decomposition ability in visible light irradiation for 20 wt.% PVB-amTiO2F, Reaction conditions: Fiber 0.2 g, 10 mL (10 mg/L) dyes, pH~8.0, at 18 °C.

(a), the adsorption capacities for MB, Rh-B, and MO were ~68%, ~20%, and ~4% respectively, consistent with the experimental capacity order of MB>Rh-B>MO. Considering the molecular

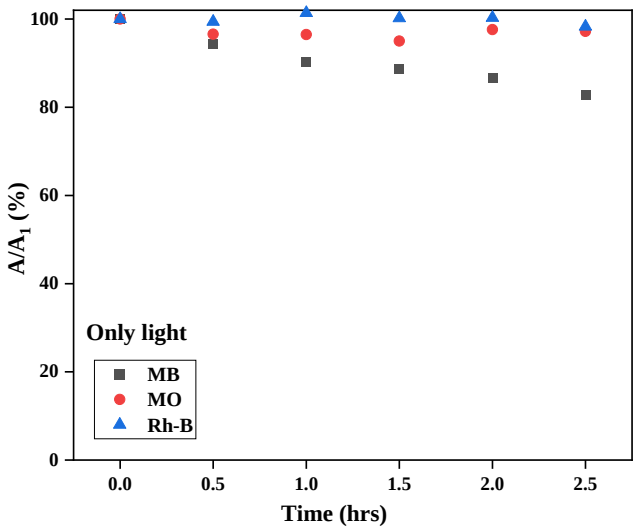

Fig. 6.21 Variation of dye absorbance in visible light, where no PVB-amTiO$_2$F was added.

sizes of the dyes (MB<MO<Rh-B:213.38<255.72<365.66 cm^3/mole), it is reasonable that adsorption of bulky (dimer) Rh-B required a long time and resulted in a lower adsorption amount compared to MB, even though Rh-B can show zwitterionic behavior at higher pH. Meanwhile, the low adsorption value for MO was attributed to the more electrostatic repulsion between the negatively charged adsorbent (PVB-amTiO$_2$F) and the anionic MO dye molecule [40,41]. **Fig. 6.20** (b) shows the decomposition abilities of 20 wt.% PVB-amTiO$_2$F for the above-mentioned dyes under visible light. MB could be decomposed by PVB-amTiO$_2$F but MO was almost unchanged. To ascertain the true nature of PVB-amTiO$_2$F, we could conclude that adsorption becomes a dominant factor here [11]. For reference, in the dye solutions without any fiber samples, MO and Rh-B were not removed but MB is partially affected (**Fig. 6.21**). Therefore, we can conclude that the removal of MB under light can only be a little enhanced by PVB-amTiO$_2$F.

6.3.13 Possible mechanism of MB dye adsorption and photodegradation

From the adsorption and decoloration behavior of PVB-amTiO$_2$F, we concluded that these reactions were independent but influenced by some other factors. In our results, cationic MB was adsorbed by PVB-amTiO$_2$F. The removal mechanism of MB dye onto PVB-amTiO$_2$F involves the electrostatic attraction between the dye and adsorbent ionic charges which are postulated with pH results [4,11,12,20,39]. **Fig. 6.22** shows the affected peak positions and intensity of PVB-amTiO$_2$F after MB adsorption. The peak intensity around the Ti—O—C band at 1132 cm^{-1} and around the Ti—O band at 600 cm^{-1} is decreased due to the interactions of MB. Furthermore, the presence of nitrogen atoms in the MB dye structure could form hydrogen bonds with –OH groups of PVB-

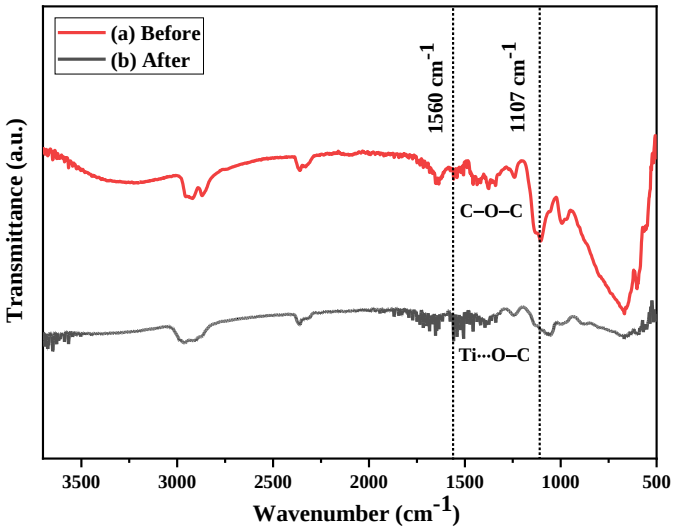

Fig 6.22 ATR-FTIR spectra of PVB-amTiO$_2$F (a) before, and (b) after MB removal.

amTiO$_2$F [4,38]. But we could not find such evidence from the FTIR spectra in our study. Since the fragment of MB bears a positive charge, it should be favorably adsorbed to the negative sites of the PVB-amTiO$_2$F surface and subsequently could be attacked by the very active •OH fraction under visible light, according to the same process described by Kanna *et al*. [11]. Overall, the mode of MB removal by PVB-amTiO2F was mostly by adsorption (~68%), but with combined prolonged adsorption and photocatalytic activity, it could be enhanced up to ~85% or more.

6.3.14 Reusability

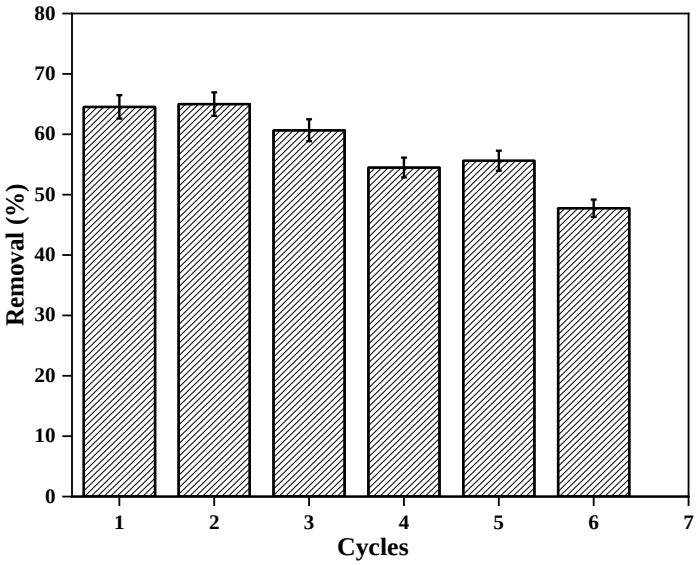

Fig. 6.23 Reusability of PVB-amTiO$_2$F after adsorption by MB dye.

An extended study was accomplished for six adsorption/desorption cycles to assess the reusability of the developed PVB-amTiO$_2$F. Desorption of MB dye was executed by soaking the dye-adsorbed PVB-amTiO$_2$F in 20 mL ethanol solution, under gentle stirring for 8-10 hrs. After regeneration, the PVB-amTiO$_2$F was reused in the next adsorption run. **Fig. 6.23** shows the repeatability study of PVB-amTiO$_2$F. After 6 cycles, the removal efficiency was 47-48%, which could indicate the reusability and durability of the fabricated PVB-amTiO$_2$F for MB adsorption.

6.4 CONCLUSION

In this study, we investigated the phenomenon whereby poly(vinyl butyral) fibers, cross-linked by amorphous TiO$_2$ (i.e. PVB-amTiO$_2$F), removed MB dyes upon visible light irradiation. According to this study, the principle of removing dye from the aqueous solution was mainly by chemisorption (~ 68%). The adsorption and degradation dynamics were mostly controlled by the fiber's relative Ti content, surface area, and the charge characteristics of the dyes. The ability of PVB-amTiO$_2$F to remove dye from different dye solutions revealed that they could be most efficient for cationic dyes, but not for acidic dyes. In addition, a repeatability test of PVB-amTiO$_2$F showed an average to good reuse possibility for several times with little decrease in the removal percentage.

REFERENCES

1 A. S. Eltaweil, I. M. Mamdouh, E. M. Abd El-Monaem and G. M. El-Subruiti, *ACS Omega*, 2021, **6**, 23528–23541.

2 M. Oz, D. E. Lorke, M. Hasan and G. A. Petroianu, *Medicinal Research Reviews*, 2011, **31**, 93–117.

3 C. D. Carneiro, J. C. Amorim, S. M. Cadena, G. R. Noleto, P. Di Mascio, M. E. Rocha and G. R. Martinez, *Food and Chemical Toxicology*, 2010, **48**, 2380–2387.

4 A. S. Eltaweil, E. M. Abd El-Monaem, G. M. El-Subruiti, M. M. Abd El-Latif and A. M. Omer, *RSC Advances*, 2020, **10**, 19008–19019.

5 V. L. E. Siong, X. H. Tai, K. M. Lee, J. C. Juan and C. W. Lai, *RSC Advances*, 2020, **10**, 37905–37915.

6 S. Buddee and S. Wongnawa, *Journal of Sol-Gel Science and Technology*, 2015, **75**, 152–163.

7 S. Sun, P. Song, J. Cui and S. Liang, *Catalysis Science & Technology*, 2019, **9**, 4198–4215.

8 M. K. I. Senevirathna, P. Pitigala and K. Tennakone, *Journal of Photochemistry and Photobiology A: Chemistry*, 2005, **171**, 257–259.

9 B. Ohtani, Y. Ogawa and S. Nishimoto, *Journal of Physical Chemistry B*, 1997, **101**, 3746–3752.

10 Q. Wang, X. Chen, K. Yu, Y. Zhang and Y. Cong, *Journal of Hazardous Materials*, 2013, **246**, 135–144.

11 M. Kanna, S. Wongnawa, S. Buddee, K. Dilokkhunakul and P. Pinpithak, *Journal of Sol-Gel Science and Technology*, 2010, **53**, 162–170.

12 P. Sriprang, S. Wongnawa and O. Sirichote, *Journal of Sol-Gel Science and Technology*, 2014, **71**, 86–95.

13 H. Asai, S. Kato, and K. Nakane, *Solid State Sciences*, 2019, **88**, 67–73.

14 A. H. Bhuiyan, T. Nagakawa and K. Nakane, *Journal of Applied Polymer Science*, 2021, **138**, 50164.
15 H. Kyung, J. Lee, and W. Choi, *Environmental Science & Technology*, 2005, **39**, 2376–2382.
16 T. P. Ang, J. Y. Law and Y.-F. Han, *Catalysis Letters*, 2010, **139**, 77–84.
17 K. S. Srikanth, H. S. Kushwaha and R. Vaish, *Materials Science in Semiconductor Processing*, 2018, **73**, 51–57.
18 J.-P. Simonin, *Chemical Engineering Journal*, 2016, **300**, 254–263.
19 D. Robati, *Journal of Nanostructure in Chemistry*, 2013, **3**, 1–6.
20 Y. Kurokawa, *Polymer Gels and Networks*, 1996, **4**, 153–163.
21 A. A. Hanna, A. H. Basta, H. El-Saied and I. F. Abadir, *Polymer Degradation and Stability*, 1999, **63**, 293–296.
22 E. Corroyer, M.-C. Brochier-Salon, D. Chaussy, S. Wery and M. N. Belgacem, *International Journal of Polymer Analysis and Characterization*, 2013, **18**, 346–357.
23 P. Peer, M. Polaskova and P. Suly, *Chinese Journal of Polymer Science*, 2018, **36**, 742–748.
24 P. Kongsong, L. Sikong, S. Niyomwas, and V. Rachpech, *The Scientific World Journal*, 2014, **2014**, ID 869706.
25 Z. Lei, Z. Chen, Y. Zhou, Y. Liu, J. Xu, D. Wang, Y. Shen, W. Feng, Z. Zhang and H. Chen, *Composites Science and Technology*, 2019, **180**, 44–50.
26 K. Alamelu, V. Raja, L. Shiamala and B. J. Ali, *Applied Surface Science*, 2018, **430**, 145–154.
27 T. N. Nguyen, V. V. Tran, V. K. H. Bui, M. Kim, D. Park, J. Hur, I. T. Kim, H. U. Lee, S. Ko and Y.-C. Lee, *Journal of Nanoscience and Nanotechnology*, 2020, **20**, 6844–6849.
28 L. Ji, S. Zhou, X. Liu, M. Gong and T. Xu, *Journal of Materials Science*, 2020, **55**, 2471–2481.
29 M. Xing, F. Shen, B. Qiu and J. Zhang, *Scientific Reports*, 2014, **4**, 1–7.
30 M. S. P. Francisco, V. R. Mastelaro, P. A. Nascente and A. O. Florentino, *The Journal of Physical Chemistry B*, 2001, **105**, 10515–10522.
31 K. S. Sing, D. H. Everett, R. A. W. Haul, L. Moscou, R. A. Pierotti, J. Rouquerol and T. Siemieniewska, *Pure Applied Chemistry*, 1985, **57(4)**, 603–619.
32 R. M. Firdaus, N. I. M. Rosli, J. Ghanbaja, B. Vigolo and A. R. Mohamed, *Journal of Nanoparticle Research*, 2019, **21**, 257.
33 Y. Bessekhouad, D. Robert, J.-V. Weber and N. Chaoui, *Journal of Photochemistry and Photobiology A: Chemistry*, 2004, **167**, 49–57.
34 B. K. Nandi, A. Goswami, and M. K. Purkait, *Applied Clay Science*, 2009, **42**, 583–590.
35 F. Çiçek, D. Özer, A. Özer and A. Özer, *Journal of Hazardous Materials*, 2007, **146**, 408–416.
36 X. Wang, N. Zhu, and B. Yin, *Journal of Hazardous Materials*, 2008, **153**, 22–27.
37 A. Aguedach, S. Brosillon and J. Morvan, *Applied Catalysis B: Environmental*, 2005, **57**, 55–62.
38 N. I. I. Zamri, S. L. N. Zulmajdi, N. Z. A. Daud, A. H. Mahadi, E. Kusrini and A. Usman, *SN Applied Sciences*, 2021, **3**, 1–16.
39 I. I. Widiyowati, M. Nurhadi, M. Hatami and L. S. Yuan, *Bulletin of Chemical Reaction Engineering & Catalysis*, 2020, **15**, 476–489.
40 N. Mohammadi, H. Khani, V. K. Gupta, E. Amereh and S. Agarwal, *Journal of Colloid and Interface Science*, 2011, **362**, 457–462.
41 K. M. Dalia, A. Mohamad, A. Wan, I. Azni and Z. A. Zurina, *Chemical Engineering Journal*, 2012, 449–457.

This article was published in the *RSC Advances*, 2022; 12, 5300-5311.

CHAPTER SEVEN

7. CONCLUSION AND RECOMMENDATIONS

This thesis has described the design and fabrication of organic-inorganic hybrid fibers namely, PVB-Zr alkoxide and PVB-Ti alkoxide hybrid fibers by adopting air gap (dry-jet wet) spinning. These developed hybrid fibers can effectively be utilized as an enzyme immobilization support matrix, and also organic dye removal.

7.1 RESEARCH SUMMARY

Chapter four has demonstrated the development of PVB-zirconia hybrid hollow fiber via a simple air gap (dry-jet wet) spinning. The results indicate that the developed hybrid fiber exhibited a typical asymmetrical structure containing a thick layer outside while the inside was hollow. The diameter of fiber increased at a particular point with increased PVB content. However, along the fiber axis, the maximum variation of fiber diameter was produced when more PVB was added. With the increment of PVB butyral degree, the surface robustness improved while a fragile structure was formed for reduced butyral content. Data illustrates that Zr alkoxide vastly affected the fiber's external surface since most of the coordination bonding between PVB and Zr happened on that site. It is expected that a large surface area of this hybrid fiber has the potential to be efficient as an enzyme carrier and subsequently the enzyme-immobilized hybrid fiber could be useful in different applications.

Chapter five has reported on the application of PVB-Zr alkoxide hybrid hollow fiber in the field of lactose hydrolysis and ester synthesis. PVB-ZrO_2 hybrid fiber has been proven as an important support matrix for entrap-immobilizing β-galactosidase (IβG) and lipase (IL) enzymes due to its low-cost, large surface area, and stability in electrolyte solutions, phosphate buffer, and organic solvents. Conversion of lactose to glucose and galactose performed by IβG continued much of their activity in wider ranges of pH and temperature than that of free β-galactosidase. Moreover, immobilized lipase (IL) appeared to be an effective catalyst for terpene ester synthesis in organic solvents. IL showed constancy over repeated runs, water content change, and reaction temperature for different organic solvents. Overall, the activity of the immobilized enzyme was shown higher for the increased specific surface area of the hybrid fiber which indicates that hydrolysis and catalysis both happened by the hollow structure. Hence this prepared hybrid fiber could be a good choice for enzyme immobilization matrix compared to other organic-inorganic hybrid materials.

Chapter six is discussed the possibility of removing organic dyes from wastewater by the adsorption and photocatalysis process using PVB-amTiO_2F hybrid fiber. According to this study, the principle of removing dye from the aqueous solution was mainly by chemisorption. The adsorption and degradation dynamics were mostly controlled by the fiber's relative Ti content, surface area, and the charge characteristics of the dyes. The ability of PVB-amTiO_2F to remove dye from different dye solutions revealed that they could be most efficient for cationic dyes, but not for other dyes. Also, good reuse possibilities may prove it as a potential candidate for application in the same field.

7.2 RECOMMENDATION AND SCOPE OF FURTHER STUDY

This study adopted the air gap (dry-jet wet) spinning method to develop polyvinyl butyral (PVB)-zirconium (Zr) alkoxide hybrid hollow fibers. The resultant PVB-ZrO_2 fibers are hollow inside where the skin of the fiber is incorporated by the coordination bonding between PVB and alkoxide. However, the cross-section of the fiber does not any evidence of macrovoids or finger-like voids developed from beneath the outer skin layer to the inner layer for the PVB fibers. PVB-dominant hybrid fibers are generally popular as hollow fiber membranes. To produce such type of performance, we recommend the addition of other polymers in the spinning solution which can facilitate the macropore into the fiber surface.

As enzyme-immobilization support for β-galactosidase, PVB-ZrO_2 hybrid fiber shows stability to citrate buffer, phosphate buffer solution, electrolyte solution, and other organic solvents. However, in a continuous bioreactor, there was a possibility of enzyme leakage from the fiber matrix; resulting in very high enzyme activity for the first few days and then an immediate drop-down. This could be due to the presence of enzymes in the vicinity of the fiber surface rather than trapped inside the matrix. Hence, we suggest the proper washing of prepared fibers with solvents in the preparatory stage so that enzymes attached to the surface could be removed easily.

Furthermore, this study found a few difficulties in the preparation process of PVB-amTiO_2 hybrid fiber. Unlike Zr alkoxide, the reaction between PVB and Ti alkoxide is slow which affects the phase change when the spinning solution of PVB pass-through into the alkoxide coagulation solution. This could lead to the flexible and limp PVB-amTiO_2 hybrid hollow fiber where the unreacted part of PVB and alkoxide was difficult to remove. In addition, the dye adsorption rate by PVB-TiO_2 is hindered by the deficient total pore volume of fiber. Hence, we recommend the addition of a foaming agent which could improve the total pore volume of the fiber.

For the continuation of the current research work, the following recommendations can be taken into consideration for future works:

I. Addition of other polymers like PVP/PEG and changing of solvent like DMAc can be mixed with the PVB spinning solution to prepare the hybrid fiber with porous structure and skin layer.

II. Like β-galactosidase and lipase, other enzymes like urease, laccase, and peroxidase can be immobilized into the PVB-Zr alkoxide hybrid fiber for different applications.

III. Other than only cationic dye, heavy metals like chromium can be removed by PVB-amTiO_2 hybrid fiber.

LIST OF PUBLICATIONS

Published Papers

1. **Anamul Hoque Bhuiyan**, Takuma Nagakawa, and Koji Nakane, "Polyvinyl butyral-zirconia hybrid hollow fibers prepared by air gap spinning", *Journal of Applied Polymer Science*, **Vol. 138**, Issue 14, Oct. 2020, **https://doi.org/10.1002/app.e50164**, https://onlinelibrary.wiley.com/doi/epdf/10.1002/app.50164.

2. **Anamul Hoque Bhuiyan**, Takuma Nagakawa, Mohammad Zakaria and Koji Nakane, "Utilization of polyvinyl butyral-zirconium alkoxide hybrid hollow tube as an enzyme immobilization carrier", *Journals of Materials Science*, **Vol. 56**, Pages 8668–8678, Feb. 2021, **https://doi.org/10.1007/s10853-021-05829-x**, https://link.springer.com/article/10.1007/s10853-021-05829-x.

3. **Anamul Hoque Bhuiyan**, Mohammad Zakaria, and Koji Nakane, "Structural analysis and dye removal behavior of amorphous titania embedded poly(vinyl butyral) hybrid fiber" *RSC Advances,* **Vol. 12**, 5300-5311, Feb. 2022, **https://doi.org/10.1039/D1RA07247A**, https://pubs.rsc.org/en/content/articlelanding/2022/ra/d1ra07247a

Presentation at International Conferences

1. **Anamul Hoque Bhuiyan**, Takuma Nagakawa, and Koji Nakane, "Preparation of polyvinyl butyral-zirconia hybrid hollow fibers by air gap spinning and its use in enzyme immobilization*" 2020 XUT Annual Graduate Conference and International Academic Symposium, Nov. 2020,* Xi'an, China. [ORAL]

2. **Anamul Hoque Bhuiyan** and Koji Nakane, "Structural investigation and dye removal performance of amorphous titania embedded poly(vinyl butyral) hybrid fiber", *The 16th XUT Annual Graduate Conference and International Academic Symposium, Nov. 2021*, Xi'an, China. [ORAL]

3. **Anamul Hoque Bhuiyan** and Koji Nakane, "Structure and properties of polyvinyl butyral-metal alkoxides hybrid hollow fibers prepared by air gap spinning", *49th Textile Research Symposium, Kyoto; The Textile Machinery Society Japan,* Oct. 8-10, 2022. [ORAL]

ACKNOWLEDGEMENTS

In the name of **ALLAH**, the most gracious, the most merciful, the originator, the one and only creator of each and everything. The deepest gratitude and sincere thanks to almighty **ALLAH**, whose peace and kindness always surround us and give us the strength to go forward.

First, a heartfelt appreciation to my supervisor, **Professor Koji Nakane**, Frontier Fiber Technology and Science, **University of FUKUI**, for his constant support and guidance from the beginning of the research proposal till the completion of this thesis. His dedication and encouragement, constructive criticism, and suggestions keep me on track in the journey of my PhD study. Also, his careful reading of the draft, valuable comments, and technical and helpful suggestions immensely contributed to improving the quality of this research work. This thesis would not be in its current form without his tremendous editorial support to polish my work into a formal dissertation.

My earnest thanks to the **Graduate School of Engineering**, for all the laboratory support provided for this dissertation. I am ever grateful to **Professor Shuichi Tanoue**, **Professor Kenji Hisada**, and **Dr. Kazumasa Hirogaki** for their generous support, advice, and correction in my thesis book. I would like to thank **Dr. Hanako Asai**, **Professor Satoshi Irie,** and **Dr. Fumihiro Nishimura** for their technical assistance in performing the experimental measurement.

My sincere thanks to Mr. Takuma Nagakawa, Dr. Mohammad Zakaria (my co-authors), and Mr. Tsuyoshi Aoike for their constructive support regarding my work over my PhD journey. Special thanks and appreciation belong to my fellow **Materials lab** students for their excellent support and contribution to various experimental investigations of my research work.

I would like to special thanks to Mr. Kanta Shibahara, my tutor, and first Japanese friend for his entire support for all my official work, academic tasks, and social life.

I am deeply grateful to my parents for their absolute love and encouragement throughout my life. They have sacrificed their own need for support and sent me overseas to achieve my PhD degree. I sincerely acknowledge the warm support and encouragement of my family during the research work. It is beyond my capability to pay my gratitude to my wife for her unremitting support in every difficulty, who consoled me and became a source of constant inspiration in my life. I am regretful to my two daughters for being unable to give them enough time. I feel sorry for my children who always had been day-long waited for my return from the laboratory.

Finally, my profound gratitude to the Japanese Government for the scholarship support towards this PhD degree. I am grateful to the government of the People's Republic of Bangladesh who permitted me to higher study and also to Dhaka University of Engineering and Technology (DUET), Bangladesh for providing me with a study leave to pursue the PhD degree.